SANDIA REPORT
SAND2005-6385
Unlimited Release
Printed October 2005

Reconstruction Algorithm Development and Assessment for a Computed Tomography Based-Spectral Imager

Bridget K. Ford, José S. Salazar, and Mark P. Wilson

Prepared by
Sandia National Laboratories
Albuquerque, New Mexico 87185 and Livermore, California 94550

Sandia is a multiprogram laboratory operated by Sandia Corporation,
a Lockheed Martin Company, for the United States Department of Energy's
National Nuclear Security Administration under Contract DE-AC04-94AL85000.

Issued by Sandia National Laboratories, operated for the United States Department of Energy by Sandia Corporation.

Available to DOE and DOE contractors from
U.S. Department of Energy
Office of Scientific and Technical Information
P.O. Box 62
Oak Ridge, TN 37831

Telephone: (865)576-8401
Facsimile: (865)576-5728
E-Mail: reports@adonis.osti.gov
Online ordering: http://www.osti.gov/bridge

Available to the public from
U.S. Department of Commerce
National Technical Information Service
5285 Port Royal Rd
Springfield, VA 22161

Telephone: (800)553-6847
Facsimile: (703)605-6900
E-Mail: orders@ntis.fedworld.gov
Online order: http://www.ntis.gov/help/ordermethods.asp?loc=7-4-0#online

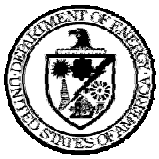

SAND2005-6385
Unlimited Release
Printed October 2005

Reconstruction Algorithm Development and Assessment for a Computed Tomography Based-Spectral Imager

Bridget K. Ford and Mark P. Wilson
Remote Sensing and Exploitation

Jose S. Salazar
Sensor Exploitation Applications

Sandia National Laboratories
P.O. Box 5800
Albuquerque, NM 87185-0570

Abstract

The collection of spatial and temporal information is of primary importance for wide-field transient event detection. Full-field imaging systems coupled with high frame-rate detectors readily enable such collections; however, these configurations are not easily adapted to secondary missions with more stressing spectral requirements. While, spectral filters (e.g., filter wheel) can be introduced, the spectral bandpasses must be fairly broad to accommodate shorter integration times. For staring mode sensors, chromotomographic systems offer significant advantages over more conventional systems (filter wheels, AOTF, LCTF). Most notably, due to their integration of signal at each pixel, hyperspectral data can be collected with higher temporal and spectral resolutions at higher signal to noise ratios. These instruments have proven applicable to such diverse fields as optical testing, biomedical imaging and airborne remote sensing. The goal of this research was to study the applicability of CTS systems to scene and target characterization from space-based platforms.

Contents

List of Figures

List of Tables

1. Introduction

While staring sensors lend themselves toward wide-field monitoring, detection and identification of transient events, they are not easily adapted to hyperspectral imaging. Multiple spectral filters may be used to add moderate spectral information; however, the need for high temporal rates requires that these filters operate with broad spectral bandpasses. For staring sensors one must considered unconventional methods to move from low to high spectral (i.e., multispectral to hyperspectral) resolution. Chromotomographic systems offer significant advantages of more conventional systems (filter wheels, AOTF, LCTF).[1,2] Most notably, due to their integration of signal at each pixel, hyperspectral data can be collected with higher temporal and spectral resolutions and higher signal to noise ratios (SNR).

Chromotomographic spectrometry has a history of approximately 10 years with significant amounts of research focusing on the generation of proof-of-concept devices (in the visible, mid-wave and long-wave infrared). These devices operate under similar principles to medical CT systems. In medical CT scans, x-rays are passed through the body and measured by 2-D detectors. These projections are collected as the x-ray source and detector are moved in opposition about the body. In this way, projections are captured from multiple view angles. This set of projections is then used to reconstruct slices through the body's internal structures. In chromotomographic spectrometry, projections of spectral datacubes (x, y, and λ) are created by imaging through a dispersive element. Rotating the disperser is analogous to moving the x-ray source with respect to the detector. Now instead of reconstructing 3 dimensions of spatial data, we can reconstruct 2 dimensions of spatial and 1 dimension of spectral data (i.e., a spectrum at every ground sample across a 2-dimensional (2-D) scene)

These instruments have proven applicable to such diverse fields as optical testing, biomedical imaging and remote sensing; however, their utility for scene and target characterization from space based platforms has not yet been explored. This was the focus of the LDRD entitled, “Reconstruction Algorithm Development and Assessment for a Computed Tomography Based-spectral Imager”. This report is broken into the following sections: (1) CTS Imaging System and Mathematical Models, (2) Reconstruction Algorithm Development (3) Task-Based Measures of Reconstruction Quality, and (4) Conclusions.

2. Comparison to Standard Spectral Imaging Approaches

Standard spectral imaging approaches require some form of spatial or spectral scanning to measure a complete 3-D (x, y, λ) datacube. Figure 1 for example, shows the scanning requirements of 3 standard spectral imaging systems. For persistent surveillance applications, it is undesirable to leave significant portions of the spatial field or spectral range unmonitored in this way. Chromotomographic spectrometers (CTS), on the other hand, collect spatial and spectral multiplexed datasets. This is done by imaging the scene through a dispersive element such as a rotating prism or fixed computer generated hologram. Although, the spectral and spatial information is now convolved together, this data can be reconstructed using knowledge of the system transfer function. Such multiplexing of spatial and spectral content provides the additional benefit of increased signal at each pixel and therefore the ability to detect dim or rapidly changing phenomena with a higher signal-to-noise ratio. The trade-off for this increased capability is a dramatic increase in the complexity of algorithms used to reconstruct the desired datacubes.

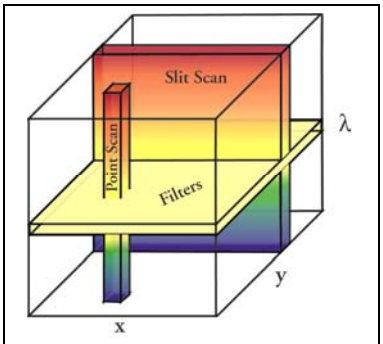

Figure 1. Schematic diagram of the spectral and spatial information collection per measurement for standard imaging spectrometers.

3. CTS Imaging Model

The goal is to reconstruct spectral slices through a 3-D spectral datacube by acquiring multiple 2-D projections of that cube. In this way, CTS systems are analogous to standard tomographic systems (e.g., x-ray CT systems) used for whole body imaging. In standard x-ray tomography, such projections are acquired by moving an x-ray source past a 3-D object and collecting the transmitted signal with a detector moving in the opposite direction (See Figure 2).

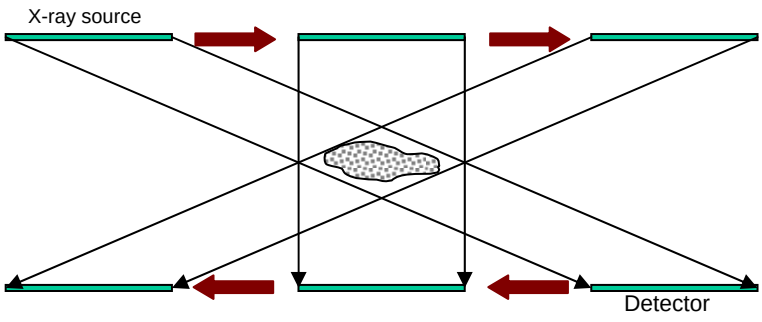

Figure 2. Schematic diagram of traditional computed tomography system.

The fundamental difference between standard x-ray tomography and chromotomography is that the 3rd dimension of the latter's object cube is spectral rather than spatial. In CTS, a dispersive element is used to project a 3-D spectral datacube onto a 2-D spatial plane (e.g., focal plane array). Figure 3a provides a schematic representation of such spatial-spectral projections. In order to reconstruct an estimate of the object cube, projections from multiple view angles are required. For a CTS, variations in projection angle are accomplished by changing the amount or orientation of spectral dispersion. Figure 3b shows a CTS which incorporates a rotating direct vision prism to create the later effect. As the prism rotates, the image from a single undeviated wavelength (shown in green) remains fixed while spectral data from shorter and longer wavelengths rotate about its fixed position. Using this method, a single datacube projection is collected per integration time.

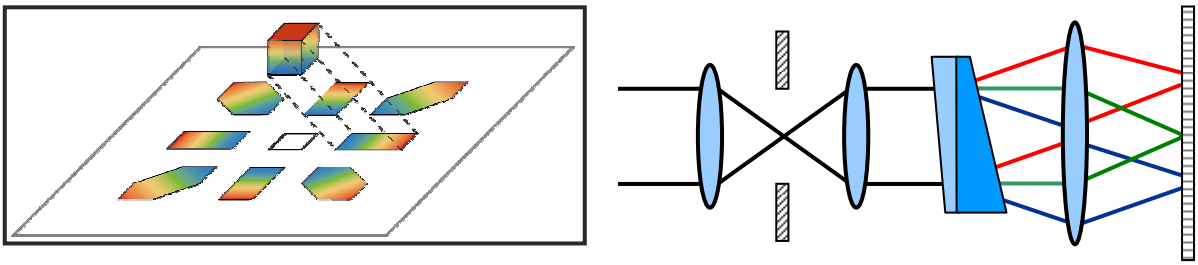

(a) (b)

Figure 3. (a) Projection of 3-D (2 spatial, 1 spectral) datacube onto a 2-D plane (e.g., focal plane array). **(b)** Schematic diagram of CTS incorporating a direct vision prism.

A 2-D spatial projection is simply an integration of signal along a series of parallel lines running through a 3-D object. Such projections can be described mathematically by

$$g(p,\phi) = \int_{\infty} d^2 r \; f(\mathbf{r})\delta(p - \mathbf{r}\cdot\hat{\mathbf{p}}) \qquad (1)$$

where $\hat{\mathbf{p}}$ is the unit vector defined by $\hat{\mathbf{p}} = (\cos\phi, \sin\phi)$. The delta functions define the lines over which the integration occurs (Figure 4).

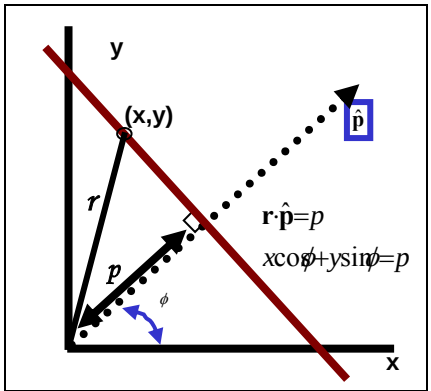

Figure 4. Definition of terms

Figure 5 shows examples of several 1-D projections through a simple 2-D object. As mentioned above, spatial-spectral projections are achieved through the use of dispersive elements. If one considers that the CTS in Figure 3b shifts a spectral image for every wavelength by an amount proportional to the spectrometer constant (μ) then a dispersed image may be represented as the integration of all such shifted spectral images.

$$g(x,y,\phi_m) = \int_{\lambda} f(x,y,\lambda) * \delta(x - [\lambda - \lambda_0]\mu\cos\phi_m, y - [\lambda - \lambda_0]\mu\sin\phi_m) \qquad (2)$$

Put more succinctly,

$$g(\mathbf{x},\phi)=\int_R f\left(\mathbf{x}-\mu(\lambda-\lambda_0)\mathbf{p}_\varphi,\lambda\right)d\lambda \text{where}, \mathbf{x}=[x_1,x_2], \phi=\text{projection angle},$$
$$\mathbf{p}_\varphi=[\cos\phi,\sin\phi], \mu=\text{spectrometer constant} \tag{3}$$

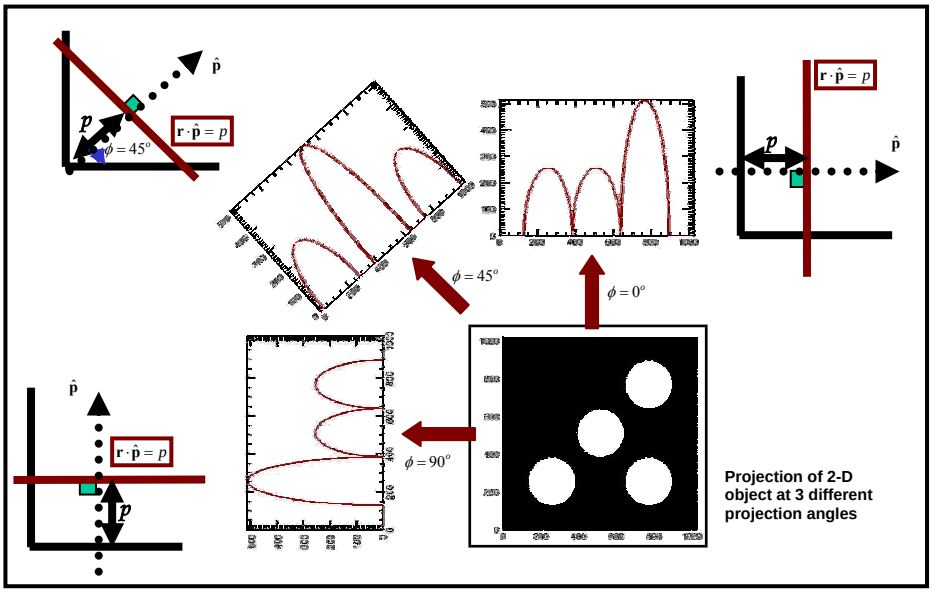

Figure 5. Example of 1-D projections through 2-D object.

The reconstruction algorithms described within this document are concerned primarily with the spatial frequency representations of the object cube [$F(\boldsymbol{\xi},\lambda)$] and projection images [$G(\boldsymbol{\xi},\phi)$]. In the discrete imaging model, the projection angles, wavelengths and spatial frequency coordinates are sampled as follows:

$$\phi_m=\frac{2\pi m}{M}, 0\le m<M \qquad \lambda_n=\frac{n}{\mu}, 0\le n<N \qquad \xi_k=\left(k_1\xi_1 \quad k_2\xi_2\right), 0\le k_1,k_2<K$$

where, M is the total number of projections, N is the total number of spectral bands and K is the total number of spatial samples. In terms of linear algebra, the spatial frequency representations of the projection images and object cube are related by means of the system transfer function (STF), **A**. Specifically, for each spatial frequency, $\boldsymbol{\xi}_k$,

$$\mathbf{G}_{\xi_k}=\mathbf{A}(\boldsymbol{\xi}_k)\mathbf{F}_{\xi_k} \tag{4}$$

where, $\mathbf{G}_{\boldsymbol{\xi}\mathbf{k}}$ is a vector in $\mathbf{C}^{\mathbf{M}}$ whose m$^{\text{th}}$ component is $\mathbf{G}^{\#}(\xi_k,2\pi m/M)$

$\mathbf{A}(\xi_k)$ is an M x N matrix whose (m, n)th coefficient is $Exp[-2\pi i n \xi_k \bullet p_m]$

$\mathbf{F}_{\xi k}$ is a vector in $\mathbf{C}^N$ whose nth component is $\mathbf{F}(\xi_k, n/\mu)$

3.1 The Missing Cone

As mentioned above, the work presented here focuses on CTS systems which use direct vision prisms to generate projections of spectral datacubes (See Figure 3). Such systems have been thoroughly described in by Mooney et al.[1] For these systems, the projection angle ϕ is sampled through a simple rotation of the prism and thus varies in orientation only. This fact has profound implications on one's ability to properly reconstruct an estimate of the spectral datacube from a set of projection images. To understand this limitation, we again look to x-ray tomography. A fundamental theorem of tomographic imaging is the Central Slice Theorem. This theorem states that the 2-D Fourier Transform a single Radon Projection of a 3D object is equivalent to a slice through the object's 3-D Fourier Transform. Figure 6 shows an example of the equivalent Central Limit Slice theorem for a 2-D object.

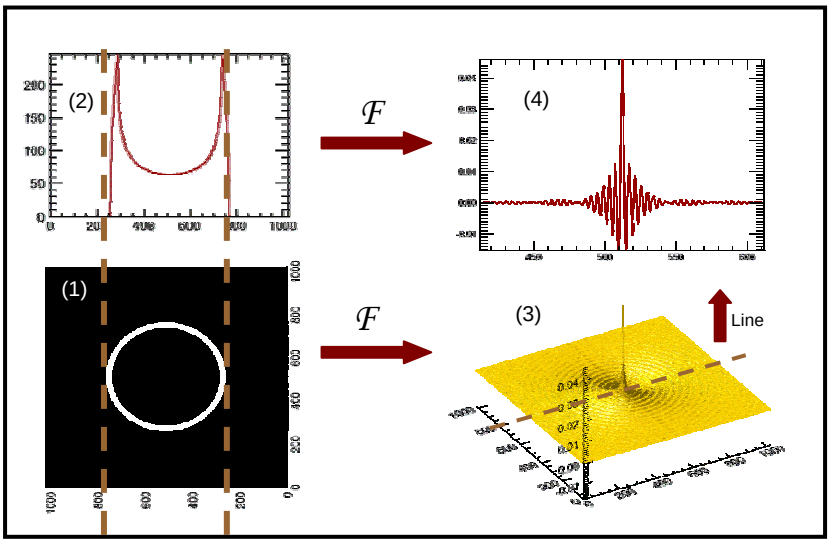

Figure 6. 2-D example of the Central slice theorem. **(1)** 2-D object. **(2)** The 1-D spatial projection of (1). **(3)** 2-D Fourier Transform of the object. **(4)** 1-D Fourier Transform of (2). Note that the 1-D Fourier Transform of the 1-D projection is equivalent to a line profile through the center of the 2-D Fourier Transform of the object, itself.

This theorem suggests a fundamental limit on our ability to accurately reconstruct datacube estimates from a limited set of projection images. For a CTS system which relies on the rotation of a direct vision prism to generate projection images, the magnitude of the projection angle remains fixed while the orientation varies from 0 to 2π. To see how this limits our ability to perform reconstructions, we must considered the 3-D Fourier Transform (2 spatial frequency and 1 spectral frequency) of the spectral datacube

(**F**). The Central Slice Theorem states that the 2-D Fourier Transform of each projection image corresponds to a slice through **F**.[3] This slice passes through the origin at an angle equal in magnitude and orientation to that of the projection angle. Figure 7 shows the effect of increasing numbers of projections on the sampling of the spatial and spectral frequencies of **F**. It is apparent that by using prism rotations to sweep out projections, a large subset of spatial and spectral frequencies will never be sampled. The missing region corresponds to a cone with its vertex at the origin of the spatial and spectral frequencies and is thus known simply as the missing cone.

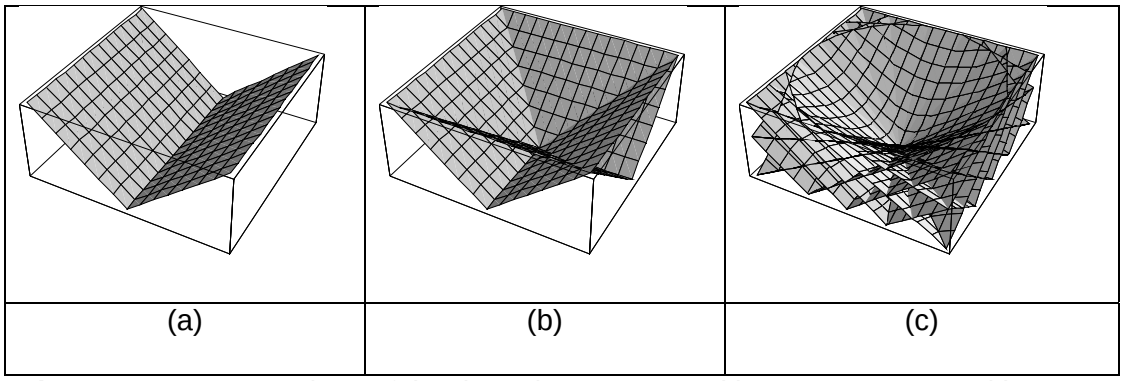

Figure 7. Representations of the data planes captured by a CTS system with a 45 degree projection angle for (a) 2 opposing projection angles, (b) 2 pairs of orthogonal projection angles, (c) multiple projection angles. The central empty space (Missing cone) corresponds to spectral and spatial frequency not captured by the CTS.

4. Object Cube Reconstructions

As seen from Equation (4), the forward imaging model of the CTS can be described in terms of linear algebra with the 3-D object cube related to the set of 2-D projection images by a system transfer function. The most direct method of reconstructing a datacube estimate from a set of projections would then be

$$\mathbf{F}_{\xi_k} = \mathbf{A}^{-1}(\xi_k)\mathbf{G}_{\xi_k} \tag{5}$$

Due to the fact that $\mathbf{A}(\xi_k)$ is a large, rectangular and often single matrix, its inverse is calculated using singular value decomposition (SVD) methods. The SVD of $\mathbf{A}(\xi_k)$ can be written as

$$\mathbf{A} = \mathbf{U}\mathbf{\Sigma}V^{\mathbf{H}} \text{ where, H indicates Hermitian adjoint} \tag{6}$$

In Equation (5), **U** is an M x N matrix of othonormal column vectors representing the object space singular vectors. **V** is an N x N matrix of orthonormal column vectors representing the image space singular vectors. **Σ** is an N x N diagonal matrix whose

diagonal elements quantify the influence of a given object vector on a corresponding image vector.[3] If A is nonsingular, the matrix inverse of **A** is defined as

$$\mathbf{A^{-1}} = \mathbf{V\Sigma}^{-1}\mathbf{U}^{\mathbf{H}} \; where, \Sigma^{-1} = \left(\sigma_0{}^{-1}, \sigma_1{}^{-1}, \ldots, \sigma_{N-1}{}^{-1}\right) \tag{7}$$

and a unique solution to Equation (4) exists:

$$\mathbf{F}_{\xi} = \mathbf{A^{-1}}(\xi)\mathbf{G}(\xi) \tag{8}$$

4.1 Moore-Penrose Inverse (MPI)

If A is rank deficient (Rank(A) = K < N) then $\mathbf{\Sigma} = \mathbf{\Sigma_K} = \left(\sigma_0, \sigma_1, \ldots, \sigma_K, 0, \ldots, 0\right)$ and a direct inverse is not possible. In this case one may use a pseudoinverse to generate an object cube estimate. For example, the Moore Penrose Inverse is defined as

$$\mathbf{A}^{+} = \mathbf{V\Sigma}^{+}\mathbf{U}^{\mathbf{H}} \; where, \Sigma^{+} = \left(\sigma_0{}^{-1}, \sigma_1{}^{-1}, \ldots, \sigma_K{}^{-1}, 0, \ldots 0\right).^{3} \tag{9}$$

The object cube estimate then becomes,

$$\mathbf{F}_{\xi}{}^{+} = \mathbf{A}^{+}(\xi)\mathbf{G}(\xi) \tag{10}$$

Due to the lack of data reconstructed from missing cone frequencies, object cube estimates generated using MPI suffer from significant reconstruction artifacts. This is especially true in the low spatial and high spectral frequency regimes (See Figure 7).

4.2 Subspace Constraint Algorithm

The Subspace Constraint Algorithm (SCA) assumes a set of spatial frequencies (Δ) exist for which the system transfer function [**A**(ξ)] has full or near full rank (i.e., region outside or just inside the missing cone). An inverse or pseudoinverse is calculated at each spatial frequency within Δ and a set of spectral principal components is calculated from these reconstructed spectra ($\mathbf{F}_{\xi}$). It is assumed that these spectral principal components sufficiently represent all spectra within the remaining object cube. For all spatial frequencies outside Δ, the range of the transfer function is thus limited to the subspace spanned by these principal components. A detailed description of this algorithm can be found in reference [[4]]. In brief, the algorithm proceeds as follows:

1. $\mathbf{F}_{\xi}{}^{+} = \mathbf{A}^{+}(\xi)\mathbf{G}(\xi)$ for all $\xi \in \Delta$ (collectively, F_{Δ})
2. Principal component decomposition : $F_{\Delta} = W'DX^{H}$
3. For all $\xi \notin \Delta$, the range of A is limited to the subspace spanned by the spectral principal components (W):

a. $A_0(\xi) = A(\xi)W$

b. $(F_0^+)_\xi = A_0^+(\xi)G_\xi$

c. $F_W^+ = WF_0^+$

4. Solutions for the two frequency subsets are combined to form the complete object cube estimate, $F = F^+ + F_w^+$

4.3 Projection onto Convex Sets

It is apparent that in order to more accurately reconstruct a datacube from a limited set of projections, an attempt must be made to estimate the signal within the missing cone. Numerous methods have been demonstrated for this purpose. One accepted method is the use of Projection onto Convex Sets (POCS).[5] POCS assumes that:

(1) The original datacube can be composed on 2 components, $\mathbf{f} = \mathbf{f}^0 + \mathbf{f}_N$ where $\mathbf{f}^0$ is the known part (outside the missing cone) and $\mathbf{f}_N$ is the unknown part (associated with the null space of **A)** and

(2) The spectrum at each spatial frequency is well represented by the set of spectral principal component calculated from $\mathbf{f}^0$

A detailed description of this algorithm can be found in [5]; therefore, we will only reiterate their suggested procedure. On each iteration,

1. Calculate the Moore Penrose Inverse $\mathbf{F}_\xi^+ = \mathbf{A}^+(\xi)\mathbf{G}(\xi) \Rightarrow \mathbf{f}^0$
    a. When computing the SVD $\mathbf{A} = \mathbf{U}\mathbf{\Sigma}V^{\mathbf{H}}$, store $\mathbf{V}_{\text{n-k}} : \mathbf{V}_{\text{n-k.}}$ is formed by replacing the first k columns of **V** with zero column vectors [k =rank(**A**)].
2. Compute the covariance matrix, $\mathbf{R}_{\mathbf{F}_\Delta\mathbf{F}_\Delta}$
3. SVD: $\mathbf{R}_{\mathbf{F}^0\mathbf{F}^0} = \mathbf{U}\mathbf{\Sigma}V^H$
4. Reduce the number of eigenchroma to L < N based upon percent contribution: $\mathbf{U} \rightarrow \mathbf{U}_\text{L}$
5. On each iteration:
    a. $\mathbf{f}_1^k = \mathbf{P}^\mathbf{f}\mathbf{f}^k \Rightarrow \mathbf{U}_\mathbf{L}\left(\mathbf{U}_\mathbf{L}^T\mathbf{F}^k\right)$ (project the estimate onto the eigenchroma)
    b. $\mathbf{f}_2^k = \overline{\mathbf{P}}^A\mathbf{f}_1^k \Rightarrow \mathbf{V}_{\mathbf{n-k}}\left(\mathbf{V}_{n-k}^H\mathbf{f}_1^k\right)$ (project the result onto the null space of A)
    c. $\mathbf{f}^{k+1} = \mathbf{f}^0 + \mathbf{f}_2^k$ (apply additive correction to Moore Penrose Inverse)

4.4 Filter Image Constraints

As noted above, the CTS inversion problem is compounded by the missing cone of spatial and spectral frequency information. SCA and POCS attempt to best estimate this missing data by constraining estimates to have a given MPI solution and consistent

spectral statistics inside and outside the missing cone.[4,5] Additional constraints are made available with some simple system modifications and minimal additional datasets. Specifically we investigated the strength of filtered image constraints on the CTS inversion problem. By introducing a spectral filter mechanism (e.g., filter wheel, tunable filters, etc) in the optical path and removing the CTS dispersion, a set of filtered images can be acquired immediately after the CTS projection images. Assuming the scene remains stationary over the course of this additional collection time, these filtered images may be used to further constrain datacube estimates.

The bandpasses used throughout our study are shown in Figure 8. In order to maximize the signal to noise ratio and minimize integration times, the spectral bandpasses must be made as broad as possible. On the other hand, the quality of the filtered image constraint is vastly improved by using narrow, independent (non-overlapping) spectral filters. In fact, as the bandpass of these filters narrows, the system tends toward a standard imaging spectrometer. This trade space was not explored during our study. Instead, we selected filters which would have operational significance when used independently of the CTS system. In other words, we were attempting to marry 2 separately defined spectral imagers: (1) a multispectral (7-10 bands) instrument which might be used for applications such as scene characterization, atmospheric correction, or weather prediction and (2) a CTS imager used to generate higher fidelity spectral products. Thus, the multispectral filters used for CTS reconstruction constraints were not optimized for this reconstruction purpose. In an operational system, both the primary and secondary applications of the spectral filters should be considered when specifying the filter properties.

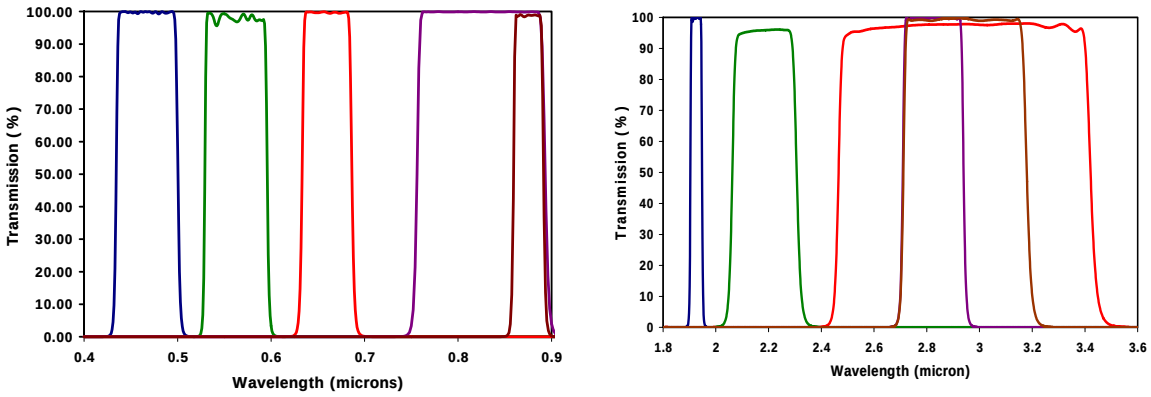

Figure 8. Spectral bandpass filters for **(a)** visible and **(b)** SWIR constraints, respectively.

One method for utilizing filtered images is to apply a filtered image constraint to the final result of a standard reconstruction algorithm such as MPI, SCA or POCS (referred to throughout this text as MPIFC, SCAFC or $SCA_{FILT,}$ and POCSFC or $POCS_{FILT}$, respectively). Another method explored is to apply the filtered image constraints within the standard algorithm itself. Specifically, the filtered image constraint was incorporated into the POCS iterations (referred to throughout this text POCSPCFC or $POCS_{PCFILT}$). In

either case, the current datacube estimate is used in combination with the filter transmission curves, **t**, to generate a set of estimated filtered images, $\hat{\mathbf{s}}$.

$$\hat{\mathbf{s}}_i = \boldsymbol{\tau}_i{}^T \hat{\mathbf{f}} \tag{11}$$

The differences between these filtered image estimates and the ground truth filtered images are then calculated [$\vec{\boldsymbol{\varepsilon}}_i = \hat{\mathbf{s}}_i - \mathbf{s}_i$] and distributed across the spectral bands.

$$\mathbf{E}_{in\_band} = -\vec{\boldsymbol{\varepsilon}}_i \frac{\boldsymbol{\tau}_i}{\sum_\lambda [\boldsymbol{\tau}_i]_\lambda} \text{ and } \mathbf{E}_{out\_of\_band}(\lambda) = \vec{\boldsymbol{\varepsilon}}_i \frac{1-\boldsymbol{\tau}_i}{\sum_\lambda 1-[\boldsymbol{\tau}_i]_\lambda} \tag{12}$$

The reconstruction improvements achieved from filtered imaging constraints are dependent upon the order in the filters are applied. We chose to work in order from the broadest to narrowest spectral bandpasses. This assumes that the accuracy improvements associated with narrow spectral filters are greater than from broad filters due to less ambiguity in the spectral redistribution of errors. After looping through all spectral filters, the datacubes are further constrained by the principal components calculated from outside the missing cone. For MPIFC, SCAFC, and POCSFC, this transformation is performed for all but the last iteration. The removal of the PC constraint from the final iteration is an attempt to preserve anomalous spectra which may not be well represented by the PCs.

Input from Standard Reconstruction Algorithm→ $\hat{\mathbf{f}}$

1. Loop through filters, i=1,…N:

$$\hat{\mathbf{s}}_i = \boldsymbol{\tau}_i{}^T \hat{\mathbf{f}}$$

$$\vec{\boldsymbol{\varepsilon}}_i = \hat{\mathbf{s}}_i - \mathbf{s}_i$$

$$\mathbf{E}_{in\_band} = -\vec{\boldsymbol{\varepsilon}}_i \frac{\boldsymbol{\tau}_i}{\sum_\lambda [\boldsymbol{\tau}_i]_\lambda}$$

$$\mathbf{E}_{out\_of\_band}(\lambda) = \vec{\boldsymbol{\varepsilon}}_i \frac{1-\boldsymbol{\tau}_i}{\sum_\lambda 1-[\boldsymbol{\tau}_i]_\lambda}$$

$$\hat{\mathbf{f}}' = \hat{\mathbf{f}} + \mathbf{E}_{in\_band} + \mathbf{E}_{out\_of\_band}$$

2. $\hat{\mathbf{f}}' = \mathbf{W}\mathbf{W}^T \hat{\mathbf{f}}'$

Repeat steps 1&2 for N iterations.

Figure 9. Step by step calculations for the Filter Constraint Algorithm (FC)

5. Scene Simulation

In order to evaluate the applicability of CTS systems to space based applications, we first generated a set of scene simulations. Table 1 provides a summary of the scenes generated by SciTec, Inc as part of this effort.[6] For each scene, a nominal geostationary orbit was assumed and both surface leaving and at-sensor radiance values were provided. Throughout this report, results are presented for the Iran and Israel data sets. The Iran 256x256 data is composed of 12 datacubes labeled A thru L and the 512x512 data is composed of 5 datacubes labeled c1, q1, q2, q3, and q4. For the Israel data, 8 datacubes labeled n_1 thru n_8 were used.

Table 1. Summary of simulated scenes generated for this project.

		# of Cubes	GSD	Spatial Dimensions	Spectral Range(microns)	Spectral Bands
Nadir	**Israel_North**	8	75	256	0.4 to 0.9	32
	Iran	5	120	512	1.9-3.4	32
		12		256		
Off Nadir	**Iran**	1	360	256 x 256	1.9-3.4	32
	Israel_North	1				
	Madison4AS	1				
	North Korea	1				
	Pakistan	1				

SciTec was also able to provide material map estimates for each simulated scene. The accuracy of these material maps is greatest for those scenes generated with a nadir looking sensor. These material maps were used to assess the accuracy of bulk classification algorithms applied to reconstructed datasets. See Figure 10 and Figure 11 for material maps associated with the Nadir viewing Israel_North datacube #8 and Nadir viewing Iran datacube C, respectively.

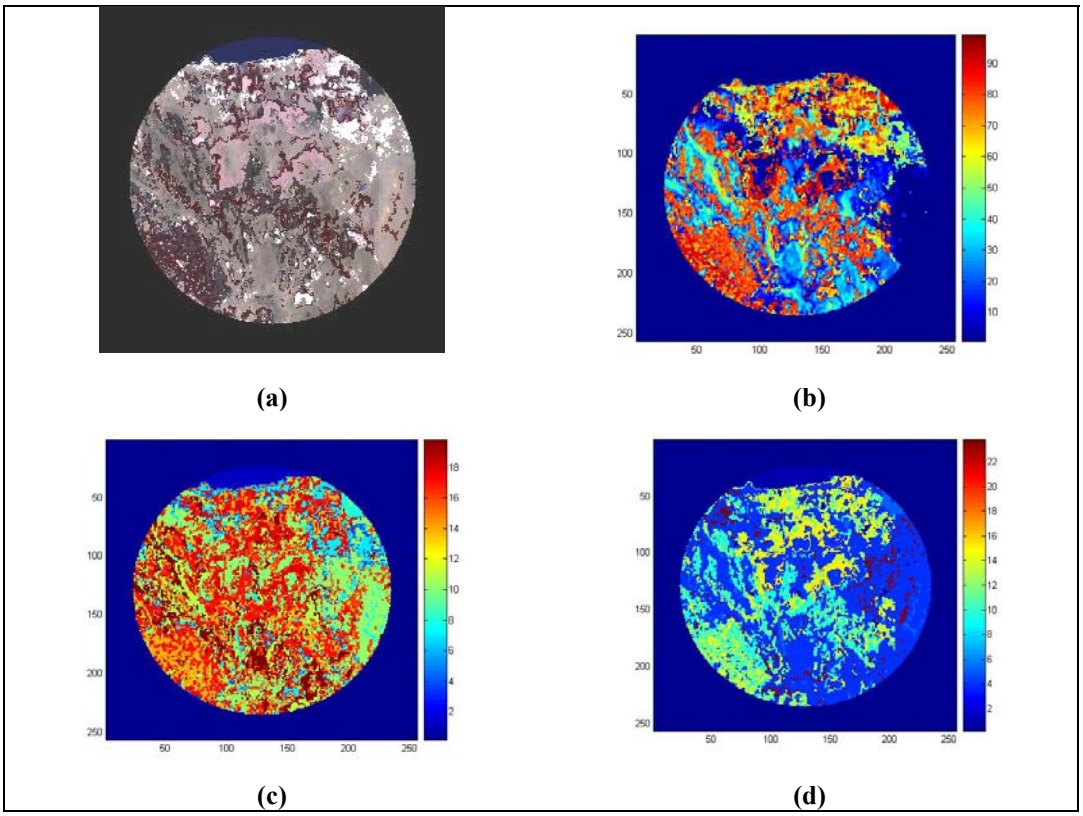

Figure 10. (a) RGB image of Nadir-viewing Israel North ground truth datacube #8. (R: 0.58 μm, G: 0.50 μm, B:0.44 μm) **(b**) Percent of the primary material (Each ground sample is composed of only 2 materials). **(c)** Index of primary material **(d)** Index of secondary material. Refer to Table A-1 in Appendix A for corresponding material names.

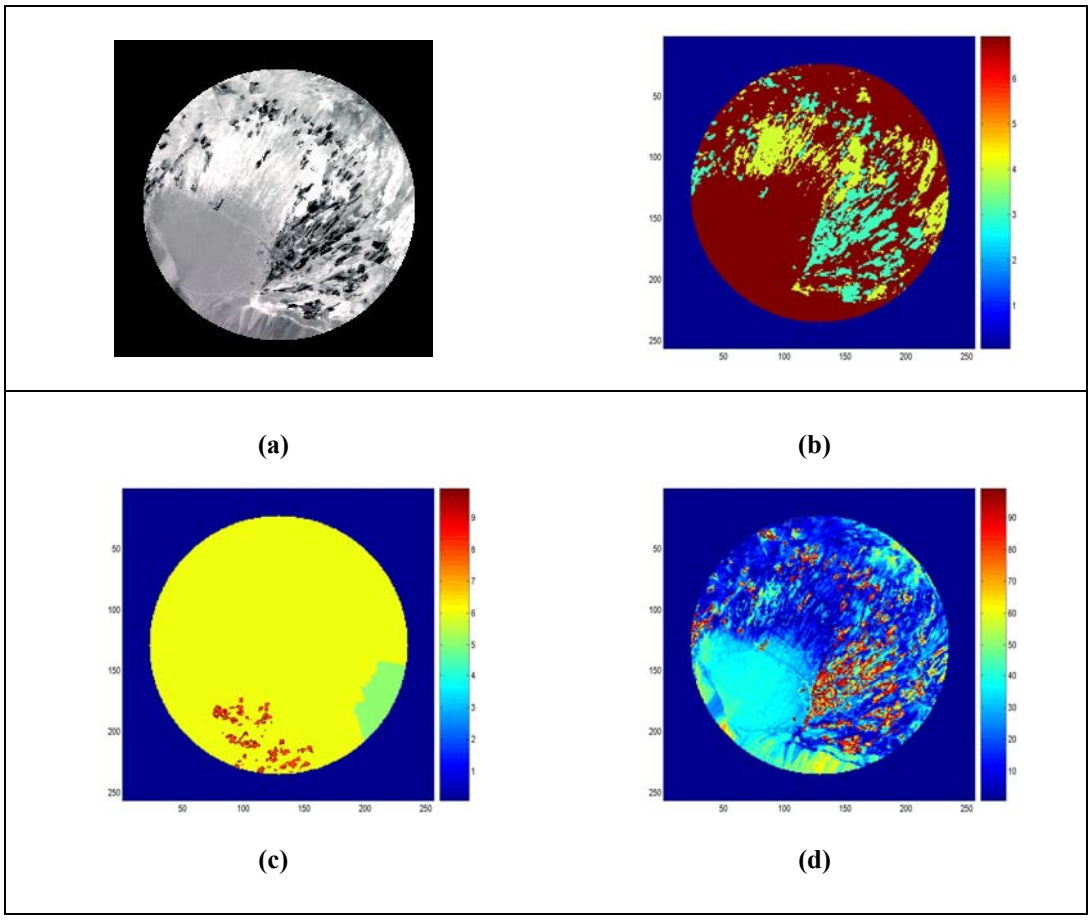

Figure 11. (a) False color image of Nadir-viewing Iran ground truth datacube C. (R: 2.44 μm, G: 2.2 μm, B: 2.02 μm) **(b)** Percent of the primary material (Each ground sample is composed of only 2 materials). **(c)** Index of primary material **(d)** Index of secondary material. Refer to Table A-2 in Appendix A for corresponding material names.

6. Simulation of Potential Error Sources

Part of this effort focused on assessing the degradation of reconstruction performance due to certain anticipated error sources: namely, detector noise and platform motion. CTS projection images were thus generated with and without these error sources.

6.1 Gaussian Noise

Detector noise was modeled as a Gaussian random distribution of errors added to the projection images prior to reconstruction. This noise term was added such that the signal to noise ratio ranged from 10 to 400. This was the only noise term considered with

respect to the detector. We did not look at different noise models such as Poisson distributions.

6.2 Jitter

Here, jitter is defined as the platform motion induced by such active components as gyros, pumps and motors. This movement is translated to the imaging telescope which in turn blurs the sensed image. Jitter can produce translations or rotations in 3-space, making it difficult to correct. In order to study the effect jitter has on a CTS system 2-D translational jitter is introduced in the cross-track and along-track directions.

A jitter model was created to resemble Parametric Technology Corporation's Pro-Engineer's dynamic motion/structural analysis module.[7] The model includes the structural dynamics of a representative platform and the dynamics of the telescope structure itself. The forcing functions along with the frequency response of the structure are used to produce pointing vectors for the telescope at a sample rate of 70 Hertz. These pointing vectors are then used to produce affine transform coefficients which assume the sensor is in a nominal geosynchronous orbit.

The jitter translation positions are given as degree latitude and longitude coordinates referenced to the center of the detector. The coordinates are then transformed into pixel translations with respect to the ground sample distance (GSD). The positions are first differentiated leaving only the relative displacement between each time step. Each translation is then converted from degrees to kilometers assuming the earth's radius is 6,378 km. The latitude spacing is scaled by:

$$scaleLat = \frac{EarthRadius \cdot \pi}{180}$$

and the longitudinal spacing is scaled by:

$$scaleLong = scaleLat \cdot \cos\left(\frac{position_1 \cdot \pi}{180}\right),$$

where the cosine of the starting latitude position accounts for the longitudinal spacing at the given latitude due to the curvature of the earth. Each translation's latitude and longitudinal position change is then multiplied by its appropriate scaling factor. The new values are then divided by the given GSD to scale from kilometers to pixels on the detector. Now the sampling rate is taken into account by taking the CTIS projection frame rate in seconds and multiplying it by the jitter sample frequency of 70 Hz and inverting this result. The jitter translations are then up-sampled or down-sampled according to the required jitter samples per frame or projection. Once the jitter translations are converted to pixel translations they can be scaled in order to vary their values and study the effects of various magnitudes of jitter. The maximum and mean

distance in pixels from the origin for latitude and longitudinal translations are shown in Figure 12 and Figure 13, respectively.

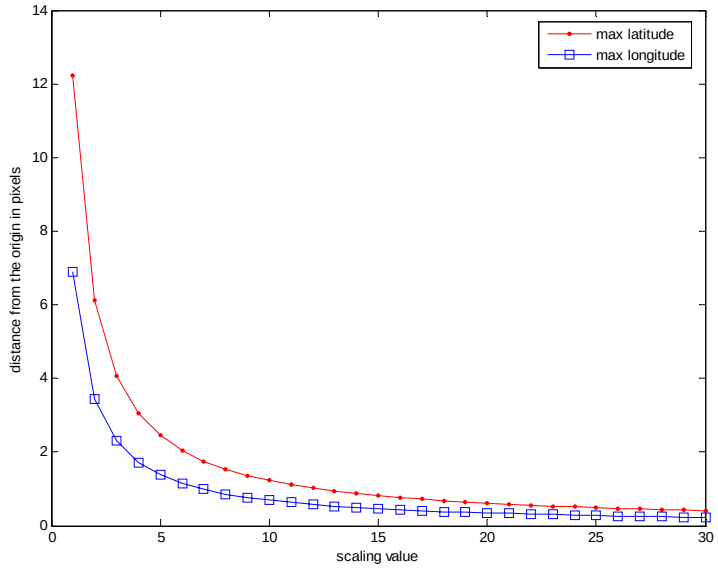

Figure 12 Plot of maximum displacement from the origin for shifts in latitude and longitude.

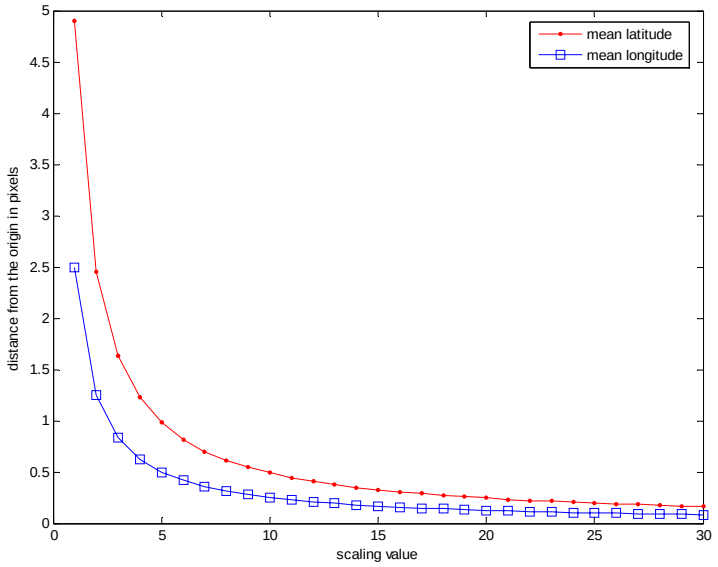

Figure 13. Plot of mean displacement from the origin for shifts in latitude and longitude.
.

In addition, the maximum and mean radial distance in pixels from the origin are shown in Figure 14 while the maximum and mean radial distance in pixels between consecutive time steps are shown in Figure 15.

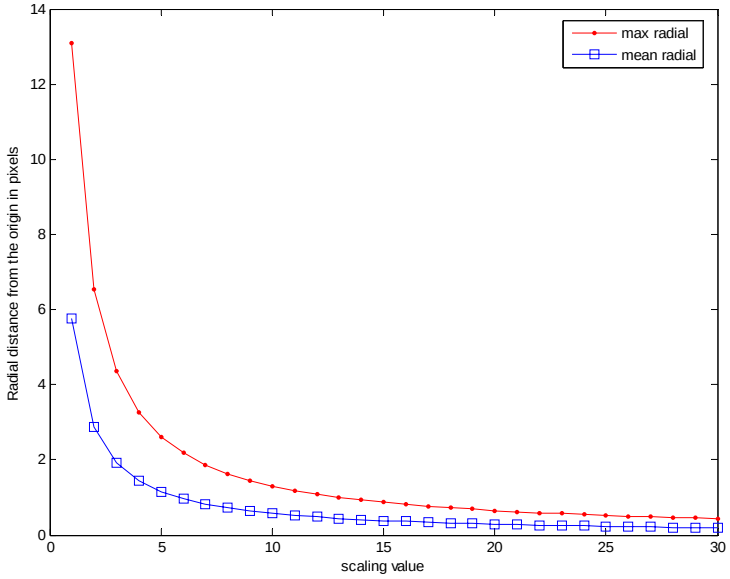

Figure 14. Max and mean radial displacement from the origin.

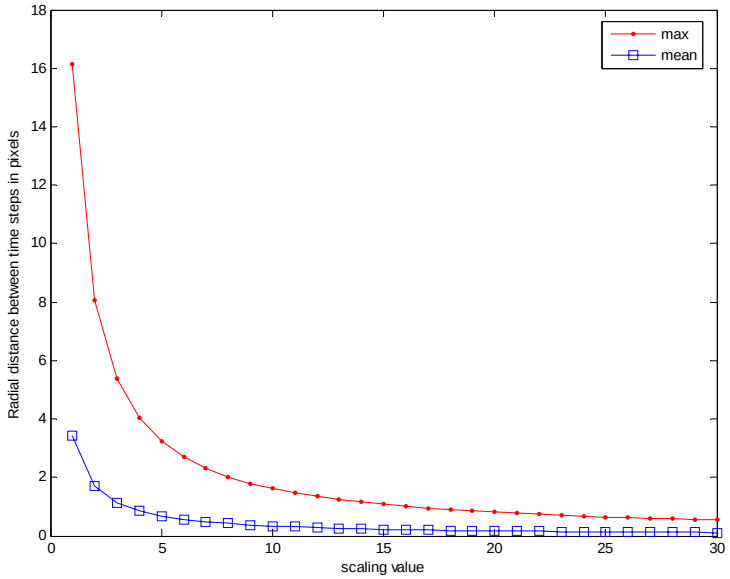

Figure 15. Max and mean radial displacement between consecutive time steps.

6.3 Generation of Jittered Datacubes

In order to evaluate a range of jitter magnitudes the scale plots were visually interpreted to have an effective scale factor range of 1 to 10 since after a scale value of 10 the jitter

statistics are approximately constant. In order to account for sub-pixel movement pixel fractions are used to create mixed pixels. This concept is illustrated in Figure 16, where a translation of 0.25 pixels to the north and 0.5 pixels to the east are called for. The image on the left shows the percentages or fractions of pixel values used to create the new center pixel in the right image. The pixel fractions are multiplied by the pixel values and then summed to create the new pixel.

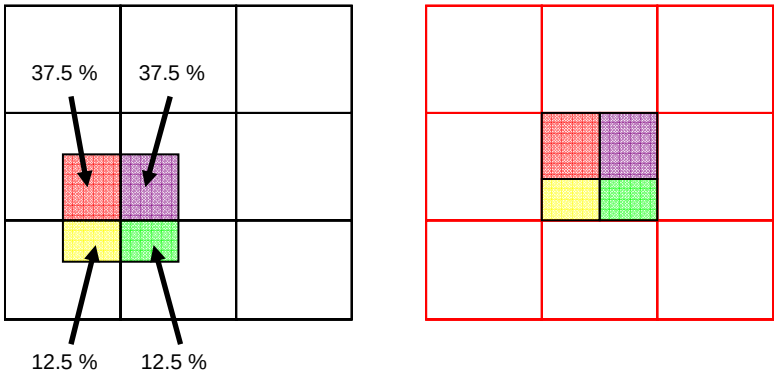

Figure 16. Illustration of how a sub-pixel translation is handled

The end product of the jitter exercise is a spectral data cube that has been reconstructed with the various reconstruction algorithms used in this study. Therefore, a function was created to jitter the projection images at the beginning of each reconstruction algorithm. The magnitude scaling factor is used an input to the function. The filtered images used within the filter constrained algorithms also have appropriate levels of jitter applied. As an example of the effects of jitter, reconstructions using the POCSFCPC for jittered projections are shown in Figure 16. Each scene has an imbedded target in the upper left quadrant; an enlarged sub-region containing this target is pictured in the second row. Each column represents a different scale parameter in which the overall jitter magnitudes decrease from left to right. As the jitter increases in magnitude the scene energy is spread further and additional ringing is apparent.

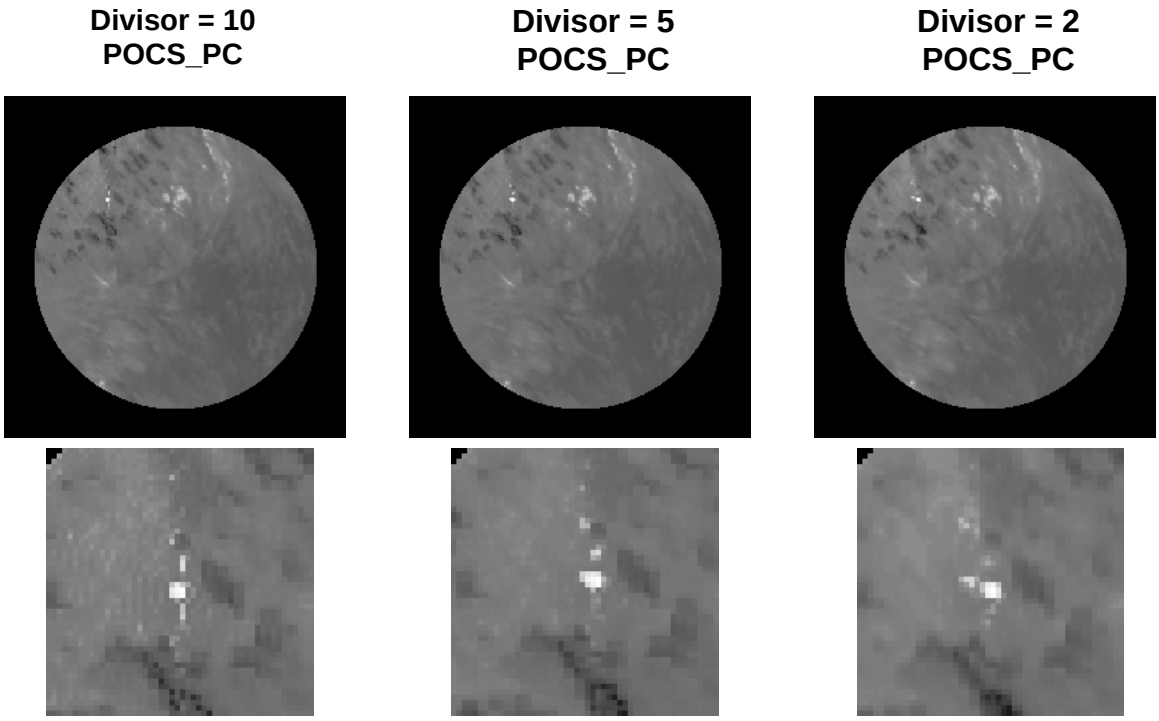

Figure 17. Examples of reconstruction artifacts due to jitter.

7. Reconstruction Results

Representative reconstruction results are presented in this section from 2 datasets: (1) the nadir-viewing Israel North Datacube #8 (Figure 10) and (2) the nadir viewing Iran Datacube C (Figure 11). Within the remainder of this text, these datacubes will be referred to as simply Cube 8 and Cube C, respectively. These datacubes both consisted of 256 x 256 spatial samples and 32 spectral bands. Cube 8 covered the visible spectrum from 0.4-0.9 microns and had a GSD of 75m; while, Cube C covered the SWIR from 1.9-3.4 microns with a GSD of 120m. Three representative pixel locations were chosen from each datacube. Spectra from these locations will be used throughout this section to demonstrate the reconstruction accuracy associated with various reconstruction algorithms: namely, MPI, SCA, SCAFC, POCS, POCSFC, and POCSFCPC. The locations of these pixels and their material make-up are provided in Table 2.

Table 2. Material contributions for sample spectra used throughout this section for Cube 8 and Cube C.

	x	y	Primary	% Primary	Secondary	% Secondary
Cube 8	**115**	**35**	Water	0	Water	100
	157	**111**	Urban commercial	81	Concrete	19
	70	**138**	Broadleaf and brush mix	36	Compacted soil	64
Cube C	**73**	**158**	Rock	41	Silt-sand	59
	159	**150**	Rock	38	Silt-sand	62
	130	**98**	Rock	50	Silt-sand	50

7.1 MPI - Reconstruction Results

As was mentioned in the section entitled, "4.1 Moore-Penrose Inverse (MPI)", a MPI solution does not include signal from spatial and spectral frequency locations within the missing cone. This is apparent from the sample spectra shown in Figure 18. The effect is more pronounced in Iran Cube C; however, in both cases the loss of spectral fidelity demonstrates the need for advanced reconstruction algorithms. This report focuses on reconstruction results from SCA, POCS, filter constrained SCA and filter constrained POCS.

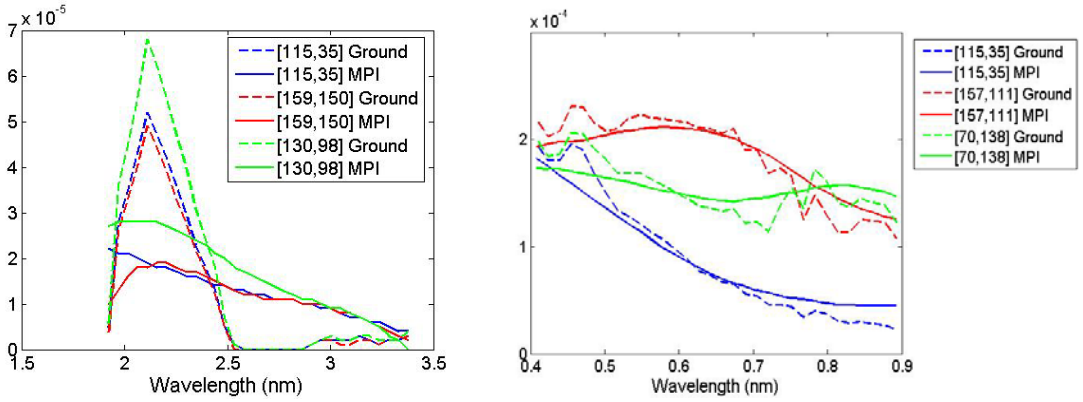

Figure 18. Representative spectra from 3 locations within the MPI reconstruction of **(a)** Cube C and **(b)** Cube 8, respectively.

7.2 SCA - Reconstruction Results

SCA attempts to improve the accuracy of datacube reconstructions by constraining the range of the system transfer function to include only those spectra represented by PCs derived from a subset of spatial frequencies outside the missing cone. See the Section Entitled, "4.2 Subspace Constraint Algorithm" for a complete description of this algorithm. SCA has several variables which may be changed to optimize the reconstruction results. Namely, one can adjust the region used for PC calculations as well as the number of these PCs used to constrain the range of the STF. Figure 19 shows reconstructed spectra from 3 spatial locations within the Cube 8 and Cube C. An increase in spectral frequency content is readily apparent in comparison with the MPI spectra of Figure 18. The spectra shown in Figure 19 were generated using 6 principal components for Israel North and 3 principal components for Iran, respectively. In each case the number of PCs minimized the spectral error between these reconstructed and ground truth spectra.

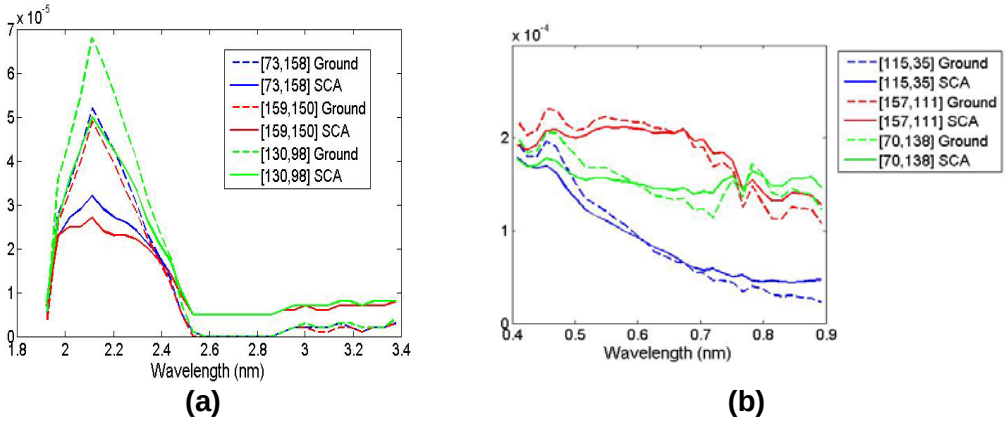

Figure 19. Representative spectra from 3 locations within the SCA reconstruction of the **(a)** Cube C and **(b)** Cube 8, respectively

7.3 POCS - Reconstruction Results

Reconstruction accuracy is improved by moving from the noniterative techniques such as SCA to an iterative algorithm such as POCS. This move of course comes at the expense of reconstruction speed. See the section entitled, "4.3 Projection onto Convex Sets" for a complete description of this algorithm. The expected improvement in reconstruction accuracy is readily apparent in the representative spectra shown in Figure 20.

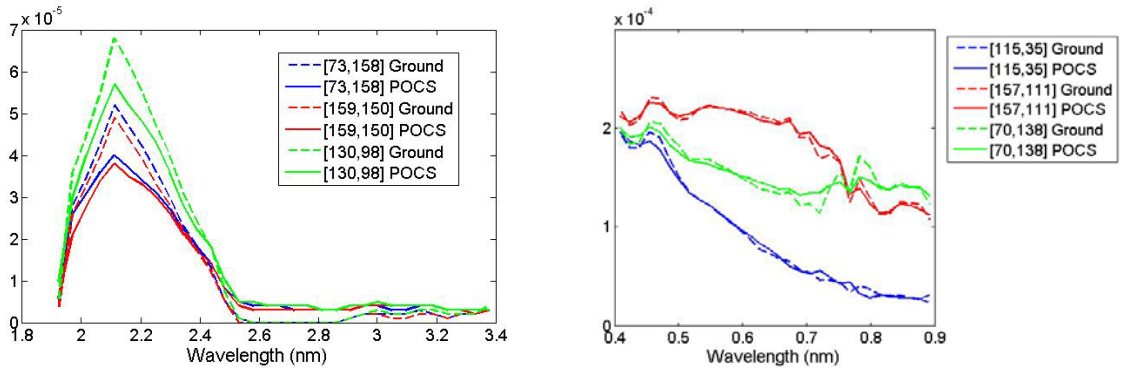

(a) **(b)**

Figure 20. Representative spectra from 3 locations within the POCS reconstruction of the **(a)** Cube C and **(b)** Cube 8, respectively

7.4 Filter Constrained SCA - Reconstruction Results

A goal of this LDRD was to investigate additional constraints designed to improve the accuracy of datacube estimates over standard reconstruction techniques. We were especially interested in investigating the potential improvements gained by applying filtered image constraints to the reconstruction algorithms developed by Mooney et al [SCA and POCS]. See the section entitled, "4.4 Filter Image Constraints" for a completed description of the filtered constraint algorithm. The spectra provided in both Figure 21 and Figure 22 clearly demonstrate the improvements in spectral accuracy gained through the inclusion of these new filter constraints.

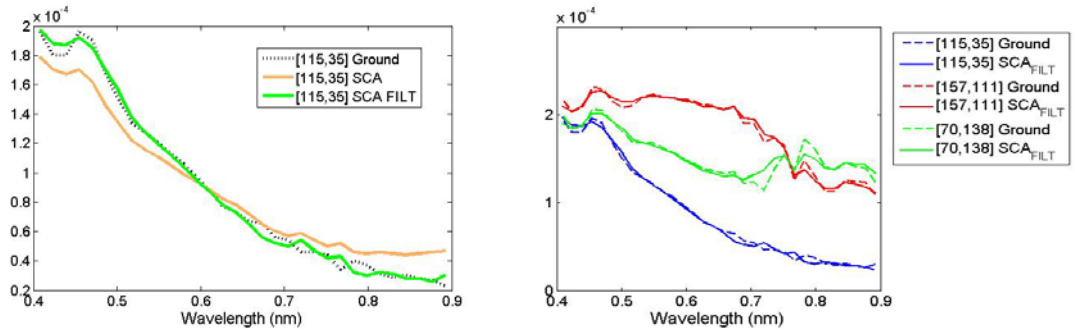

(a) **(b)**

Figure 21. (a) Comparison between SCA reconstruction and Filter constrained SCA for a single pixel location in Cube 8. **(b)** Representative spectra from 3 locations within the SCA reconstruction of Cube 8**.**

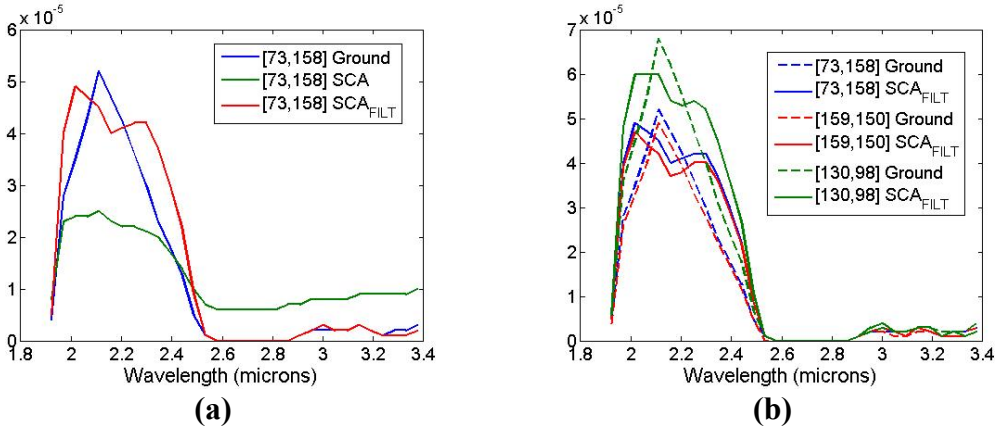

Figure 22. (a) Comparison between SCA reconstruction and Filter Constrained SCA for a single pixel location in Cube C. **(b)** Representative spectra from 3 locations within the SCA reconstruction of the Cube C.

7.5 Filter Constrained POCS - Reconstruction Results

For the results presented here, 10 iterations of the filter constraint algorithm were applied either as part of each POCS iteration (POCSPCFC) or after completion of the full POCS algorithm (POCSFC). Improvements over the standard POCS algorithm were seen for either implementation of the filter constraints. Although, the improvements were not as pronounced as for SCAFC, they were still noticeable (See Figure 23 and Figure 24)

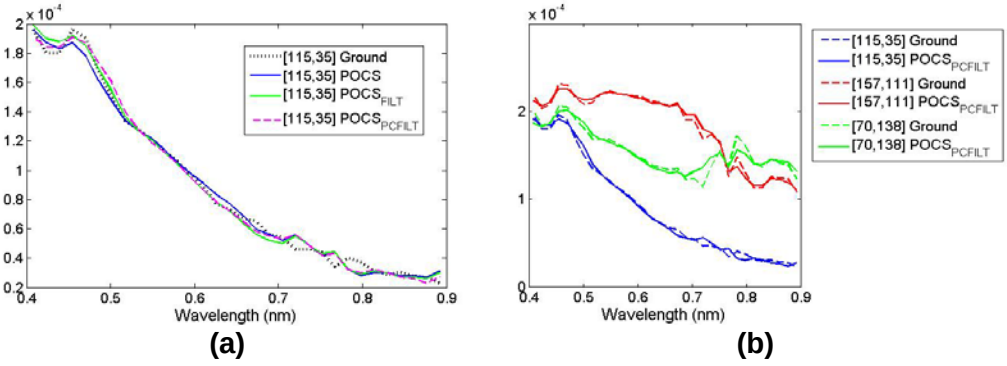

Figure 23. (a) Comparison between filter and non-filter constrained POCS reconstructions for a single pixel location. **(b)** Representative spectra from 3 locations within the PC Filter Constrained POCS reconstruction of the Cube 8 datacube**.**

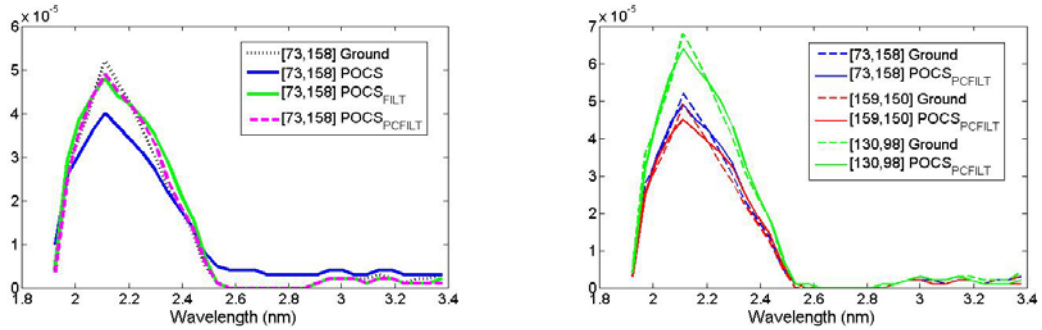

Figure 24. (a) Comparison between filter and non-filter constrained POCS reconstructions for a single pixel location in Nadir Iran Cube C. **(b)** Representative spectra from 3 locations within the PC Filter Constrained POCS reconstruction of the Nadir Iran Cube C.

7.6 Summary of Reconstruction Results

A summary of the reconstructed spectra presented in this section is provided in Figure 25 and Figure 26. From these figures it is readily apparent that filter image constraints do significantly enhance our ability to accurately reconstruct spectral estimates from projection images. Most notably, the performance of SCA dramatically improves with this technique, to the extent that it now provides comparable performance to the iterative POCS techniques. This is significant due to the time savings allowed by using a noniterative base algorithm itself.

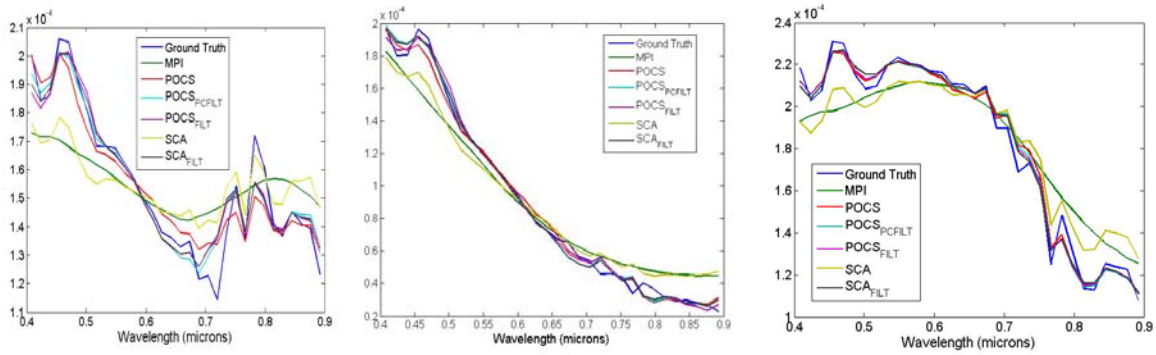

Figure 25. Comparative pots of reconstructed spectra from 3 spatial locations in the Cube 8: **(a)** [70,138], **(b)** [115,35], **(c)** [157,111]

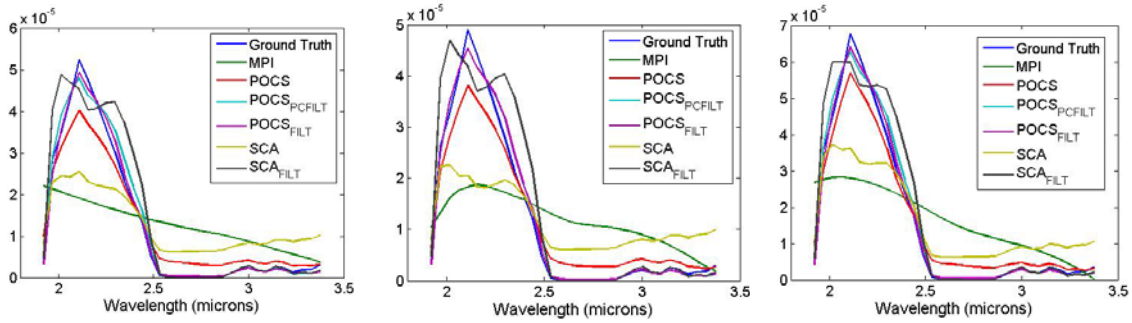

(a) **(b)** **(c)**

Figure 26. Comparative pots of reconstructed spectra from 3 spatial locations in the Cube C: **(a)** [73,158], **(b)** [159,150], **(c)** [130,98].

From these plots it would be difficult to adequately compare the performance differences between POCS, POCSFC and POCSPCFC. Instead, one can look at the mean spatial and spectral correlation statistics and mean spectral error associated with each datacube. Plots of these values with respect to the various reconstruction algorithms are provided in Figure 27 and Figure 28 for Cube 8 and Cube C, respectively. Mean spatial correlation is calculated by first determining the spatial correlation between the original and reconstruction datacubes on a band by band basis. These values are then averaged to provide a mean spatial correlation. In much the same way the mean spectral correlation is calculated on a per pixel basis and averaged over the entire datacube. The Mean Spectral Error (MSE) is defined as

$$MSE = \left\langle \frac{\sqrt{\sum_i (s_o - s_r)^2}}{\sqrt{\sum_i (s_o)^2}} \right\rangle \text{ where, } i = 1,2,...\text{Number of spectral bands} \qquad (13)$$

The plots in general show a trend of increasing accuracy from MPI to SCA, SCAFC, POCS, POCSFC, and finally POCSFCPC. Also, from these plots there does not appear to be a large difference between the 2 implementations of filter constrained POCS however both do offer an advantage over POCS alone. The greatest improvement offered by the filter constraint algorithm is seen for SCA. The improvement is enough to make this a much more competitive algorithm even bringing it up to the level of the iterative approaches.

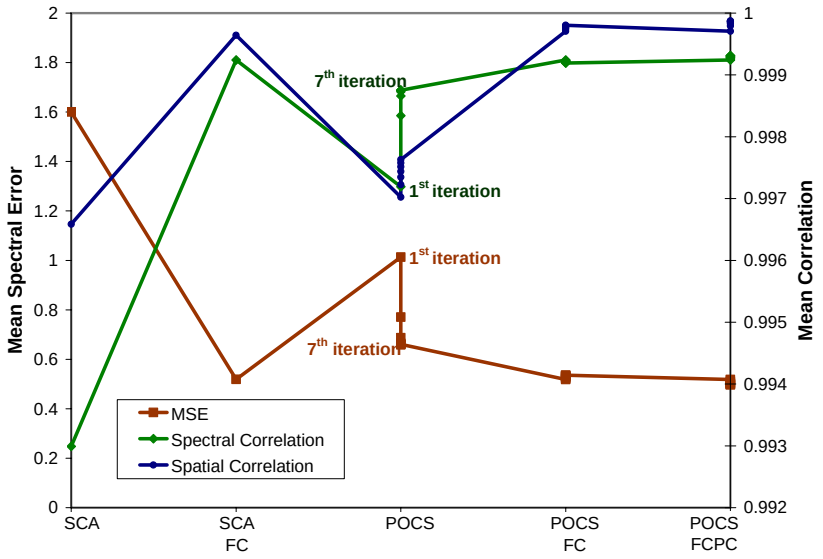

Figure 27. Mean spatial error, spectral correlation and spatial correlation as a function of reconstruction algorithm and iteration number for Cube 8.

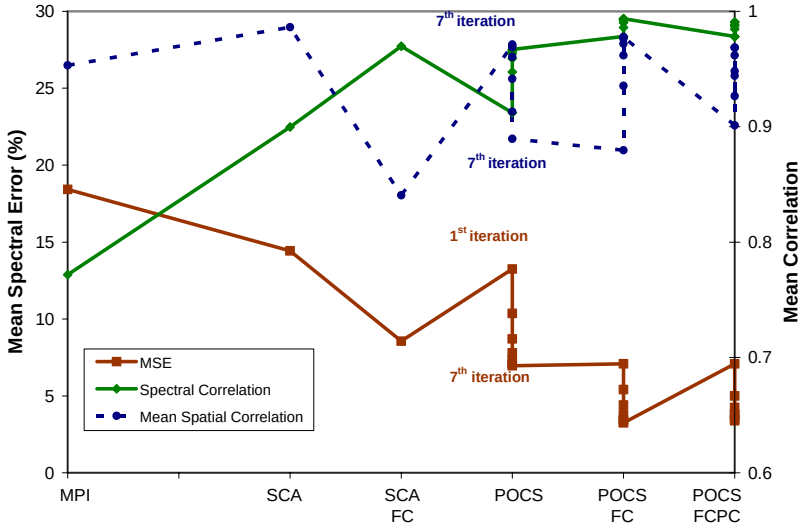

Figure 28. Mean spatial error, spectral correlation and spatial correlation as a function of reconstruction algorithm and iteration number for Cube C.

8. Task-based Measures of Reconstruction Quality

In the past, CTS reconstruction quality has been assessed in terms of spectral and spatial accuracy. While these are important parameters for assessing strict reconstruction accuracy, they do not hold the answers to questions most likely posed by end-users. Specifically, they do not include any information regarding how the data will be used or better yet whether or not the data is accurate enough to meet specific mission requirements. To this end, we looked at 2 possible mission scenarios. The first assumes a need to detect static point targets against a cluttered background. Static targets are used because it is assumed that the spectra associated with dynamic events can be calculated without need for full datacube reconstruction (e.g., for example using background subtraction methods). The second scenario involves the need to perform bulk classifications on all materials within the scene. This would correspond to fairly general classes such as vegetation, water and bare soil. We are interested in quantifying the difference between classifications maps derived from a standard hyperspectral instrument (no reconstruction required) versus those derived from the CTS system. The method of quantifying changes in bulk classification was developed as part of this LDRD effort and is described in 10. Theoretical Description of Classification Algorithms.

9. Reconstruction Accuracy of Anomalous Point Objects

As mentioned above we were interested in quantifying the ability of various reconstruction algorithms to accurately estimate anomalous spectra within a scene. We also sought to assess the dependence of these reconstructions on (1) the number of PCs used in reconstruction constraints, (2) the ratio of target to background signals, and (3) the correlation between the target and background signatures. For the point target experiments, the Synthetic Scene Generation Model (SSGM) was used to create both the basic scene and anomalous spectra.[8] The base scene without any anomalous spectra is shown in Figure 29.

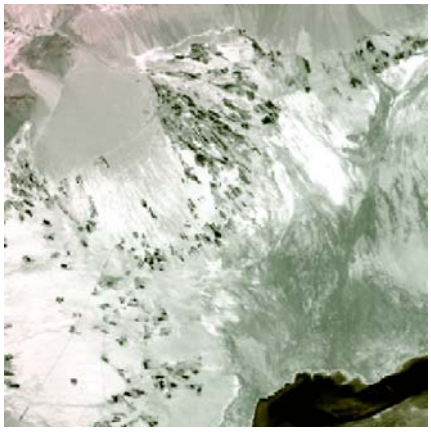

Figure 29. SSGM scene used in anomalous spectra experiments.

9.1 Target to Background Ratio

The first experiment was to assess the reconstruction accuracy of the point target (anomalous) spectra as a function of the ratio between the total target irradiance and the total background irradiance. Here, we considered only one anomalous spectrum. In order to compare the impacts of adding multiple dim targets versus a few bright targets, the point targets were inserted in numbers of 1, 10, 100 or 1000 were inserted at locations selected from a uniform random distribution of positions. The anomalous spectrum and the average background spectrum are shown in Figure 30a and Figure 30b, respectively. The correlation between these spectra is a moderate 0.65. The relationship between reconstruction accuracy for anomalous spectra with varying degrees of correlation to background is explored later in this report.

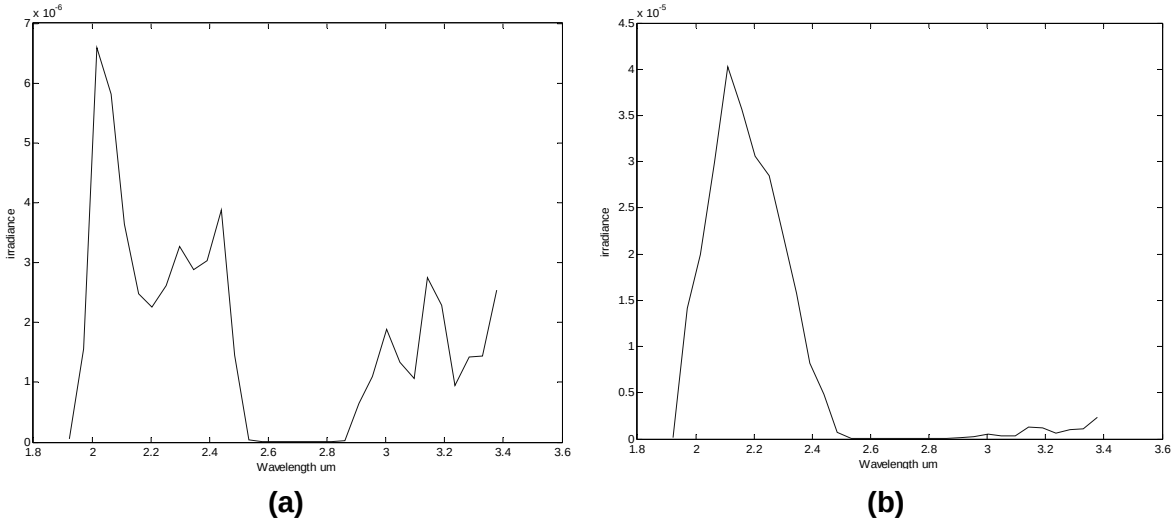

Figure 30. (a) Original target signal used for TBR experiment. (b)Average background signal from the SSGM scene.

The target to background ratio (TBR) is calculated as follows. Given the original simulated target spectrum (S_{ot}) the altered target spectrum $\left(S_{at} = \delta * S_{ot}\right)$ and the average background spectrum $\left\langle S_b \right\rangle$, the TBR is defined as

$$TBR = \frac{\sum_i \left(S_{at}\right)_i}{\sum_i \left\langle S_b \right\rangle_i} \text{ where } i = 1\ldots \text{ to the number of bands.} \qquad (14)$$

Targets are placed in the scene by full pixel replacement at the given location(s) with TBRs ranging from 0.1 to 3 in increments of 0.1. The family of curves for these TBR values is shown in Figure 31. After the point targets were inserted in the basic scene, a set of projection images and subsequently reconstruction estimates were generated using the algorithms of the Sections entitled "CTS Imaging Model and "Object Cube

Reconstructions", respectively. The algorithms are referenced as Moore-Penrose Pseudo-Inverse (MPI), Projection onto Convex Sets (POCS), Projection onto Convex Sets with Filter Constraints (POCS Filter), Projection onto Convex Sets with Filter Constraints per iteration (POCS PC), Subspace Constraint Algorithm (SCA) and Subspace Constraint Algorithm with Filter Constraints (SCA Filter).

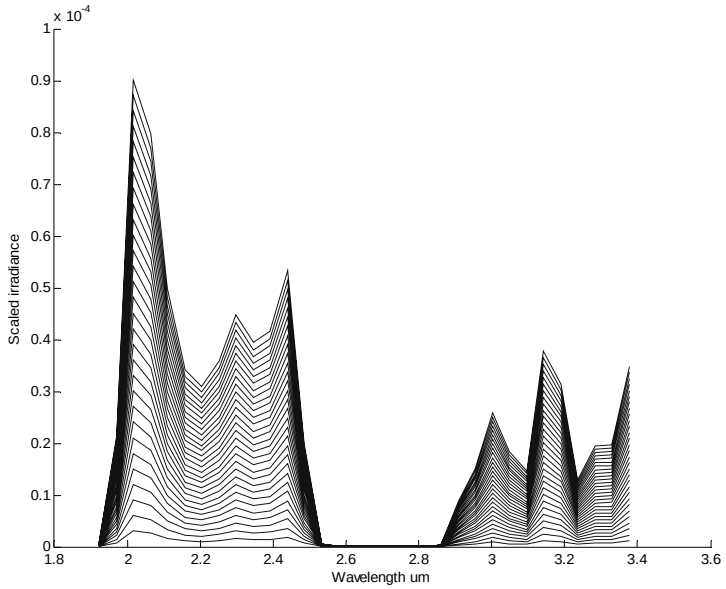

Figure 31. Family of curves for the 30 TBR levels.

After each reconstruction the target spectra were extracted and compared to their original signature using the spectral angle defined as

$$\alpha = \arccos\left(\frac{\sum_{i=1}^{n} \left(S_{at}\right)_i \cdot \left(S_{rt}\right)_i}{\sqrt{\sum_{i=1}^{n} \left(S_{at}^2\right)_i} \cdot \sqrt{\sum_{i=1}^{n} \left(S_{rt}^2\right)_i}} \right). \qquad \textbf{(15)}$$

In Equation (15), n is the number of bands and S_{rt} is the reconstructed spectrum. For algorithms which use PC based constraints, the number of PCs was varied from 3 to 6 and the resulting spectral angle was averaged over the 4 results. The quality of individual reconstructions is highly dependent upon several variable parameters within the reconstruction algorithms. In order to explore the dependency of reconstructions on the selection of PCs, we looked at the residual errors associated with a range of PC transformations. We did this in such a way as to isolate these errors were from other reconstruction artifacts. Specifically, we examined the errors incurred by expanding the target and background spectra in terms of a limited set of PCs (ranging from 3 to 6). These PCs were calculated first from the region outside the missing cone and then from the entire datacube. This process was repeated for each target-scene combination.

9.2 Spectral Correlation to Background

In order to study the effects of target to background correlation on reconstruction accuracy of anomalous spectra, a second experiment was created. The TBR was kept at a constant value of 2 while adding varying amounts of the average background spectrum to the target spectrum. A TBR of 2 was chosen to assure that the target signature dominated for each anomalous pixel. The altered target spectra is defined as

$$S_{at} = \varepsilon \cdot (\alpha \cdot \langle S_b \rangle + S_{ot}) \tag{16}$$

The variable, ε is used to maintain a constant TBR and is defined as,

$$\varepsilon = \frac{TBR \cdot \sum_i \langle S_b \rangle_i}{\sum_i \alpha \cdot \langle S_b \rangle_i + S_{oti}} \tag{17}$$

while α is used to vary the target to background spectral correlation and is defined as,

$$\alpha = \frac{2\sum_i (S_{ot})_i}{\sum_i \langle S_b \rangle_i} \text{ where i = 1, … Number of spectral bands.} \tag{18}$$

A family of 10 curves was created that have target to average background correlations of 0.0002, 0.1, 0.2, 0.3, 0.4, 0.5, 0.6, 0.7, 0.8, and 0.9. The curves are shown in Figure 32.

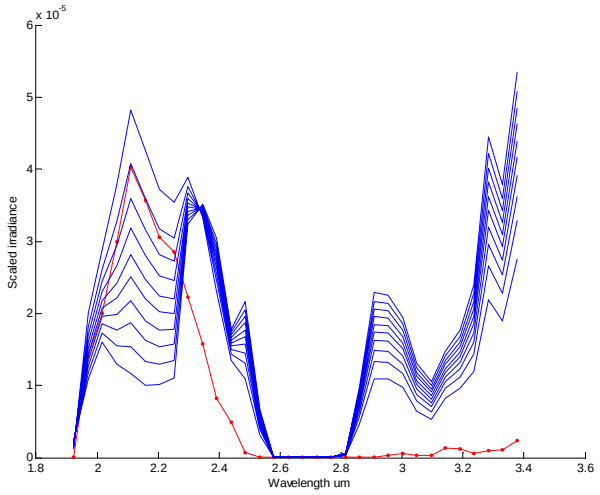

Figure 32. Family of curves used in the correlation experiment, solid blue lines correspond to target curves; while, the solid red line corresponds to the average background spectrum.

9.3 Target to Background Ratio Results

As described above, two experiments were devised and conducted to evaluate the ability of various CTS reconstruction algorithms to reconstruct point target and background scene spectra. In addition, an attempt was made to quantify the degradation in reconstruction quality associated with representing the target and background spectra by a limited subset of PCs calculated from a limited subset of spatial frequencies. The quality metric used in all cases was the spectral angle between the reconstructed and original spectrum. For the TBR experiment 1, 10, 100 or 1000 targets were inserted into the SSGM scene. A subset of the plots for each of the six sets is shown for the 1000 target case in this section. See Appendix B for a complete set of plots associated with the TBR, correlation and principal component experiments.

9.3.1 PC impacts as a function of TBR

In general a smaller spectral angle is calculated when using principal components calculated from outside rather than inside the missing cone (e.g., See Figure 33). As the target radiance is increased relative to the background, the spectral angle decreases for both cases. An interesting phenomenon occurs when only 1 target is present. Specifically, there is a dip in the spectral angle when using PCs calculated from outside of the missing cone at a TBR of approximately 0.5 after which the curve increases. At this time, there is no explanation for this behavior. See Figures B1, B11, B23 and B35 in Appendix B for the complete set of curves associated with this experiment.

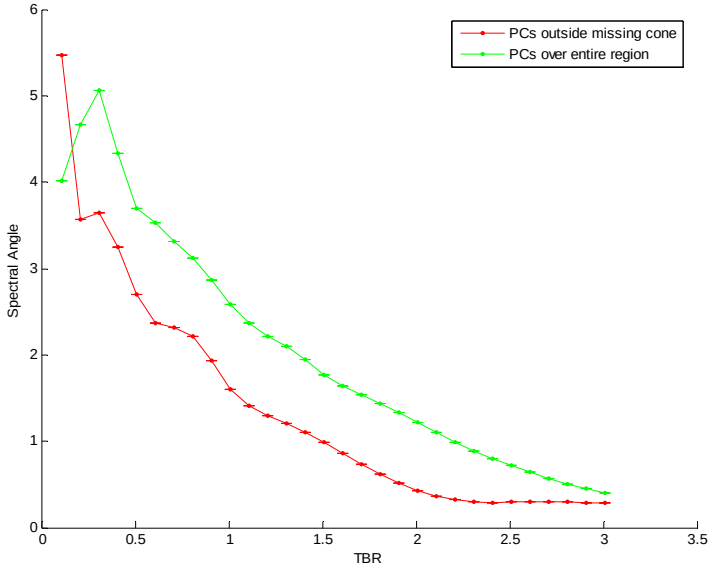

Figure 33. Average and standard deviation of spectral angle versus TBR for target signature(s) using projections onto principal components in the spatial frequency domain calculated outside missing cone and over entire region. The average of the spectral angles associated with 3 to 6 PCs are shown here.

In contrast to the target signatures, the average background is better represented when all spatial frequencies are included in the principal components calculations. Due to the punctile nature of the targets, we expect these objects to be better represented at the higher spatial frequencies outside the missing cone than the background materials which are dominated by lower spatial frequencies. Overall the average spectral angles are very small (< 2 degrees) while the standard deviation increases as the target pixel(s) become brighter. A representative plot is shown in Figure 34 for an insertion of 1000 randomly placed targets. See Figures B4, B14, B26, and B38 in Appendix B for the complete set of curves associated with this experiment.

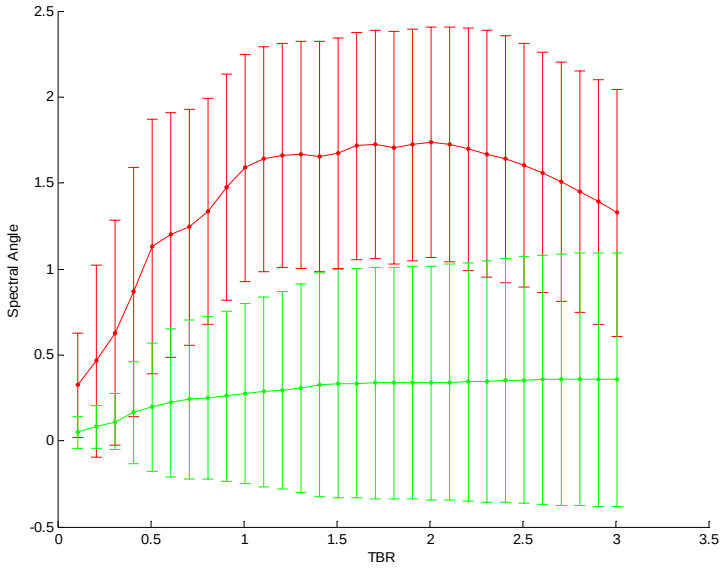

Figure 34. Average and standard deviation of spectral angle versus TBR for the background signatures using projections onto principal components in the spatial frequency domain calculated outside missing cone and over entire region. The average of the spectral angles associated with 3 to 6 PCs are shown here.

9.3.2 MPI Results as a function of TBR

In general, as the TBR increases, the spectral angle decreases for all target insertion numbers and their values are nearly identical; however, if only 1 target is inserted, the spectral angle is on average 15 degrees below the other curves. Considering that one target pixel could be represented as a delta function, its Fourier transform would be a constant, therefore represented at all frequencies. MPI exploits the data contained outside of the missing cone using the system transfer function and the single target is well represented in this case leading to a smaller spectral angle. A representative plot is shown

in Figure 35 for an insertion of 1000 randomly placed targets. See Figures B2, B12, B24, and B36 in Appendix B for the complete set of curves associated with this experiment.

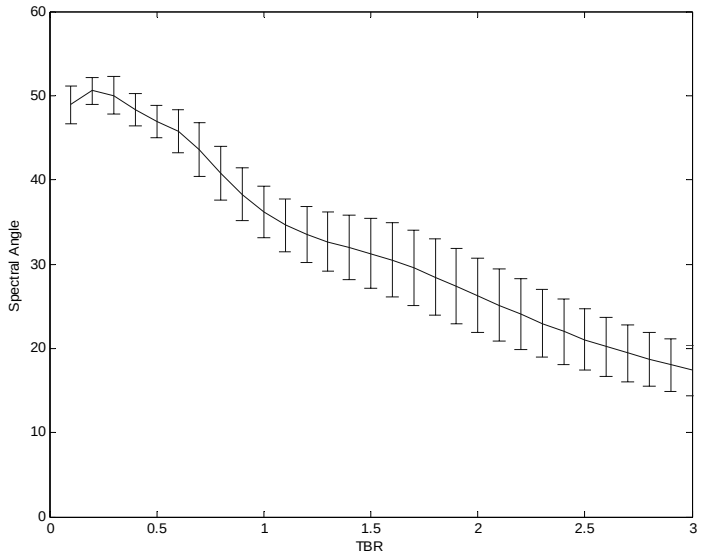

Figure 35. Average and standard deviation of spectral angle versus TBR for target signature(s) reconstructed with the MPI algorithm.

For MPI reconstructions of the background signatures, the spectral angle remains relatively constant irregardless of the number of targets inserted or the brightness of those targets. This shows that the accuracy of the reconstructed background spectra are largely unaffected by the insertion of anomalous spectra when using the MPI reconstruction algorithm. A representative plot is shown in Figure 36 for an insertion of 1000 randomly placed targets. See Figures B5, B15, B27, and B39 in Appendix B for the complete set of curves associated with this experiment.

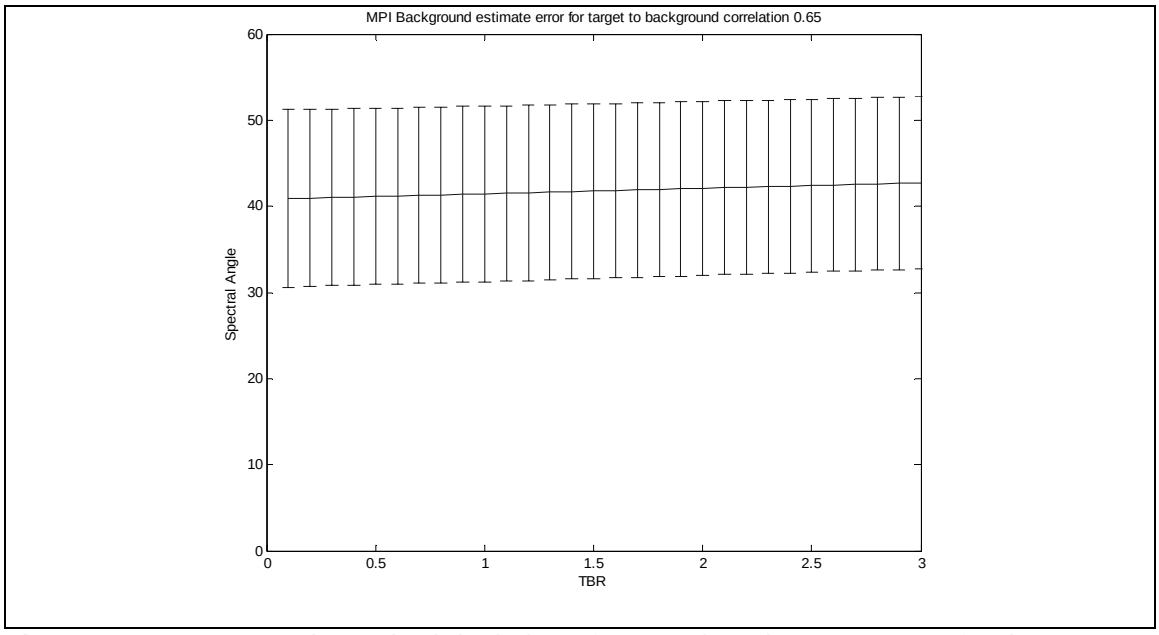

Figure 36. Average and standard deviation of spectral angle versus TBR for the background signatures reconstructed with the MPI algorithm.

9.3.3 TBR SCA and POCS Results (Filter and non-Filter constrained)

In general the POCS, POCS Filter and SCA Filter have smaller spectral angles than SCA and POCS PC. The POCS algorithm is considerably better for the 1 target case. An unexplained hump appears in the POCS PC curve for all cases. The POCS, POCS Filter and SCA Filter curves show that a bright target (TBR of 1.5 or greater) will be resolved with a spectral angle of 15 to 10 or better for all cases. A spectral angle of 15 degrees or better will generally provide acceptable target identification; however this depends on the correlation to the background spectra. A representative plot is shown in Figure 37 for an insertion of 1000 randomly placed targets. See Figures B3, B13, B25, and B37 in Appendix B for the complete set of curves associated with this experiment.

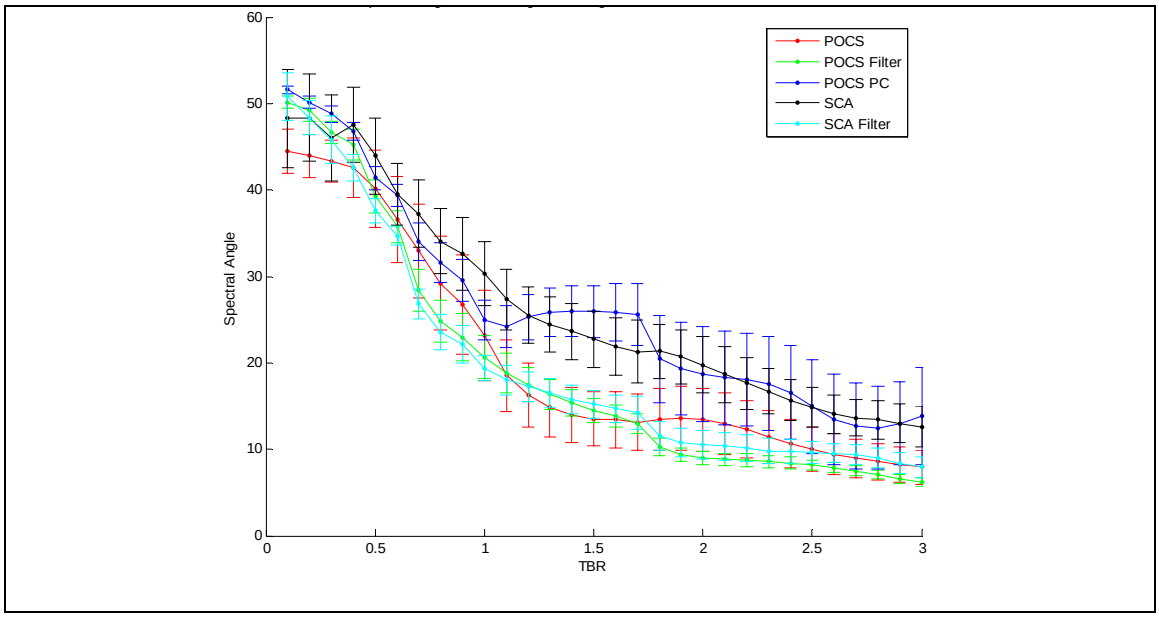

Figure 37. Average and standard deviation of spectral angle versus TBR for target signature(s) reconstructed with POCS, POCS Filter, POCS PC, SCA, and SCA Filter algorithms.

For reconstructed background spectra, the spectral angle statistics are relatively constant for all but the POCS PC algorithm, which is not understood at this time. Once again the POCS, POCS Filter and SCA Filter are consistently the best performers. Overall the POCS algorithm seems to have the smallest angles. A representative plot is shown in Figure 38. For an insertion of 1000 randomly placed targets. See Figures B6, B16, B28, and B40 in Appendix B for the complete set of curves associated with this experiment.

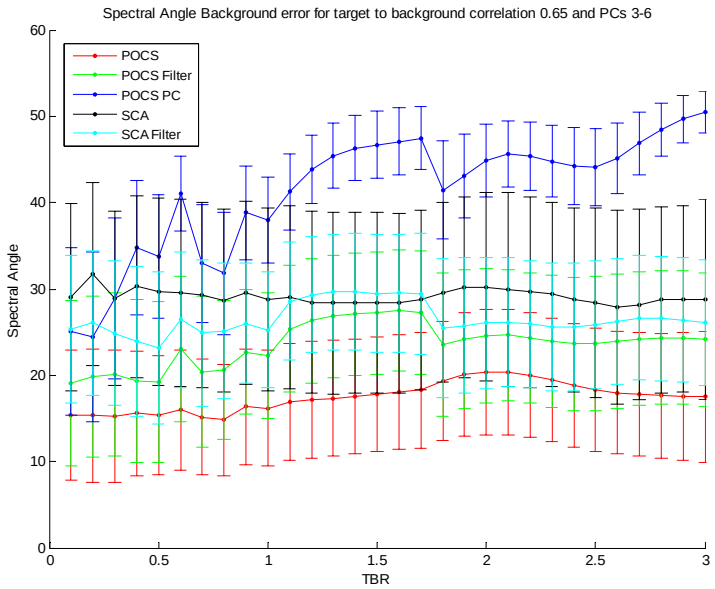

Figure 38. Average and standard deviation of spectral angle versus TBR for the background signatures reconstructed with POCS, POCS Filter, POCS PC, SCA, and SCA Filter algorithms.

9.4 Spectral Correlation to Background

9.4.1 PC impacts as a function of Spectral Correlation

For the spectral correlation experiment 1, 10, 100 or 1000 targets were inserted into the SSGM scene. Again we are first interested in how well we can represent the target spectra from principal components calculated from all spatial frequencies as well as just those outside the missing cone. For all numbers of inserted targets, the spectral angle decreases as the target to background correlation approaches 1. Intuitively, as the similarity between the target and background increases, the target should be better represented by principal components which are calculated primarily from background statistics. Overall the principal components calculated outside of the missing cone resulted in smaller spectral angles. This is again explained by their relatively higher contribution to higher spatial frequencies than the background signal. The single target case has spectral angle twice as large as the other cases, however this is not understood at this time. A representative plot is shown in Figure 39 for an insertion of 1000 randomly placed targets. See Figures B7, B17, B29 & B41 in Appendix Bfor the complete set of curves associated with this experiment

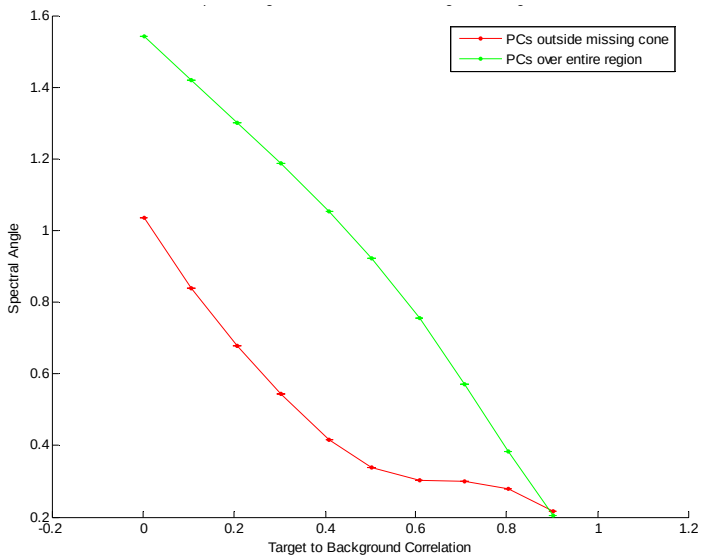

Figure 39. Average spectral angle versus target to background correlation for target signature(s) using projections onto principal components calculated from spatial frequencies outside missing cone and over entire region.

As was the case in the TBR experiments, the background spectra are estimated with smaller spectral angles when using PCs from the entire spatial frequency range. A representative plot is shown in Figure 40 for an insertion of 1000 randomly placed targets. See Figures B10, B20, B32 & B44 in Appendix B for the complete set of curves associated with this experiment.

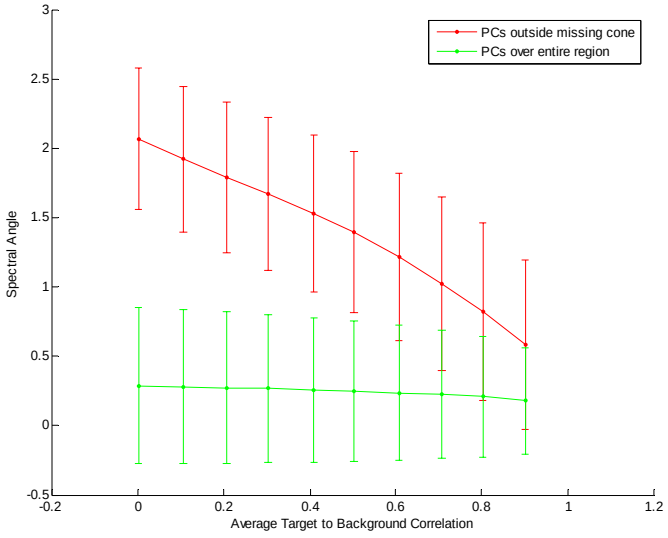

Figure 40. Average and standard deviation of spectral angle versus target to background correlation for the background signatures using projections onto principal components in the spatial frequency domain calculated outside missing cone and over entire region.

9.4.2 MPI Results as a function of Spectral Correlation

For target spectra reconstructed using MPI, the spectral angle generally increases as the target to background correlation increases. As the target spectra gain similarity to the surrounding background, one would expect the target spectra to have a reduced contribution to higher spatial frequencies (i.e., the target spectra begin to blend with the background) and therefore perform in this way. A representative plot is shown in Figure 41 for an insertion of 1000 randomly placed targets. See Figures B8, B18, B30, and B42 in Appendix B for the complete set of curves associated with this experiment.

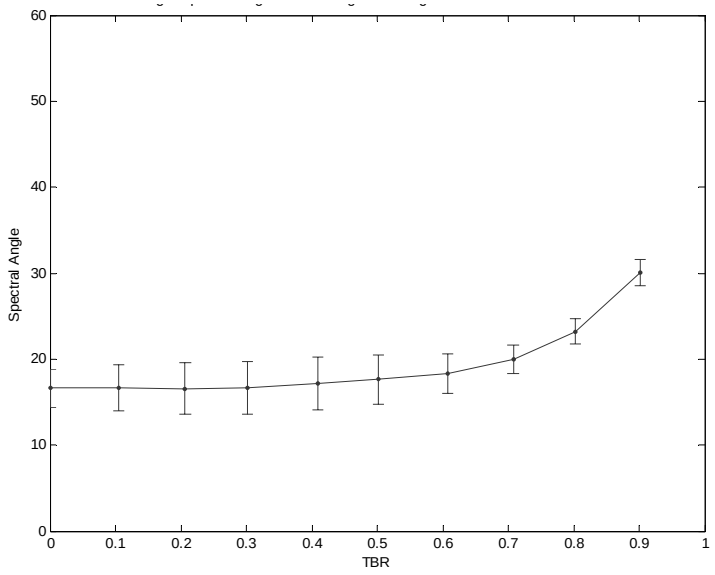

Figure 41. Average and standard deviation of spectral angle versus target to background correlation for target signature(s) reconstructed with the MPI algorithm.

For MPI reconstructions of the background signatures, the spectral angle remains relatively constant irregardless of the number of targets inserted or the target to background correlation. A representative plot is shown in Figure 42 for an insertion of 1000 randomly placed targets. See Figures B11, B21, B33, andB45 in Appendix B for the complete set of curves associated with this experiment.

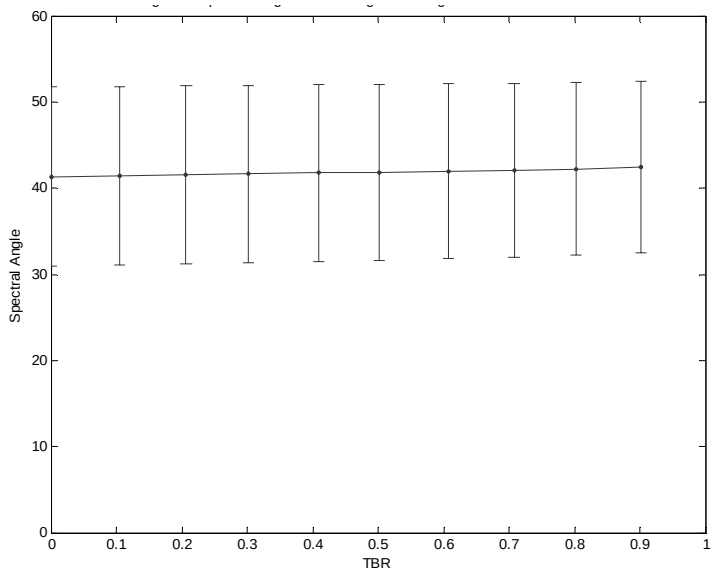

Figure 42. Average and standard deviation of spectral angle versus target to background correlation for the background signatures reconstructed with the MPI algorithm.

9.4.3 Spectral Correlation SCA and POCS Results

For reconstructed background spectra, SCA outperformed all other algorithms for all target number cases while POCS PC gave the highest angles overall. The POCS algorithm was the second best performer. The spectral angle increases as the correlation approaches 1 due to its decrease in spatial frequency and subsequent movement into the missing cone (i.e., towards lower spatial frequencies). A representative plot is shown in Figure 43 for an insertion of 1000 randomly placed targets. See Figures B9, B19, B31, and B43 in Appendix B for the complete set of curves associated with this experiment.

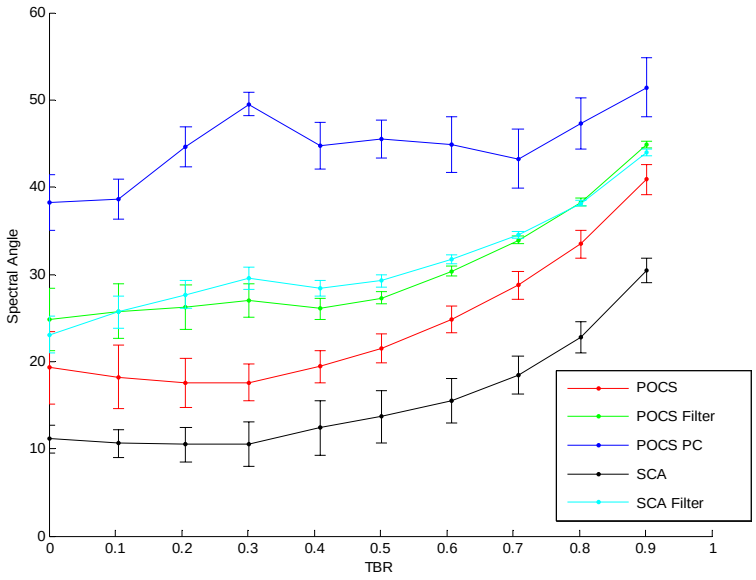

Figure 43. Average and standard deviation of spectral angle versus target to background correlation for target signature(s) reconstructed with POCS, POCS Filter, POCS PC, SCA, and SCA Filter algorithms.

In general, the inserted target spectra correlations have little effect on the background spectral reconstructions. The POCS algorithm has the smallest angles overall while POCS PC has the highest; however as the number of targets decreases POCS produces higher and higher spectral angles. A representative plot is shown in Figure 44 for an insertion of 1000 randomly placed targets. See Figures B12, B22, B34, and B46 in Appendix B for the complete set of curves associated with this experiment.

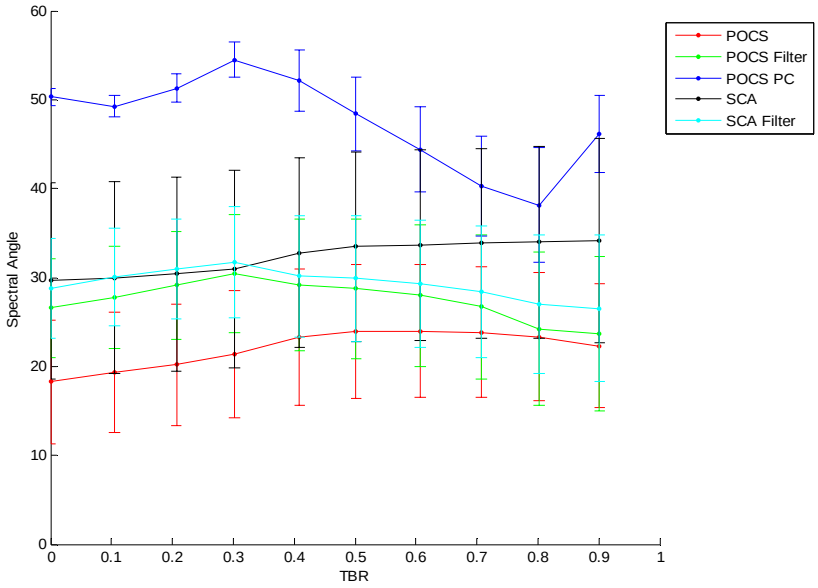

Figure 44. Average and standard deviation of spectral angle versus target to background correlation for the background signatures reconstructed with POCS, POCS Filter, POCS PC, SCA, and SCA Filter algorithms.

9.5 Point Target Conclusions

For all point target experiments, the POCS and POCS filter reconstructions produce the minimum spectral angles. The SCA algorithm, on the other hand performs poorly for the targets but very well for the background spectra. The CTS system is ideal for point target detection due to their inherent high spatial frequency that is well preserved outside of the missing cone. As was expected, the system performs better when the targets are bright relative to the background and are less correlated to the background. The single target case needs to be investigated further to better explain its behavior in terms of TBR and correlation.

10. Theoretical Description of Classification Algorithms

10.1 Introduction

Image classification is proposed in this LDRD as the means of characterizing the "bulk" loss/change in information due to image reconstructions. The basic assumption is that the classification of a near-perfect CTS image reconstruction should provide a nearly identical match with that of the classification of the original image from which the CTS reconstruction was derived. As such, the match between the CTS and original image classifications should diminish with poorer reconstructions or with the introduction of increasing amounts of system noise or CTS instrument jitter. The challenges in this study include both the choice of image classification and development of a means to compare classification maps. In the last 30 to 40 years several image classification algorithms have been developed for multispectral/hyperspectral imagery and are readily available for this study. However, all are not equally applicable or useful to this problem. Our study concentrates on examining the results from two suitable yet very different classification approaches. In contrast, the concept of quantifying a match between classification maps has received comparatively little or no study. We propose one approach for quantifying the "optimum" match between classification maps. The results provided are based on an approximation which requires significantly less time to compute.

10.2 Classification Approaches

Classification approaches can typically be categorized into parametric and nonparametric methodologies. Some commonly used parametric approaches rely on Gaussian mixture models to characterize the feature space clusters.[9,10,11] These sorts of approaches also require the number of clusters/classes as input in order to iteratively establish the appropriate mixture of parameterized distributions. Some approaches for determining this number are discussed in [12].[12] In general, parametric methods yield unsatisfactory results especially where a complex feature space is involved. Since the shape of the delineated clusters is predefined with a parametric model, defining the feature space distribution in this way will tend to introduce artifacts in the resulting classified image.

Nonparametric clustering methods do not rely on a priori assumptions about the feature space distribution. These methods are better suited for complex feature spaces and tend to provide superior results in these cases. Nonparametric approaches can be categorized into hierarchical and density estimation methods. Hierarchical methods combine (or partition) data based on a given proximity measure.[13] These methods tend to be computationally expensive and the stopping criteria for combining (or partitioning) the data are not clear-cut. Alternately, nonparametric methods, based on density estimation, leverage off the concept that the feature space can be viewed as an empirical multivariate distribution. Dense regions in this feature space correspond to the modes of the empirical distribution. Given the location of a particular mode, the associated cluster can be delineated based on the distribution within the local feature space.

Recently more powerful nonparametric cluster approaches have been introduced.[14] With these, the goal has been to determine modes of the underlying probability density to define candidate cluster centers. Although very powerful, this approach can fall victim to another common data and dimensionality problem known as the 'curse of dimensionality'. That is, the density estimation will tend to become more difficult as the dimensionality of the feature space increases. In particular, when the dimensionality N becomes very large (e.g. $N > 7$) in a multidimensional feature space, samples quickly become 'lost' in the wealth of the space. Moreover, local neighborhoods of points in a high dimensional space are likely to be free of observations. When neighborhoods are extended to include a sufficient number of observations, they become so large that they tend to provide global, rather than local density estimates. To relieve the problem by filling the space with observations would soon require prohibitively large sample sizes.

The two approaches chosen for this study include a selection from each of these categories. The parametric approach is the well-known *k*-means clustering approach that has been used extensively in image analysis.[15] The other is a relatively new non-parametric approach known as Distribution-Free Clustering (DFC).[16] We believe that DFC should provide classification maps that are more consistent with the self similar regions represented by each image. Although *k*-means is a very different classification approach, we choose it for this study to cross-check reconstruction quality trends determined from DFC.

10.2.1 K-means Clustering

K-means is a non-hierarchical approach for partitioning (or clustering) N data points into K disjoint subsets S_j containing N_j data points so as to minimize the sum-of-squares criterion (19). Here x_n is a vector representing the nth data point and μ_j is the geometric centroid of the data points in S_j.

$$J = \sum_{j=1}^{K} \sum_{n \in S_j} \left| x_n - \mu_j \right|^2 \tag{19}$$

When the user specifies a random start, the algorithm generates the *k* cluster centers randomly and proceeds by fitting the data points in those clusters. The algorithm assigns each case (object) to one of *k* clusters so as to minimize a measure of dispersion within the clusters. The algorithm consists of a simple re-estimation procedure as follows. First, the data points are assigned at random to the K sets. Then the centroid is computed for each set. These two steps are alternated until a stopping criterion is met, i.e., when there is no further change in the assignment of the data points

This very common measure of sum of distances or sum of squared Euclidean distances from the mean of each cluster can be set up as an integer programming problem but because solving integer programs with a large number of variables is time consuming,

clusters are often computed using a fast, heuristic method that generally produces good (but not necessarily optimal) solutions.

In general, the algorithm does not achieve a global minimum of *J* over the assignments. In fact, since the algorithm uses discrete assignment rather than a set of continuous parameters, the "minimum" it reaches cannot even be properly called a local minimum. Despite these limitations, the algorithm is used fairly frequently as a result of its ease of implementation.

10.2.2 Distribution-Free Clustering

The goal of DFC is to perform unsupervised coarse level image classification consistent over image calibration or sensor view geometry. We propose that a gross spectral shape can be exploited. The proposed approach associates spectra that have similar overall shape characteristics to designate self-similar regions while ignoring the categories of spectral variabilities mentioned here. This algorithm is significantly more intricate than *k*-means. The description of the algorithm follows below.

In the first step the image is transformed into a space where signal variabilities within self-similar regions are less discernable. The approach applied is a scaling-independent transformation that reduces the pixel-to-pixel variability and enables our multivariate clustering approach. The spectral content represented in a given *N*-dimensional pixel can be viewed as the 'spectral-signature' for any underlying material(s) as seen by the sensor. Our transformation is a simple rank ordering of the *N* components of this signature.

Due to the ran*k*-ordering approach used to quantize the spectral signatures, the transformed data becomes concentrated in a predetermined number of feature space locations. That is, the rank ordering quantization process forces the spectral signatures (feature vectors) to take on $N!$ predetermined values. For example, for $N = 3$, we have $3!$ or 6 possible permutations. The resulting 6 quantized feature vectors (QFVs) V_i are as follows: $[0,1,2]$, $[0,2,1]$, $[1,0,2]$, $[1,2,0]$, $[2,0,1]$, and $[2,1,0]$.

Given any two QFVs $V_m = [v_{ma}, v_{mb}, ...]$ and $V_k = [v_{ka}, v_{kb}, ...]$, we define the squared spectral distance (SSD) between these as shown in (20). From here on, we refer to the SSD as simply the "distance". It can be shown that the minimum distance between any two vectors in this quantized space is independent of *N* and cannot be less than 2. However, the maximum distance $d_{\max}$ varies as function of *N*. Thus, given this prepossessing step, the QFVs are integer valued and are limited to the permutations on *N*. It is important to note that only a subset of the $N!$ possible permutations can be represented in typical imagery. For example, in 14-band image there are approximately 87 billion possible permutations. However, the actual number of represented permutations cannot exceed the number of actual pixels.

$$d = \|V_m - V_k\|^2 = (v_{ma} - v_{ka})^2 + (v_{ka} - v_{kb})^2 + \ldots \quad \textbf{(20)}$$

10.2.3 Graph Theoretic Framework

The data quantization described earlier is the basis of our framework in which coarse level image classification can be performed. In particular, data in our quantized feature space can be viewed as a graph consisting of a set of nodes $\mathbf{V}$ (also referred to as vertices) and a set of connecting edges $\mathbf{E}$. In this framework, each node $\mathbf{V}_i \in \mathbf{V}$ corresponds to one and only one of the $N!$ QFVs and $\mathbf{E}_{i,j} \in \mathbf{E}$ corresponds to the connecting edge between two of the nodes in $\mathbf{V}$. The node symbol $\mathbf{V_i}$ is represented in bold here in order to distinguish it from the corresponding QFV, $\mathbf{V_i}$. Together, the sets of nodes and connecting edges describe our basic graph, $\mathbf{G} = (\mathbf{V}, \mathbf{E})$. Thus, each of the possible $N!$ nodes $\boldsymbol{v_i}$ represents a particular number of quantized spectral signatures.

The edges $\mathbf{E}_{i,j}$ between nodes in the graph represent similarity relationships between QFVs. Two nodes are related and therefore connected by an edge if their distance is less than or equal to a connectivity distance $d_{connect}$ where $2 \le d_{connect} \le d_{\max}$. We note that multiple connections can occur between nodes for a given $d_{connect}$. This can be illustrated with the representative feature vectors $[0,1,2]$, $[0,2,1]$, and $[1,0,2]$. For $d_{connect} = 2$, the nodes represented by the vector pair $\{[0,1,2],[0,2,1]\}$ are connected, as is the node pair $\{[0,1,2],[1,0,2]\}$. The basic graph shown in Figure 45 (a) illustrates the connectivity for all possible nodes for the $N = 3$ case, and $d_{connect} = 2$. Here, the nodes are depicted as circles with labels $\mathbf{V}_i$ and the associated QFV shown in the node.

From the case represented by Figure 45 (a), we observe that a single graph contains all possible representative nodes. We note that in some cases, one or more QFVs may not be represented within the data and thus the corresponding nodes will not be part of the graph. For example, if we find that the QFVs corresponding to nodes $\mathbf{V}_2$ and $\mathbf{V}_3$ do not exist, then the graph describing our feature space will consist of two unconnected sub-graphs as shown in Figure 45(b). From Figure 45 (a), we also observe two characteristics: 1) multiple connections to nodes and 2) the existence of a path from any given node to any other node. Although our observations of this graphical feature space description provide us some insights into the relationships between QFVs, it is not immediately apparent how this can assist us in classifying an image. However, through the introduction of two additional constraints (*Node Weight and Connectivity Direction*) to our basic graph framework this problem becomes more tractable as we will show in the next section.

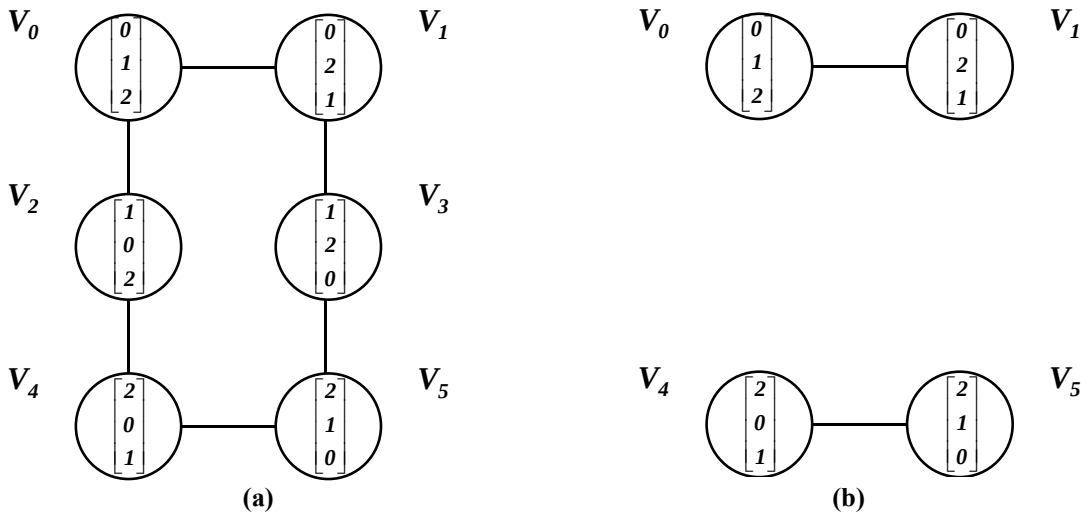

Figure 45 (a) Graph for *N*=3 and $d_{connect}$ = 2, **(b)** Unconnected graphs for *N*=3 and $d_{connect}$ = 2

Node Weight is defined as the total number of original feature vectors (spectra) transformed to a QVF representative and *Connectivity Direction* is the direction designated from the node with the larger weight (parent) *to* the node with the smaller weight (child). Edge weights between nodes are equal to the weight of the parent node. We define a weight function $\mathbf{w}$ for edge $\mathbf{E}_{i,j}$ as $\mathbf{w}(\mathbf{V_i}, \mathbf{V_j}) = \mathbf{w}(\mathbf{V_i})$, where $E_{i,j}$ indicates directionality from i to j and $\mathbf{E}_{j,i}$ indicates directionality from j to i. Figure 46 illustrates this concept for the following node weight relationships: $\mathbf{w}(\mathbf{V_1}) > \mathbf{w}(\mathbf{V_0})$, $\mathbf{w}(\mathbf{V_1}) > \mathbf{w}(\mathbf{V_3})$, $\mathbf{w}(\mathbf{V_0}) > \mathbf{w}(\mathbf{V_2})$, $\mathbf{w}(\mathbf{V_2}) > \mathbf{w}(\mathbf{V_4})$, $\mathbf{w}(\mathbf{V_4}) > \mathbf{w}(\mathbf{V_5})$, and $\mathbf{w}(\mathbf{V_3}) > \mathbf{w}(\mathbf{V_5})$.

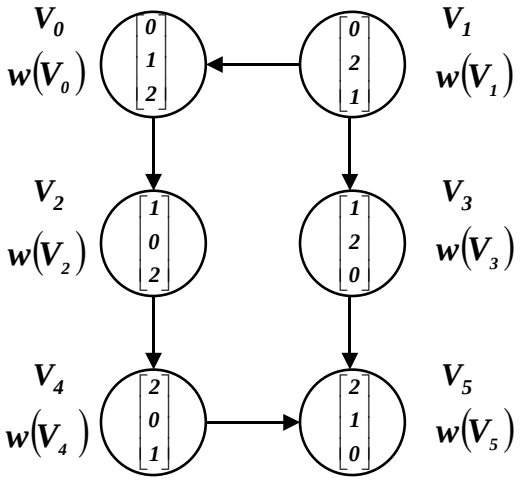

Figure 46 Graph for *N*=3 and $d_{connect}$ = 2 annotated with node weight and direction

In this modified framework, our feature space is represented by a directed acyclic graph (DAG). Certain important phenomena now become evident in this framework. In particular, certain nodes are found to have no incoming edges. These nodes are defined as "major nodes". In the sections that follow we will see that they tend to represent the most significant feature vectors in our image. Examples of these are nodes $\mathbf{V_1}$ and $\mathbf{V_2}$ in Figure 46(c). Equally important, we observe that multiple parent connections can occur to a child node.

Using the DAG framework, we suggest that self-similar regions in an image correspond to sub-graphs within the DAG. Our task becomes one of determining how to partition these sub-graphs such that each best represents a single classification within the data. The premise of our approach is that a child node can have one and only one parent. Thus, given a child node shared by multiple parent nodes, we must devise a scheme for choosing a single parent. Our goal in the next section is to explain a partitioning scheme that will give ownership of shared child nodes to the self-similar region within our feature space.

10.2.4 Graph Traversal Approach

In the framework described above, we introduce a graph traversal approach that seeks to partition our DAG into separate sub-graphs where each is rooted at a major node. In this approach, we establish parent-to-child ownership by seeking the path with *maximum* combined edge weight to any given child node. Doing so creates separate graphs known as maximum spanning trees. A great deal of research has been on the subject of *minimum* spanning trees, which typically use a "greedy" graph traversal approach that is based on the paradigm that a locally optimal choice will lead to a globally optimal solution to the problem. Dijkstra's algorithm* is one such method for finding *minimum* spanning trees in a DAG.[17] However this approach is not applicable to our task since finding maximized node paths require global knowledge of the graph and we must resort to a less optimized method described as follows:
First, we assume that a path $\mathbf{p_k} = \{\mathbf{V_0}, \mathbf{V_1}, ..., \mathbf{V_k}\}$ exists in $\mathbf{G}$ with a path weight $\mathbf{w(p_k)} = \sum_{\mathbf{i=1}}^{\mathbf{k}} \mathbf{w(V_{i-1}, V_i)}$ defined as the sum of the edge weights between successive pairs of nodes along the path $\boldsymbol{p_k}$. Based on our earlier edge weight definition, this can be simplified to $\mathbf{w(p_k)} = \sum_{\mathbf{i=0}}^{\mathbf{k}} \mathbf{w(V_i)}$. Further, we define $\mathbf{S}$ as a set containing nodes whose paths have already been determined to be maximized and we define $\mathbf{Q}$ as a set of nodes whose maximum paths have not been determined such that $\mathbf{Q} = \mathbf{V}\text{-}\mathbf{S}$. Next, for each node $\mathbf{V_q} \in \mathbf{Q}$, we keep only the edge to the predecessor parent with the maximum path

* Dijkstra's algorithm is a greedy approach used to efficiently generate a minimum-spanning tree for a directed acyclic graph from a single source node.

weight, and add $\mathbf{V_q}$ to $\mathbf{S}$. If the node $\mathbf{V_q}$ has only one parent, then it is immediately added to the set **S**. Maximum paths are determined by solving for every possible path from $\mathbf{V_q}$ to a major node. Recursion adds efficiency to this path calculation by working backwards from possible major nodes and only keeping track of path weight and immediate predecessor information. Once the algorithm has terminated and the set $\mathbf{Q}$ is empty then the set **S** contains all nodes in **V** and each of these nodes has only one parent.

Figure 47 shows an example of a DAG before traversal with node specifications and node weights shown outside the circles symbolizing the nodes along with the QFV specifications inside the circles. Figure 48 shows the same DAG after traversal with finalized edges. At this point we've established 3 separate clusters denoted by the 3 separate maximum spanning trees. Thus, each QFV has been included in a distinct cluster with one major node and is linked to other QFVs by similarity distance $d_{connect}$ via a maximally weighted path. We note that the use of path weights lends a sense of cluster gravity to our determined memberships.

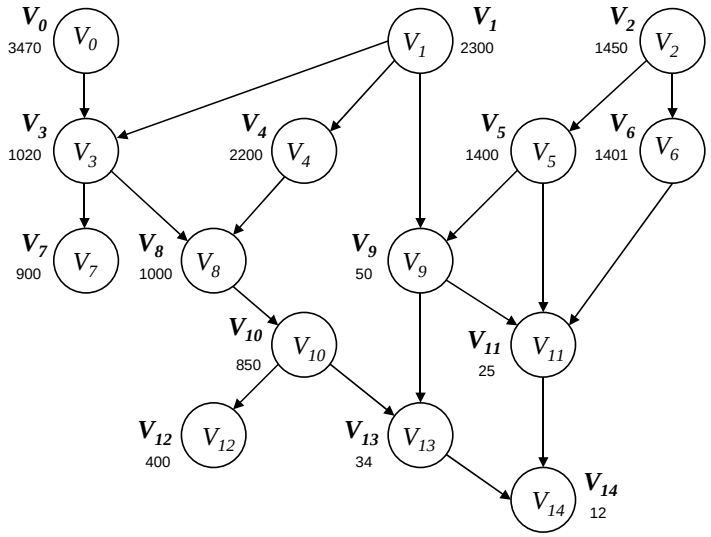

Figure 47 Example Directed Acyclic Graph before graph traversal annotated with node weight and direction.

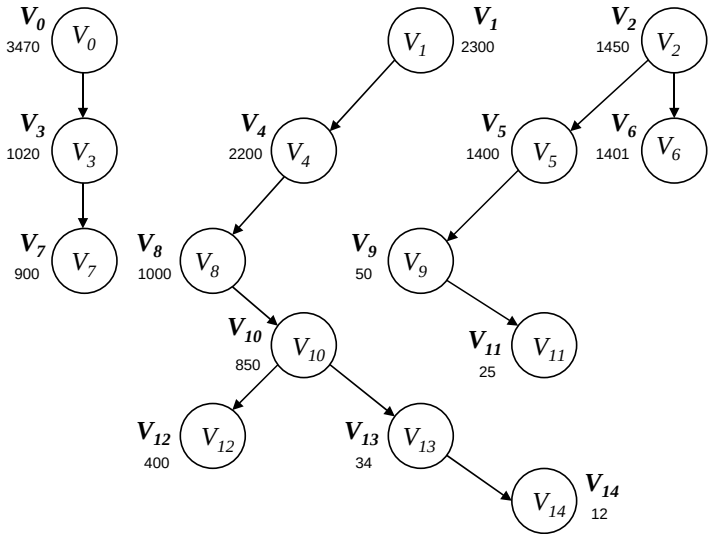

Figure 48 Example Directed Acyclic Graph after graph traversal annotated with node weight and direction.

10.3 Definition of Quality Metrics

The quality of a given reconstruction method is determined by comparing a classification map of a reconstructed image with one of the original image from which the reconstruction was derived. Here, the *k*-means and DFC classification algorithms are the methods we chose to generate these maps. We note that the classification algorithms proposed do not perform a classification as in terrain categorization or materials identification. Instead they simply associate self-similar regions based on their inherent design assumptions as described above. The resulting classes are each labeled with a unique numerical identifier by the algorithm

We note that the *k*-means algorithm will (in general) provide *k* uniquely labels regions for a user-specified value of *k*. In contrast the DFC algorithm, will determine the unique self-similar classes which may differ in number between the original and reconstructed image. Of course, if a reconstruction was "perfect" the number of classes will be the same but the numbering may or may not be the same. In the *k*-means based analysis, the same number of classes will be specified from both original and reconstructed images. We note that *k*-means also doesn't guarantee the same numerical labeling whether or not it is the same or a different image.

Given the possibility of varying class labeling or variations in the number of classes between original and reconstructed images, we propose a measure of quality that is independent of either. The quality measure that we define here is simply a measure of similarity between the original and reconstructed classification maps. We illustrate it with the aid of the following simple examples. The first and second examples illustrate cases where original and reconstructed classification maps both have the same number of classes as might be produced by *k*-means. The third illustrates a result where the number of reconstructed image classes is greater than original image classes.

The first example illustrated by Figure 49 depicts nearly identical classification maps between original and reconstructed datacubes. The data of concern is that which is contained inside the circular region. The area outside this circle is regarded as "masked". Here, the C1|C2 and C3|C4 boundaries have changed between the reconstructed and original image classifications.

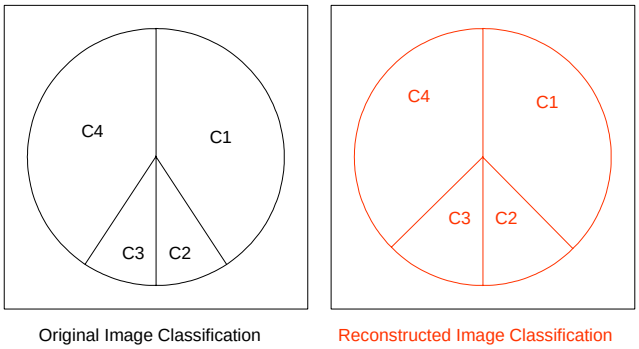

Figure 49. Classification maps for original and a nearly identical reconstruction

An overlay of the reconstructed classification map over the original image classification map as seen in Figure 50 illustrates how we might visualize their similarity. From this, we can discern how the classes of reconstructed and original overlap.

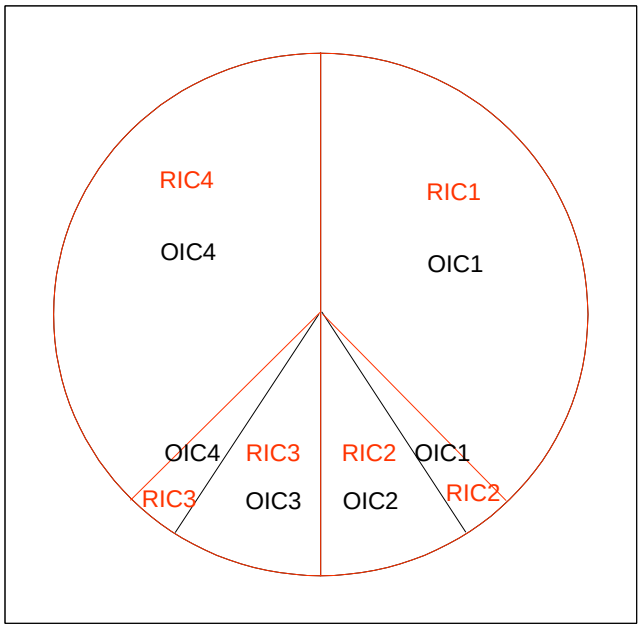

Figure 50. Overlapped class maps for nearly identical original and reconstructed images.

Equivalently, we can express these overlaps as a "Match" table. Here, the table indicates /the number of common pixels in classes that overlap between original and reconstructed classifications. In our original and reconstructed data sets, all images have the same pixel dimensions and the masked regions are also the same in both cases. Thus, the table represents pixel counts between class intersections of the two classification maps. Therefore the sum of all intersections equals the count of all possible pixels of interest in either image. Since, the sum of the entries in the Match table equals the total number of possible pixels; we can also represent these entries as percentages of the total as shown in Table 3.

From the example overlay, we can see that Original Image (OI) Class 1 (C1) overlaps with Reconstructed Image (RI) C1 and RIC2. But, clearly, the largest percentage contributing to our measure of similarity comes from the OIC1 and RIC1 intersection. In our quality metric we choose to "optimize" the total percentage between original and reconstructed classification map intersection by including any contributions for an OI or RI class only once. For example, if we include the RIC1 and OIC1 intersection, we can not consider RIC1 or OIC1 as contributions to any other intersection. From the example Match table, we determine the total best possible percentage comes from the contributions along the table diagonal yielding a 95% level of similarity.

Table 3 Match Table class maps of nearly identical original and reconstructed images

	Original Image (OI) Classification				
Reconstructed Image (RI) Classification		**C1**	**C2**	**C3**	**C4**
	C1	**37.5**	0	0	0
	C2	**2.5**	**10**	0	0
	C3	0	0	**10**	**2.5**
	C4	0	0	0	**37.5**

We execute the quality metric algorithm by selecting the first maximum table entry followed by zeroing out the corresponding row and column. We repeat this process until the entire table is zeroed out. The sum of the maximum entries selected equals our measure of similarity. The second example illustrated by Figure 51 depicts moderately different classification maps between original and reconstructed datacubes. Here, all boundaries have changed between the reconstructed and original image classifications. In this case the Match table yields a slightly different result equal to 90% similarity.

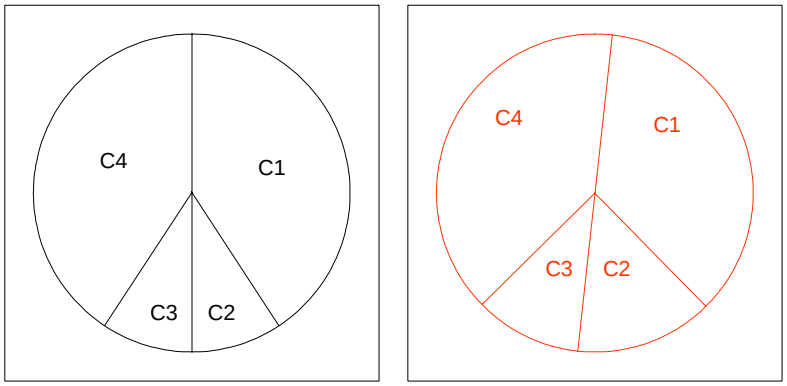

Figure 51. Classification Maps for original and reconstructed imagery with moderate variations

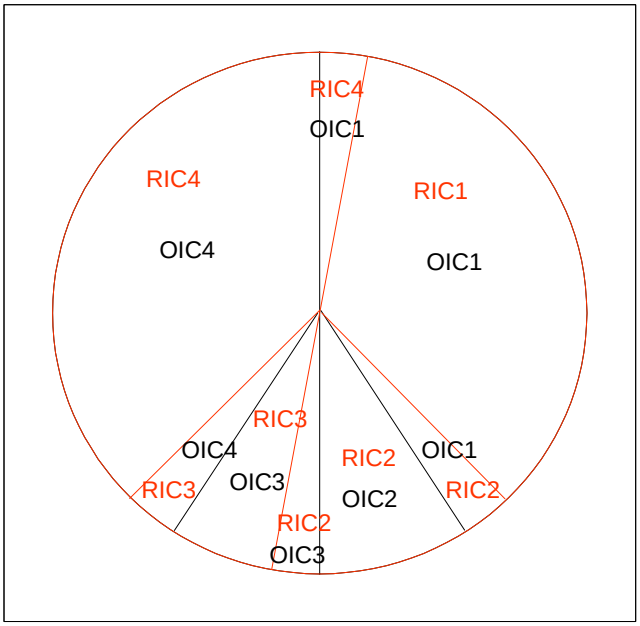

Figure 52. Overlapped class maps for original and reconstructed imagery with moderate variations

Table 4. Match Table for class maps of original and reconstructed imagery with moderate variations

	Original Image (OI) Classification				
Reconstructed Image (RI) Classification		**C1**	**C2**	**C3**	**C4**
	C1	**35**	0	0	0
	C2	**2.5**	**10**	**2.5**	0
	C3	0	0	**7.5**	**2.5**
	C4	**2.5**	0	0	**37.5**

In the third and final example shown in Figure 53 and Figure 54 we depict a case where the classification algorithm yields 5 classes for the CTS reconstruction and 3 classes for the original image. Such a situation is not unusual when using a classification algorithm like DFC and when the CTS reconstruction differs significantly from the original. In this case, the quality metric applied to the results in Table 5 yields 72.5% similarity.

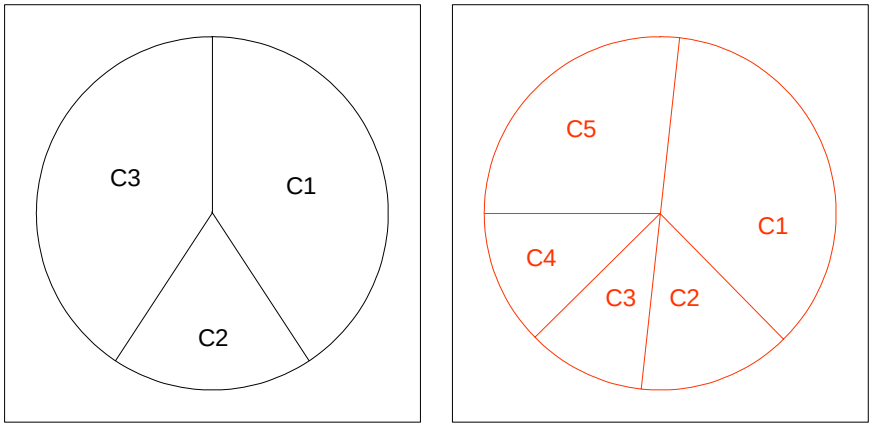

Figure 53. Classification Maps for original and reconstructed imagery with significant variations

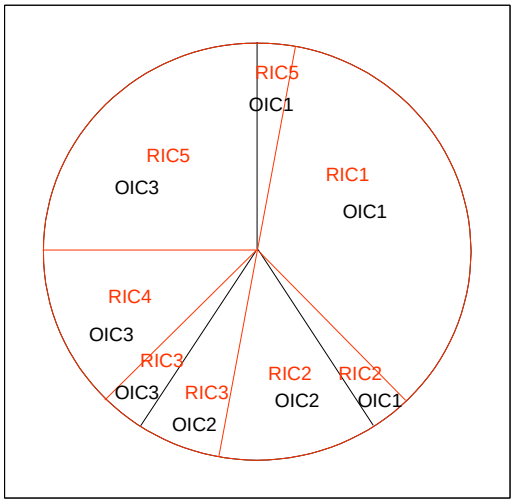

Figure 54. Overlapped class maps for original and reconstructed imagery with significant variations

Table 5. Match Table for class maps of original and reconstructed imagery with significant variations

	Original Image (OI) Classification			
Reconstructed Image (RI) Classification		**C1**	**C2**	**C3**
	C1	**35**	0	0
	C2	**2.5**	**12.5**	**0**
	C3	0	**7.5**	**2.5**
	C4	0	0	**12.5**
	C5	**2.5**	0	**25**

11. Bulk-Classification Results

The results provided in this report describe algorithm performance in terms of the percent match between the original and reconstructed image classification maps. Results are presented for the Iran and Israel data sets. The Iran data set is composed of 256x256 and 512x512 pixel images while the Israel imagery is restricted to only 256x256 pixels. For either Iran or Israel, the 256x256 or 512x512 datacubes were extracted from a single larger image. The Iran 256x256 data is composed of 12 datacubes labeled A thru L and the 512x512 data is composed of 5 datacubes labeled c1, q1, q2, q3, and q4. For the Israel data, 8 datacubes labeled n_1 thru n_8 were used.

This analysis was performed in two parts. These include reconstruction algorithm performance assessments without and then with additional perturbations due to system noise or sensor jitter. The latter part of this analysis is described under the section entitles, "11.6 Sensitivity Analysis". The result plots pertaining to the analysis described here constitutes a great deal information. The majority of these plots are provided in the appendix at the end of this report. Due to the large number of plotted results of this information, only a representative set of plots are provided in the main body of this report.

For all performance analyses, results were generated from the DFC and *k*-means algorithms. In order to determine any net effect from the use of a particular set of spectral bands, 2 sets of spectral bands for the available imagery was analyzed with the two classification algorithms. The two sets of spectral bands chosen for this analysis include bands 1 through 16 for the first set and bands 1 through 13 and 24 through 32 for the second set. Bands 14 through 23 are water absorption bands and were omitted from the second set for that reason.. No significant difference was observed between these two band selections however the results for both sets are provided in the appendix. Also, in the case of the *k*-means, the algorithm was executed for k=3 and k=6. This was done to determine the effect, if any, of the choice of k.

In the plots that follow, we note that *k*-means based quality metric performance results tend to depict larger percentage match values compared to those based on a DFC quality metric. This difference follows from the number of classes that were generated in the two classification approaches. Typically, when large and/or unequal numbers of classes are generated between original and reconstructed classifications (as can be the case of DFC), the tendency will be a reduction in the maximum common pixel/area intersections between classification maps as observed in Figure 54. We can also observe this effect for the *k*-means based quality metric as the value k is increased from 3 to 6. This overall reduction in performance for the k-means quality based metric is illustrated in several examples throughout Appendix C.

11.1 Comparison of Reconstruction Algorithms

Two sets of performance results are provided for both Iran and Israel datasets. In the first set, results are presented that illustrate the relative performance of CTS reconstruction algorithm approaches. The second set illustrates performance of the reconstruction algorithms as a function of the number of principal components constraints from 2 through 6.

11.2 Performance Change by Average Number of Images

The first set of results illustrates performance for the 6 reconstruction algorithms as a function of an average of 6 or 12 images for the 256x256 Iran data. The reason for utilizing the full set and half the set was to determine whether performance remained consistent in this case. For the 512x512 Iran data, performance is shown as a function a 5 image average since only 5 512x512 images were available and a computing an average of results less than 5 would not be considered useful. Given the similar performance between Israel and Iran data sets, only the Iran data results are shown in this section. Results for the Israel data are provided in Appendix C

The results that follow depict an average performance for the MPI, POCS, POCS Filter Constrained (POCSFC), POCS Principal Component Filter Constrained (POCSPCFC), SCA, and SCA Filter Constrained (SCAFC) reconstruction algorithms. Figure 55and Figure 56 illustrate performance for 256x256 and 512x512 datacubes respectively. These results incorporate an average effect of using 2 through 6 principal component constraints for all but the MPI approach. In that case, the only reconstructions produced were based on either 2 principal component constraints or with no constraints at all.

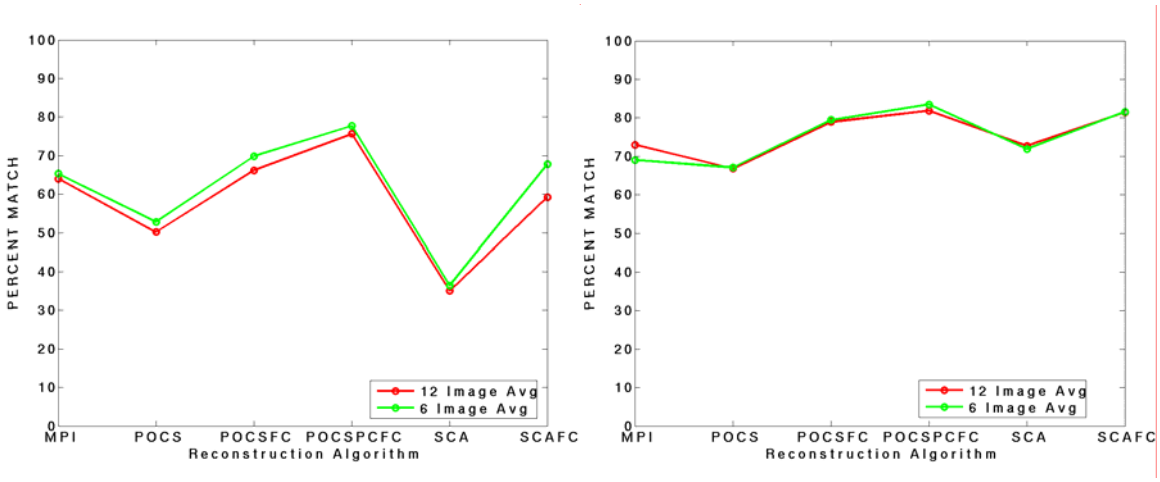

DFC ***k*-means (6 classes)**

Figure 55 Iran 256x256 Images, Bands: 1-16, DFC and *k*-means Classification Algorithms, Performance Change by Average Number of Images

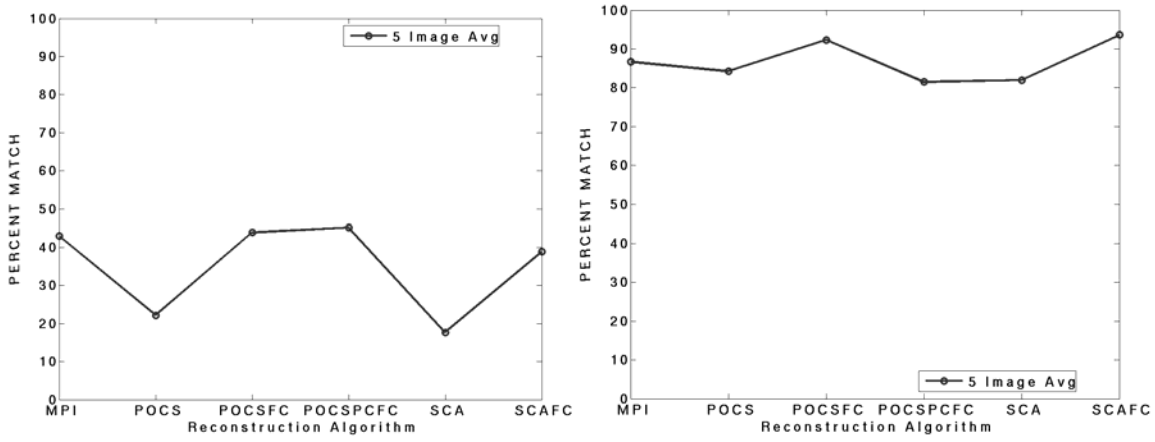

Figure 56 Iran 512x512 Images, Bands: 1-13 and 24-32, DFC and *k*-means Classification Algorithms, Performance Change Over Average of All Images

Observations and Conclusions Regarding Average Number of Images

The plots in Figure 55 illustrate that performance steadily improves for the POCS-based approaches starting from the POCS to the POCSFC and POCSPCFC algorithms. The same is true for the SCA based approaches SCA and SCAFC. These results are consistent with the design and implementation assumptions for these algorithms. However, from these plots, it is not necessarily clear there is a clear winner between best of these two reconstruction approach subsets POCSPCFC and SCAFC. From these same plots, one might assume that the MPI algorithm also appears to perform competitively. However, we recall that MPI results only include performance results from 2 variations in principal components where as the other approaches include performance results from 5 principal component variations. Therefore a comparison of MPI against the other reconstruction approaches is not a fair one to make. Likewise, from Figure 56 we can make some similar observations from the DFC based quality metric. Although the improvement trend is not as clear for the POCS-based reconstruction, the general trend between the reconstruction approaches follows that discerned from the 256x256 imagery. Alternately, the *k*-means results for the 512x512 imagery do not seem to correspond. That is, the POCSPCFC performance results are expected to be at least as good as those of the POCSFC. Instead, they tend to b slightly worse. However, the performance manifested for the k-means based quality metric is generally very high throughout and the performance difference between all approaches here tends to be between 5 to 10 percent.

11.4 Performance Change by Number of Principal Component Constraints

The second set of results illustrates CTS reconstruction algorithm performance as a function of the number of PCs (2-6) used as reconstruction constraints. MPI results are only available for constraints of 2 principal components. Therefore comparisons with MPI are not very useful and are not considered in this analysis. The results included here illustrate performance for Iran 256x256 and 512x512 imagery. These are shown in Figure 57 and Figure 58 respectively. Results for Israel 256x256 pixel imagery depict different characteristics from those seen in the Iran data and for that reason are provided in Figure 59. In addition, the full complement of available imagery is used for Iran and Israel imagery in either the 256x256 or 512x512 pixel cases.

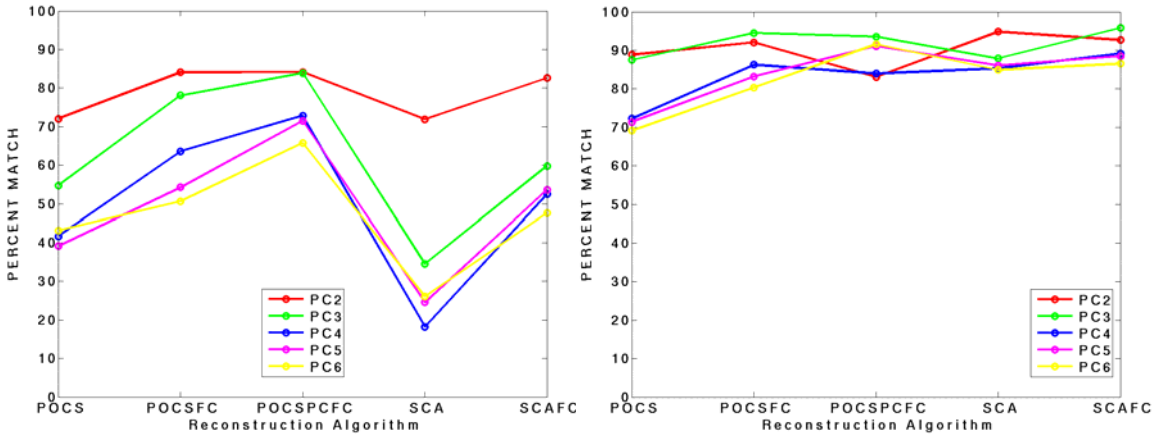

DFC *k*-means (3 classes)

Figure 57 Iran 256x256 Images, Bands: 1-16, DFC and *k*-means Classification Algorithms, Performance Change by Number of Principal Component Constraints

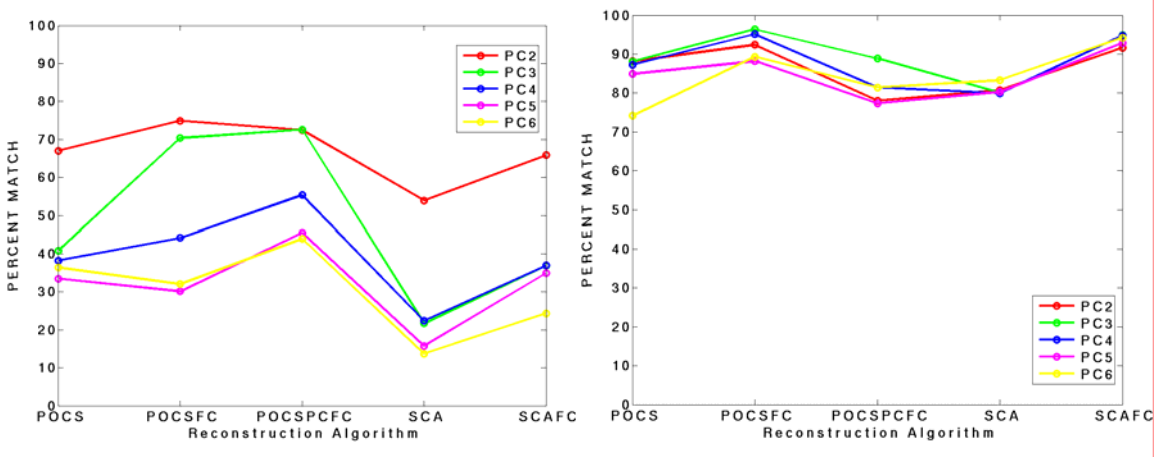

DFC *k*-means (3 classes)

Figure 58 Iran 512x512 Images, Bands: 1-16, DFC and *k*-means Classification Algorithms, Performance Change by Number of Principal Component Constraints

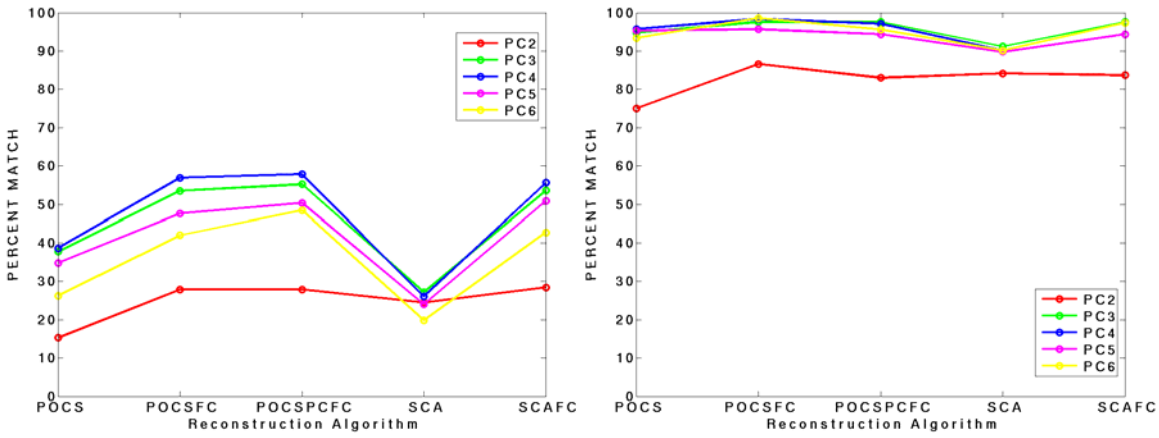

DFC ***k*-means (3 classes)**

Figure 59 Israel 256x256 Images, Bands 1-16, DFC and *k*-means Classification Algorithms, Performance Change by Number of Principal Component Constraints

11.5 Observations and Conclusions Regarding Classification as Function of PCs

The results derived in this analysis depict reconstruction algorithm performance trends that are very similar to those seen and discussed in Appendix C. In addition, the results shown here in Figure 57 and Figure 58 for the Iran 256x256 and512x512 imagery both follow a very similar trend. However, the trend observed between the Iran and Israel data sets is significantly different. For example, in the DFC based quality measure, the 2 principal component constraint (PC2) results tend to be the most significant for the Iran data sets and the least significant for the Israel data. Outside of that constraint case, we also note that performance generally degrades for all CTS reconstruction approaches with increasing numbers of principal component constraints. The first observation would seem to indicate a data dependency in which the Iran data was best characterized by the first 2 principal components and in the case of the Israel data the contrary is true. Our second observation indicates that given the best principal component characterization, increasing the number of principal components only serves to degrade performance of the reconstruction algorithm by introducing additional noise.

11.6 Sensitivity Analysis

The second phase of our study was a sensitivity analysis directed at determining the effects of varying signal to noise ratio (SNR) and sensor jitter. In the interest of time, the number of images used in these studies was limited to 6 out of either 12 or 8 total datacubes for Iran and Israel data respectively. For SNR, analysis was further limited to reconstructions constrained by only 5 principal components. For the jitter experiments, the plots incorporate average results for principal constraints or 2 through 6. However,

the jitter quality metric results for reconstructions with 5 principal component constraints are also available in Appendix C. In all plots shown here, results pertaining to the MPI reconstruction approach are excluded since this approach is considered to be non-competitive with the other reconstruction approaches discussed here.

11.6.1 Signal to Noise Ratio

Figure 60 and Figure 61 results were generated from the Iran and Israel data sets respectively and include representative plots that illustrate performance changes due to signal to noise ratios of 10, 100, 200, 400 compared to results on noiseless data. The results due to noiseless data are shown in black.

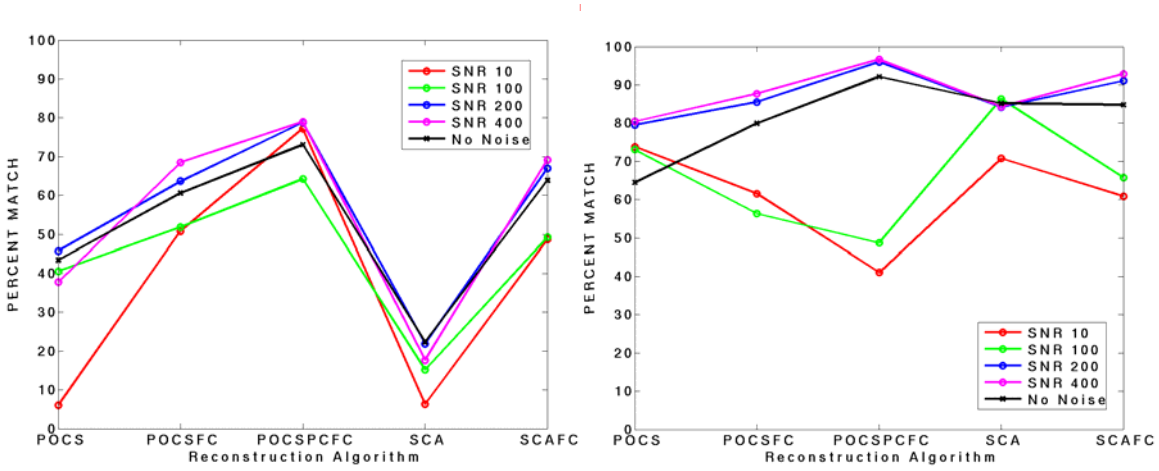

DFC ***k*-means (3 classes)**

Figure 60 Iran 256x256 Images, Bands: 1-16, DFC and *k*-means Classification Algorithms, Signal to Noise Ratio (SNR) Analysis

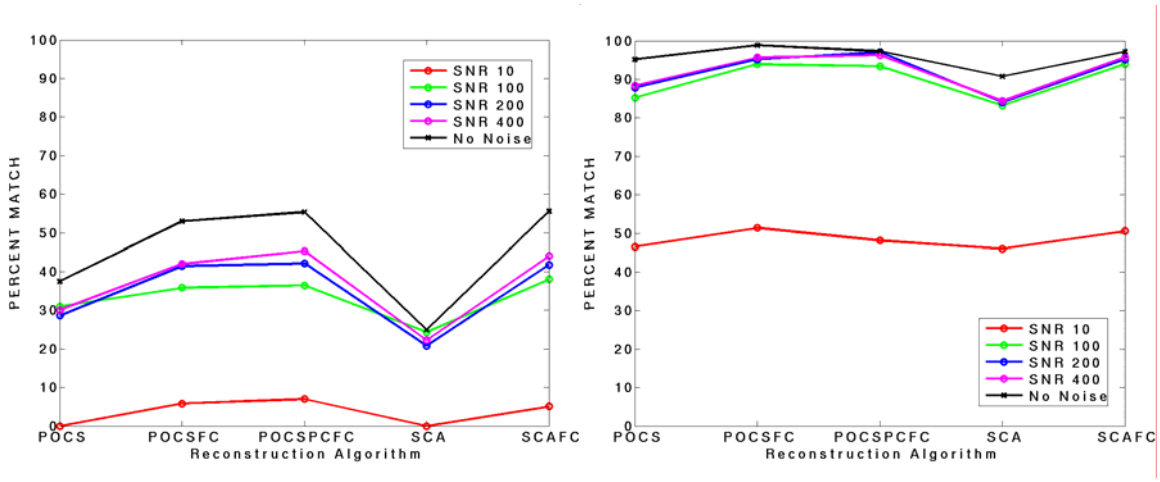

DFC ***k*-means (6 classes)**

Figure 61 Israel 256x256 Images, Bands 1-16, DFC and *k*-means Classification Algorithms, Signal to Noise Ratio (SNR) Analysis

The results achieved from this analysis generally indicate that as SNR increases, performance increases as well with similar relative changes between algorithms. For the Iran data, we observe that the noiseless data performance tends to be slightly worse than for the SNR 200 and SNR 400 cases. This is somewhat perplexing but we see that this observation holds true for quality metrics based on both DFC and *k*-means algorithms. This would seem to indicate that the result is data dependent since it was reflected in two very different classification approaches. Although the results are not remarkably better, one supposition is that the introduction of a small amount of noise into the Iran data altered the feature space distributions of the reconstructed data in manner that yielded a more similar classification map. The hypothesis that this is a data dependent issue is further supported by the results for the Israel data reconstructions. Here, performance increases significantly from an SNR of 10 and regularly improves for SNR's of 100, 200, 400 and is best of all for noiseless data reconstructions.

11.6.2 Jitter Analysis

Figure 62 and Figure 63 results were generated from the Iran and Israel data sets respectively and include representative plots that illustrate performance changes due to increasing amounts of jitter from 10 through 1 where 10 is the least jitter and all are compared to results on jitterless data. The results due to jitterless data are shown as the thin red line.

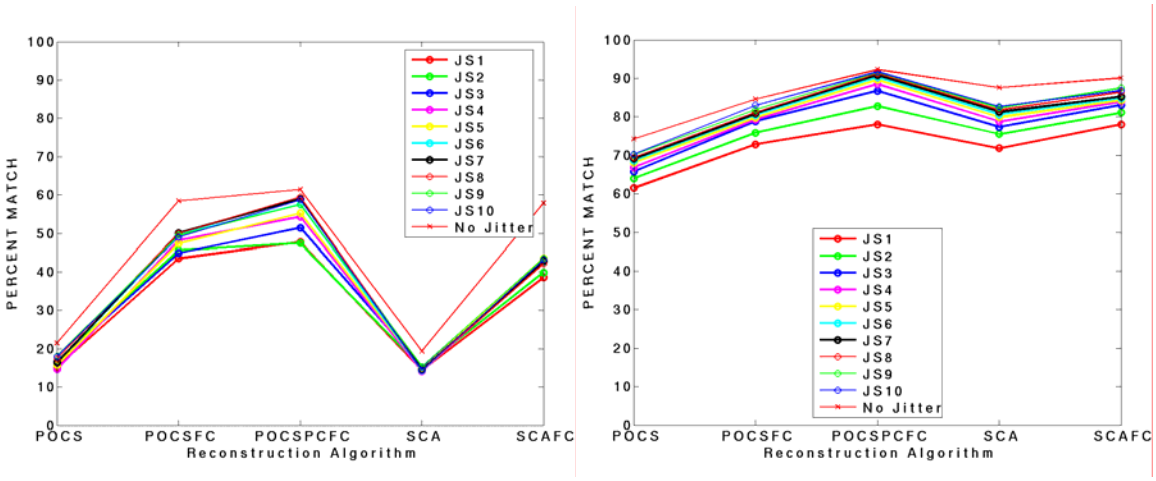

DFC ***k*-means (3 classes)**

Figure 62 Iran 256x256 Images, Bands: 1-13 and 24-32, DFC and *k*-means Classification Algorithms, Jitter Analysis

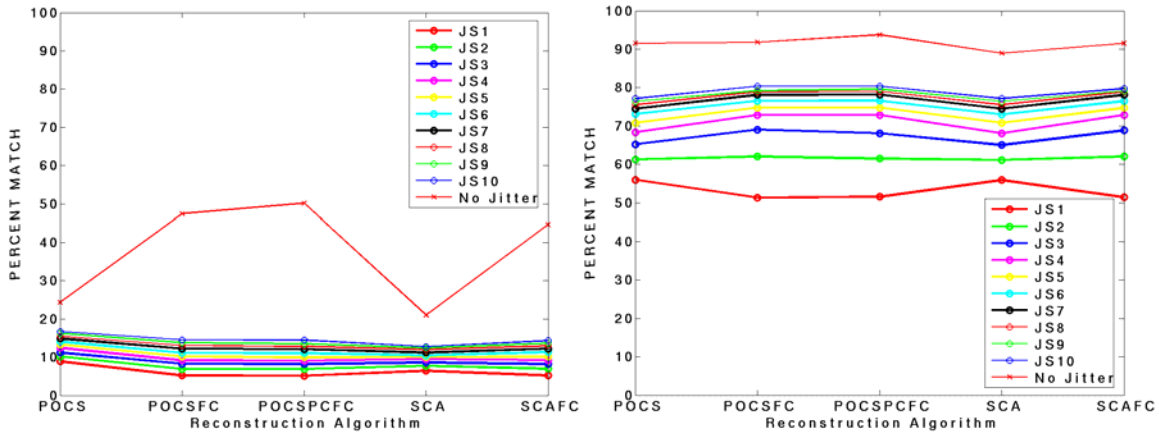

DFC ***k*-means (3 classes)**

Figure 63 Israel 256x256 Images, Bands 1-13 and 24-32, DFC and *k*-means Classification Algorithms, Jitter Analysis

From both DFC and *k*-means based quality metrics the performance results achieved from the jitter analysis reflect a very regular improvement corresponding to decreasing jitter. These results correspond to our expectations of decreasing performance with increasing sensor jitter. We note that the results tend to be more tightly packed for the DFC based approach. A clearer view of both these plots can be seen in larger versions in Appendix C.

12. Conclusions

Throughout the course of this project, we have produced a set of tools which may be used to assess the applicability of non-conventional spectral imaging systems to missions associated with space-based optical sensors. Specifically, algorithms were developed to simulate CTS imagery, reconstruct spectral datacubes, and assess new mission-based reconstruction quality metrics. New reconstruction algorithms which incorporate filtered image constraints were developed and evaluated within this framework. These algorithms were found to outperform their non-filter-constrained counterparts in terms of both spectral accuracy and bulk classification accuracy. While POCSFC also performed well throughout the point target experiments, POCS consistently provided smaller spectral angles for target spectra. The relative performance of these algorithms is of course highly dependent upon a multitude of variables including the spatial and spectral frequency content of a given scene, the number of principal components used to constrain reconstructions, the region from which these PCs are calculated and the number of projection images. Future efforts should explore this trade space and compare the sensitivity of filter and non-filter constrained algorithms to each of these variables. For example, one might predict that a reduced number of projection images would be required when filter constraints are available. In addition, a study designed to select an

optimum filter set for a combined CTS and standard spectral imager should be undertaken during the design phase of such a system.

While we were successful in setting up the tools and framework for answering many questions regarding CTS utility to space-based platforms, we were only able to perform a limited set of analyses with these tools. For example, the impacts of inaccurate STF measurements were not investigated as part of this effort. This is a critical issue for space-based systems which may not have on-board methods for performing corrections of this crucial variable in CTS reconstructions. Along these same lines, we restricted our analysis to a PSF that provided point-to-point mapping. In other words, we did not develop algorithms to incorporate multi-pixel PSFs or field dependent aberrations. We also did not address the need to optimize these reconstruction algorithms for speed or memory consumption. A study that looked at the possibility of operating CTS reconstruction algorithms with compressed data and/or a compressed STF would be very valuable to the space-based application of CTS. In addition, although we established the tools and methods for performing sensitivity analyses against error sources, we were limited by time to assessing the impacts of only two such sources on bulk-classification accuracy. A more complete assessment of these and other system-dependent impacts would be strongly recommended as part of any CTS design process. Finally, it should be noted that although the majority of this work is highly specific to CTS systems, the innovative methods developed for assessing bulk-classification capabilities may be used to compare the classification accuracies associated with any number of spectral imaging systems.

Appemdix A

Table A-1. Material distributions for the Nadir viewing Israel North datacubes. Materials with less than 1% contribution are not included in this list.

	Material		*Cube 1*	*Cube 2*	*Cube 3*	*Cube 4*	*Cube 5*	*Cube 6*	*Cube 7*	*Cube 8*
1	**Water**		0%	14%	0%	1%	1%	2%	1%	18%
2	**Old snow (1000 micron radius)**		0%	0%	0%	0%	0%	0%	0%	0%
4	**Compacted soil**		55%	50%	31%	51%	34%	37%	61%	36%
5	**Tilled soil on june 30 chgd to same as compacted**		9%	4%	11%	8%	15%	12%	13%	2%
6	**Sand**		1%	0%	0%	0%	0%	0%	0%	0%
7	**Limestone and silt**		8%	11%	12%	2%	1%	3%	3%	3%
8	**Irrigated low vegetation**		3%	0%	2%	6%	21%	20%	4%	1%
9	**Meadow grass**		1%	1%	4%	3%	4%	2%	0%	2%
10	**Scrub**		1%	3%	1%	3%	2%	2%	2%	2%
11	**Broadleaf forest**		4%	4%	10%	5%	12%	8%	4%	3%
14	**Asphalt**		0%	0%	9%	0%	0%	2%	0%	10%
15	**Concrete**		0%	0%	0%	0%	0%	0%	0%	1%
16	**Grass scrub mix**		1%	1%	2%	3%	3%	1%	0%	1%
17	**Urban residential**		0%	0%	2%	0%	0%	2%	0%	8%
18	**Urban commercial**		0%	0%	12%	0%	0%	1%	0%	6%
20	**Broadleaf and brush mix**		1%	2%	2%	1%	2%	3%	2%	3%
21	**Wet soil**		0%	0%	0%	0%	0%	0%	0%	0%
24	**Rock 30 and soil 70 mix**		14%	10%	2%	17%	5%	5%	11%	4%

Table A-2. Material numbers for the Nadir-viewing Iran North Datacubes.

#	**Material**	#	**Material**
1	Water	12	Pine forest
2	Varnished sandstone	13	Tundra
3	Mixture of material 6 & 7 (rock & silt-sand)	14	Asphalt
4	Dry silt-salt flats	15	Concrete
5	Wet silt-salt playa	16	Metal building roof
6	Silt-sand	17	Urban residential
7	Rock	18	Urban commercial
8	Irrigated low vegetation	19	Dummy replacement for polarized water (now 28)
9	Meadow grass	20	Seaice (3 meters thick)
10	Scrub	21	Old snow (1000 micron radius)
11	Broadleaf forest		

Appendix B

1000 Targets

Targets

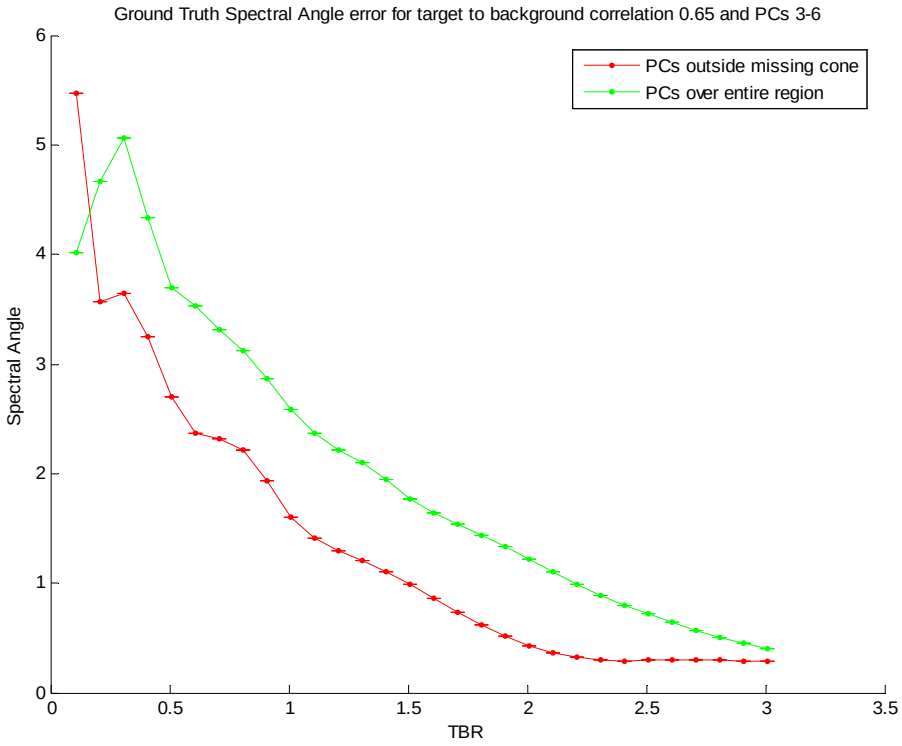

Figure B1.

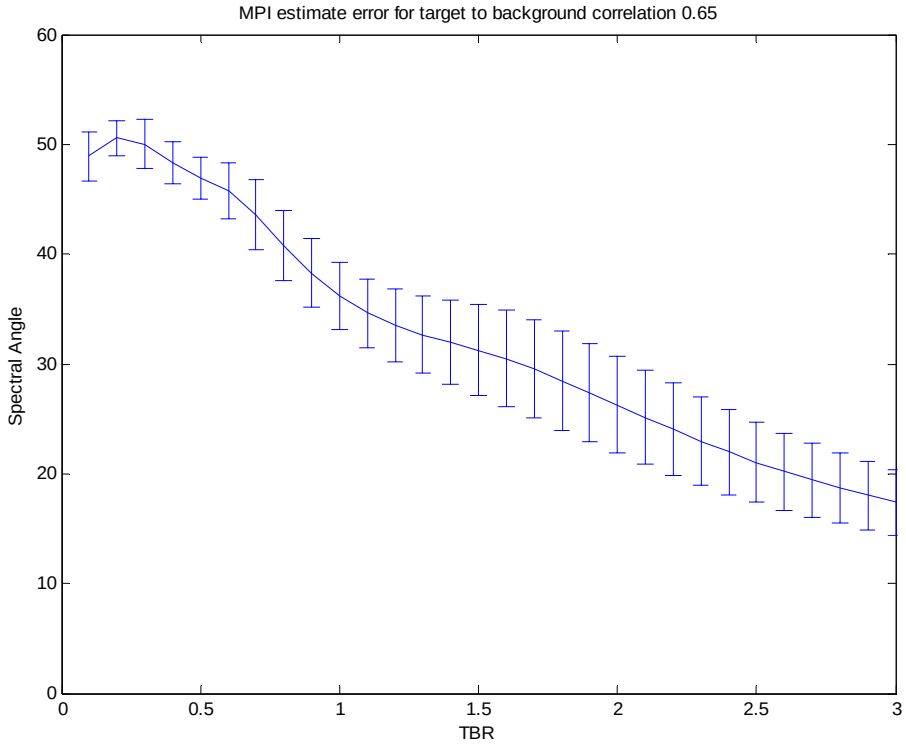

Figure B2.

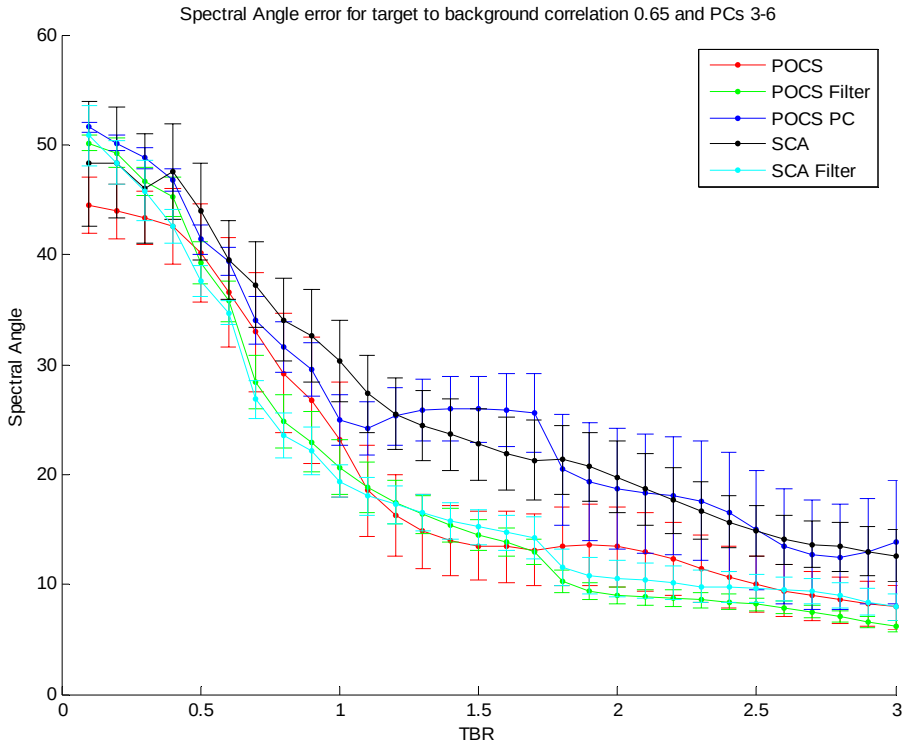

Figure B3.

Background

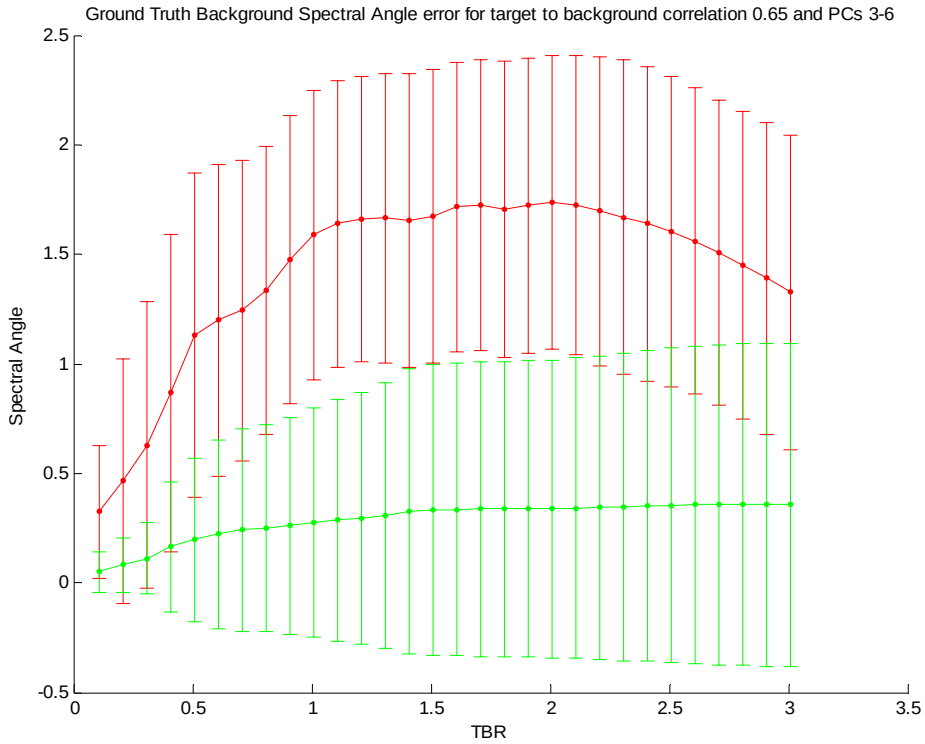

Figure B4.

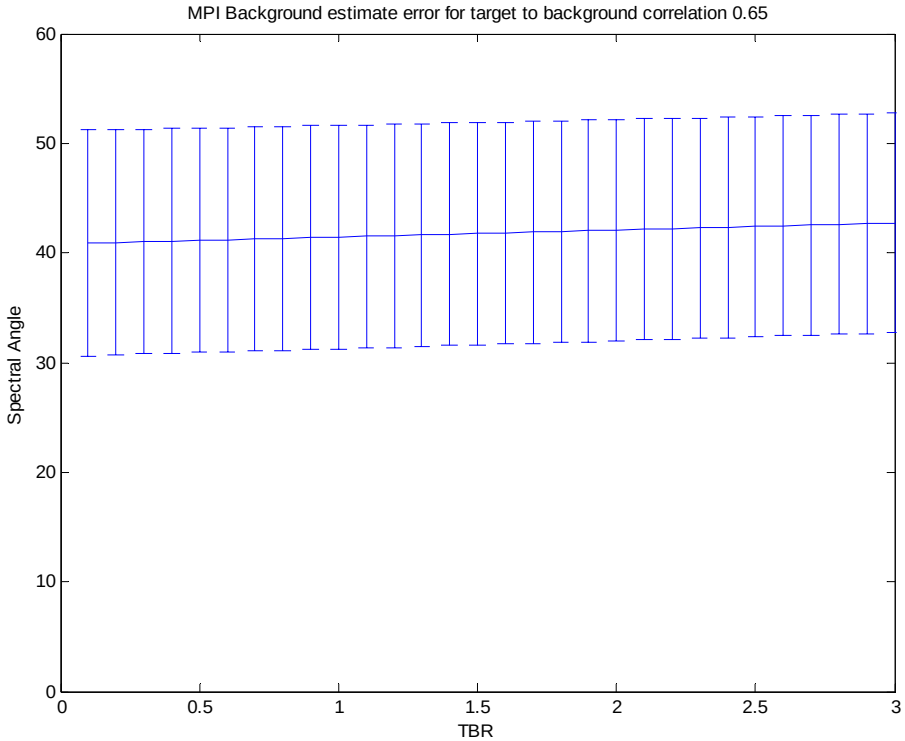

Figure B5.

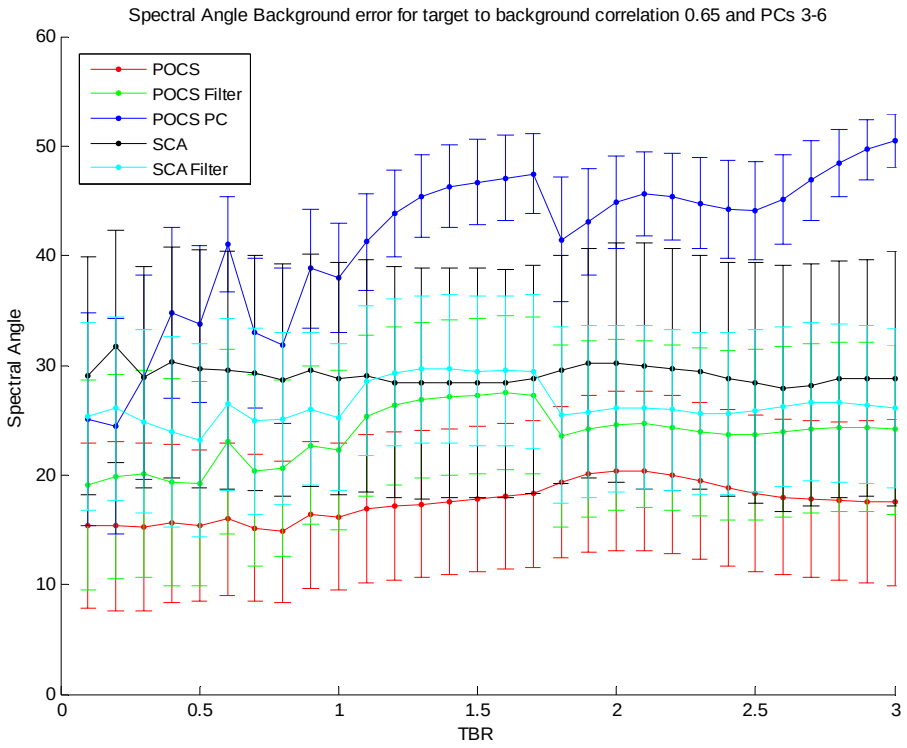
Spectral Angle Background error for target to background correlation 0.65 and PCs 3-6
POCS
POCS Filter
POCS PC
SCA
SCA Filter
Spectral Angle
TBR
0
10
20
30
40
50
60
0
0.5
1
1.5
2
2.5
3

Figure B6.

Correlation Results

Targets

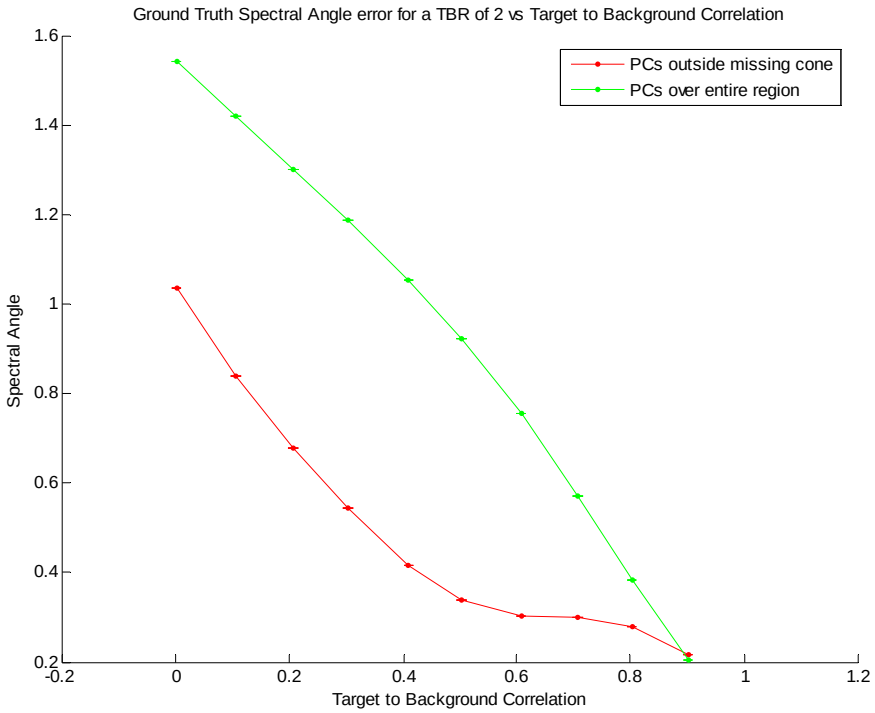

Figure B7.

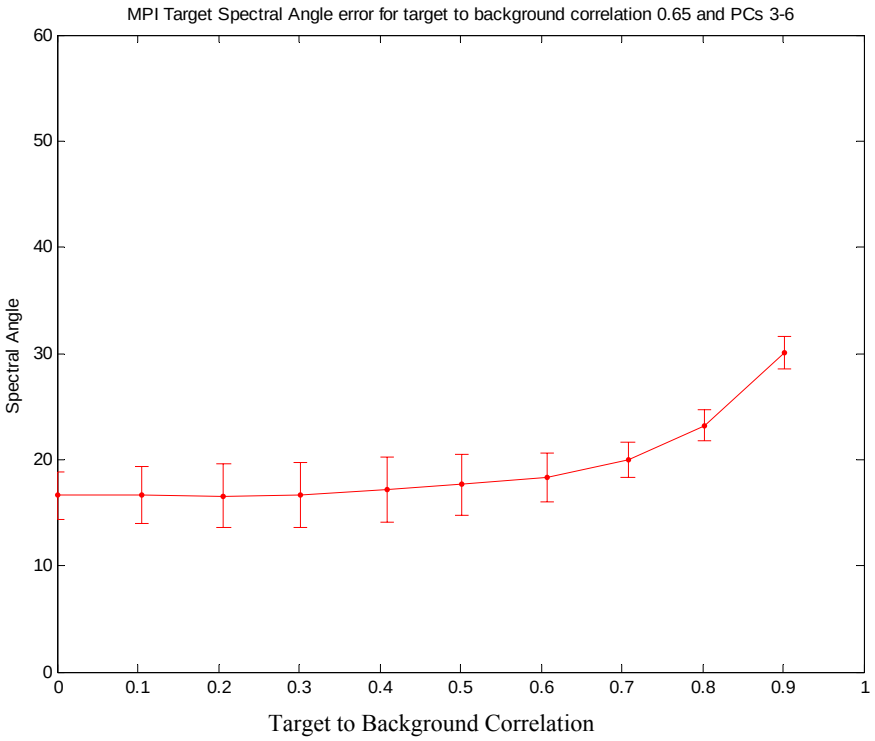

Figure B8.

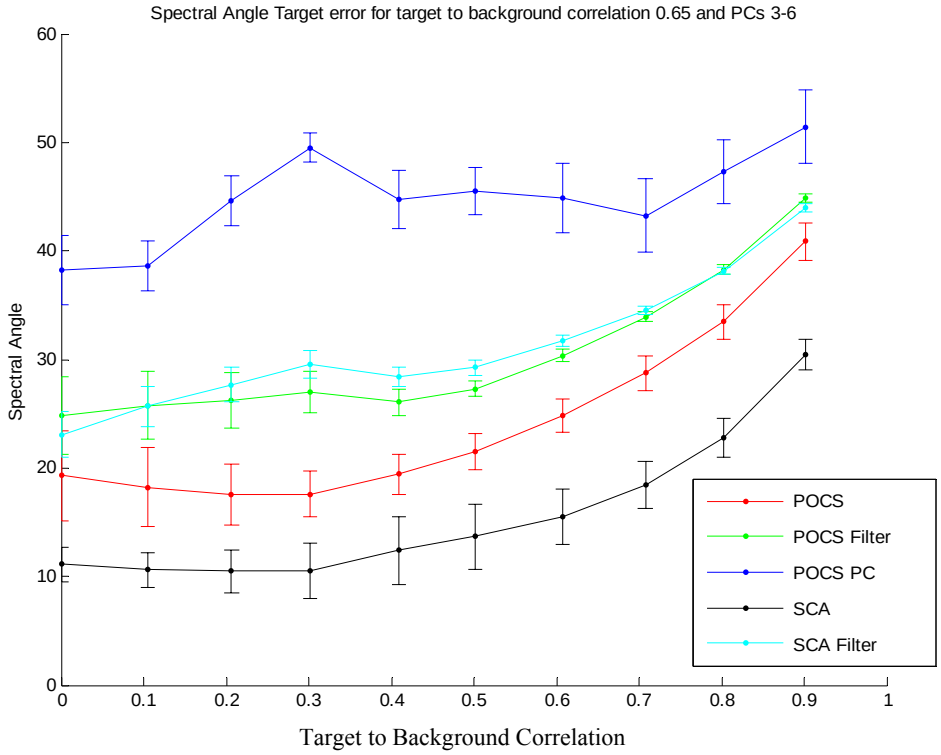

Figure B9.

Background

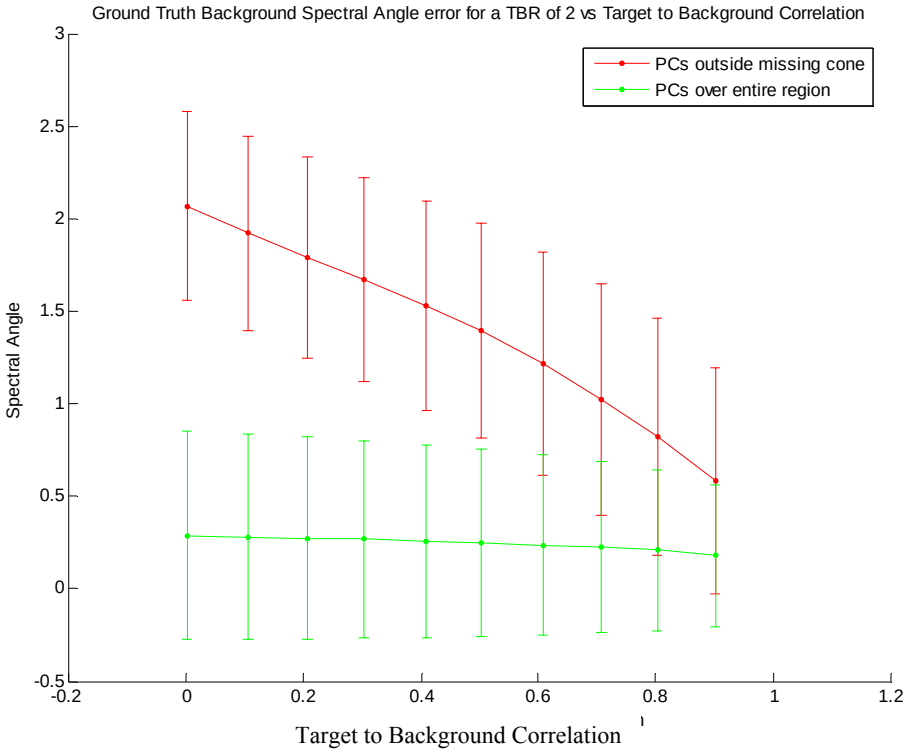

Figure B10.

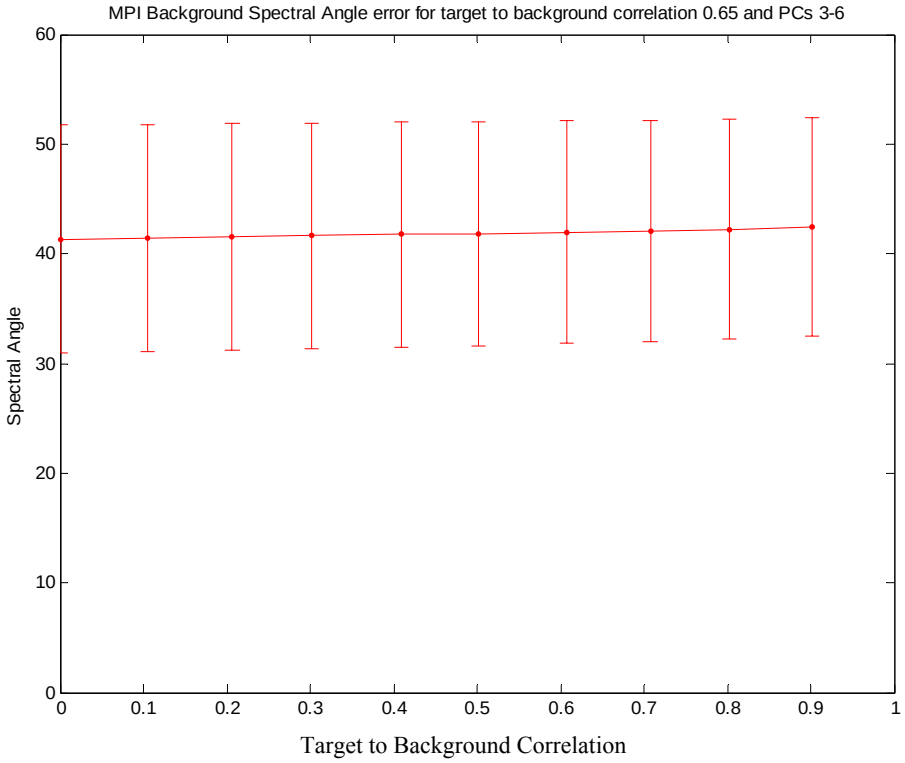

Figure B11.

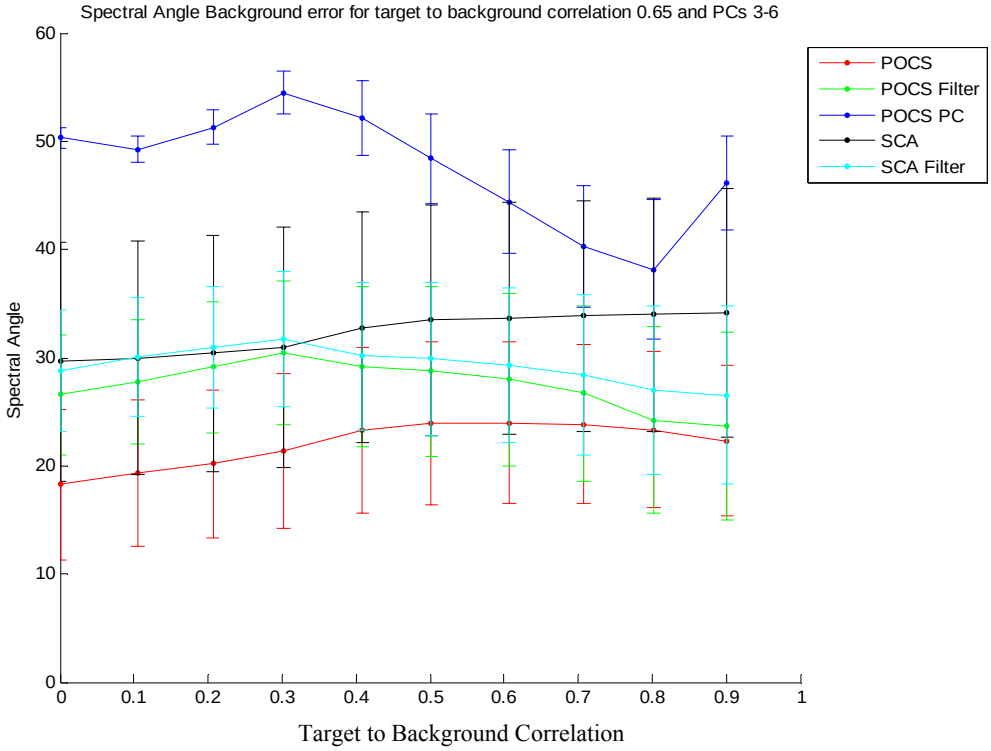

Figure B12.

100 Targets

Targets

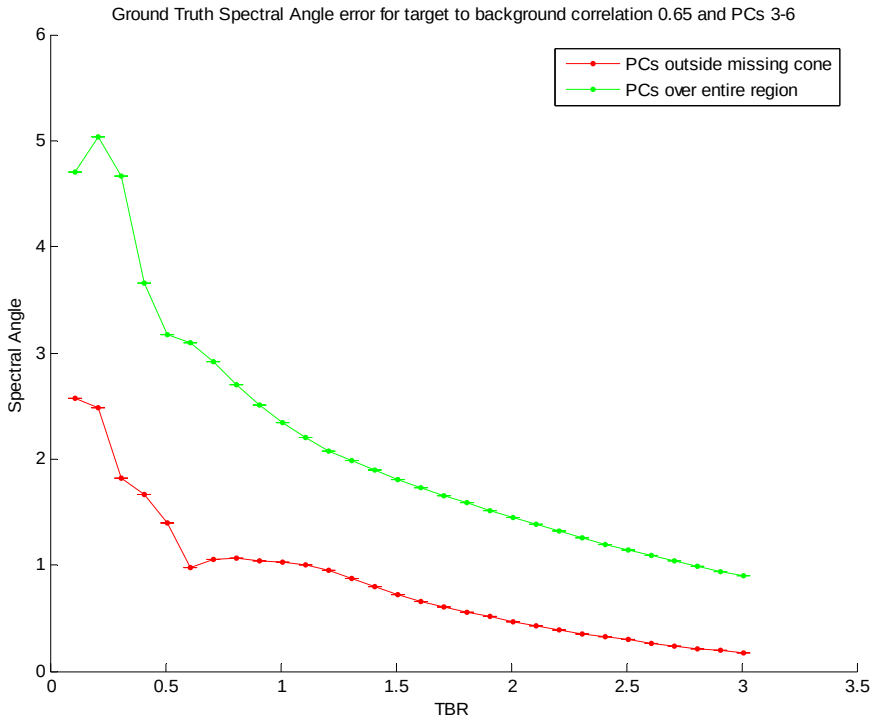

Figure B13.

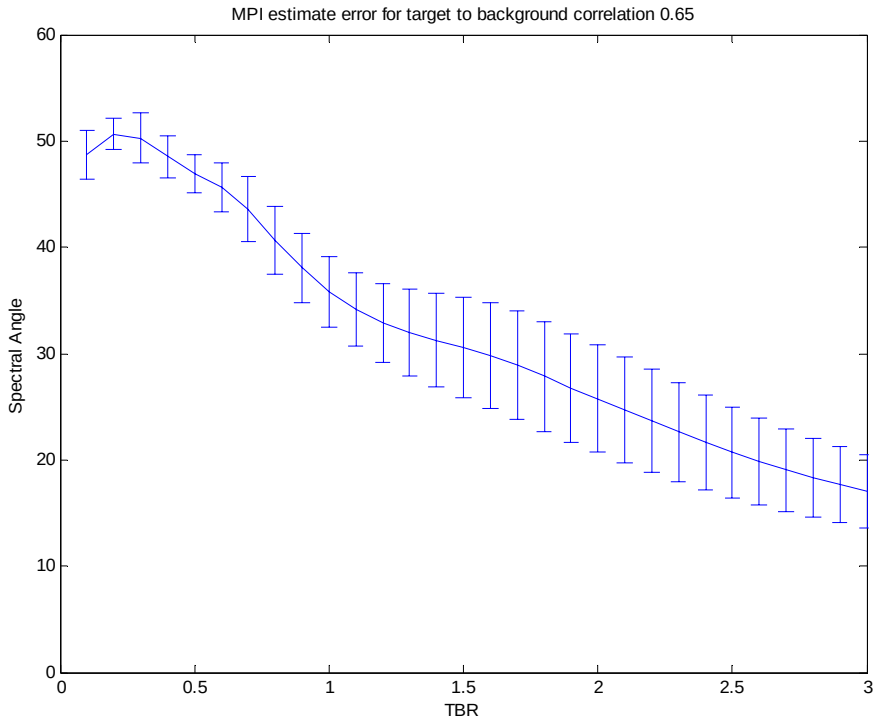

Figure B14.

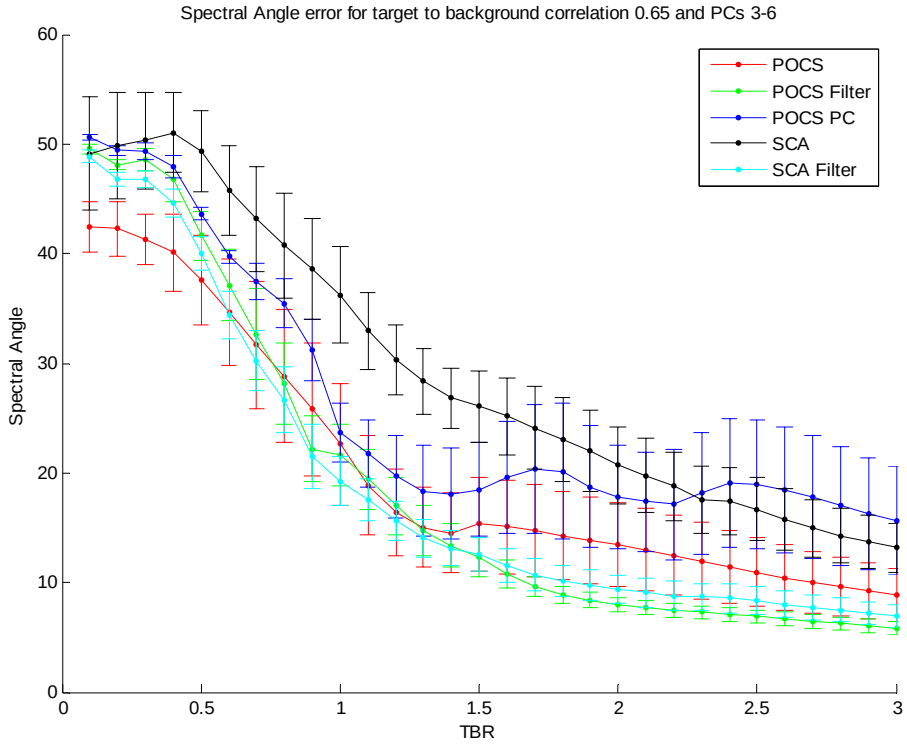

Figure B15.

Background

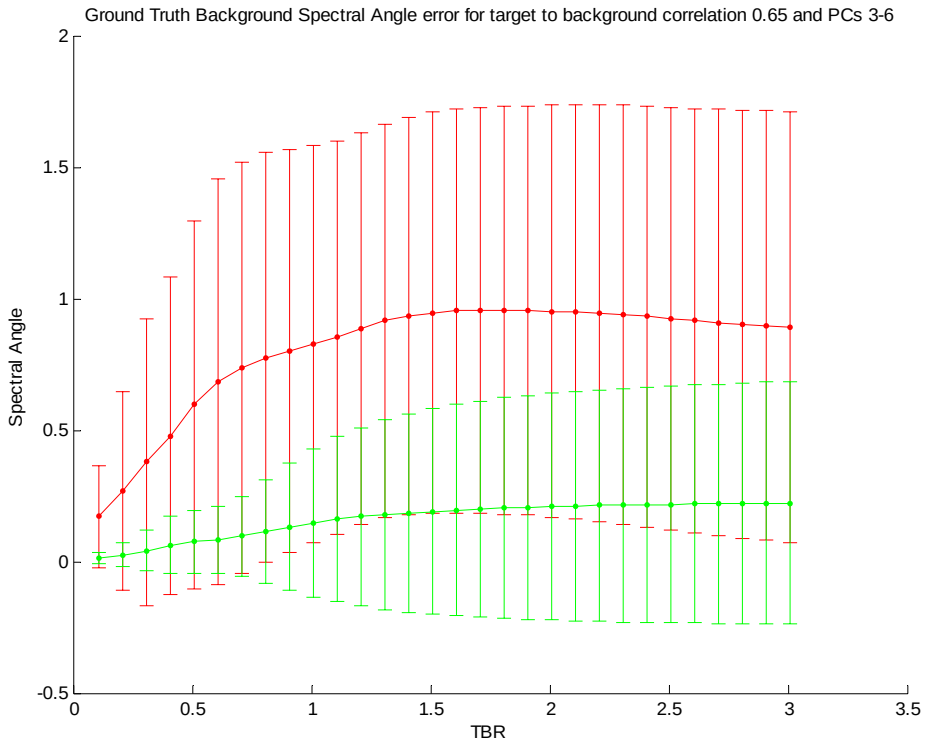

Figure B16.

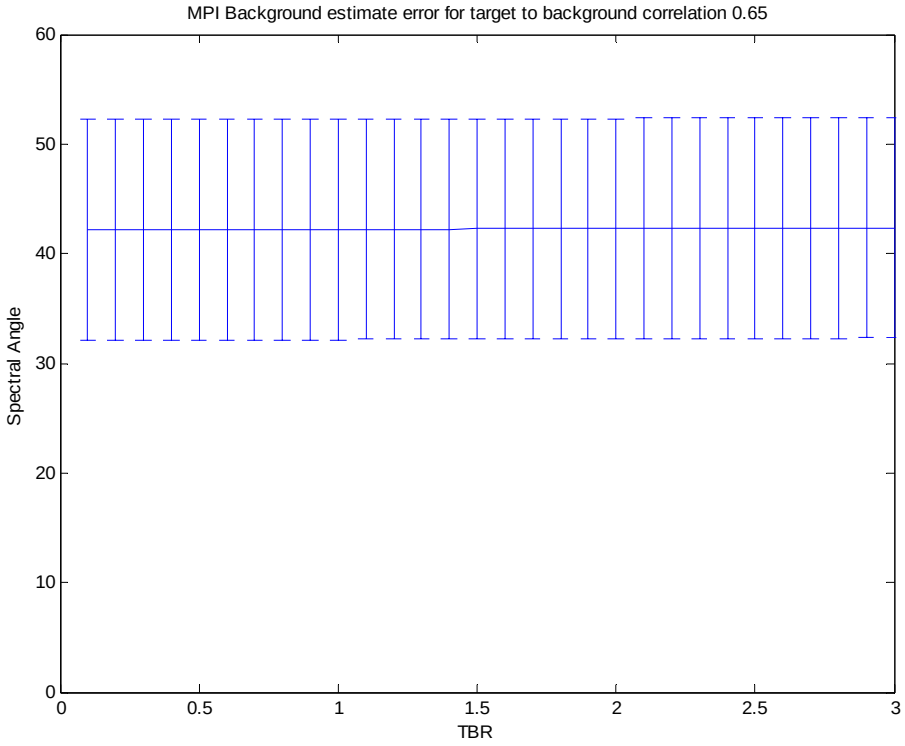

Figure B17.

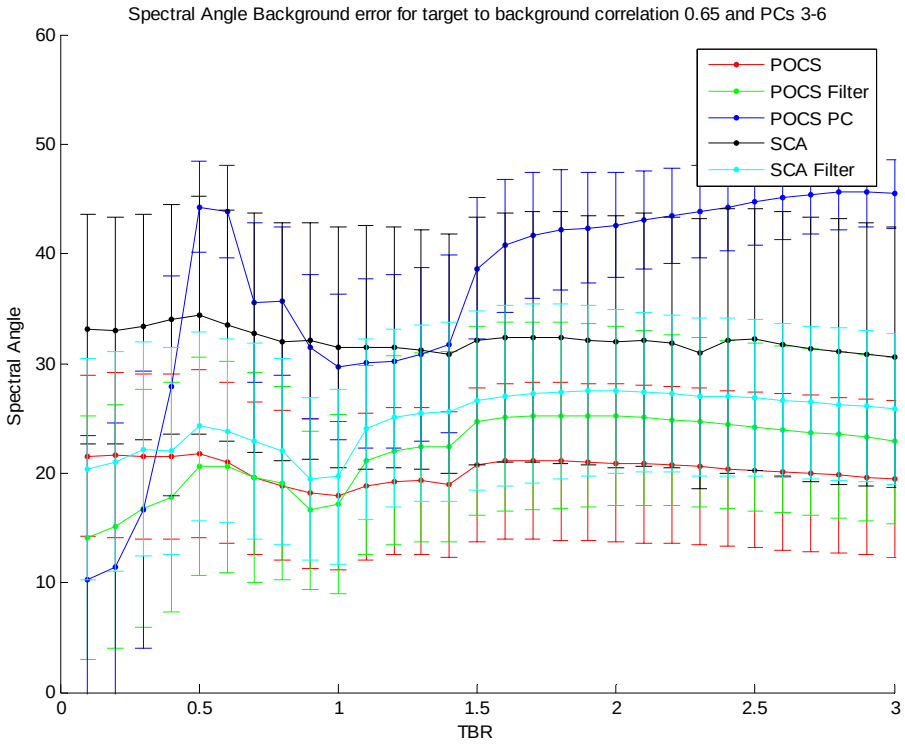

Figure B18.

Correlation Results

Targets

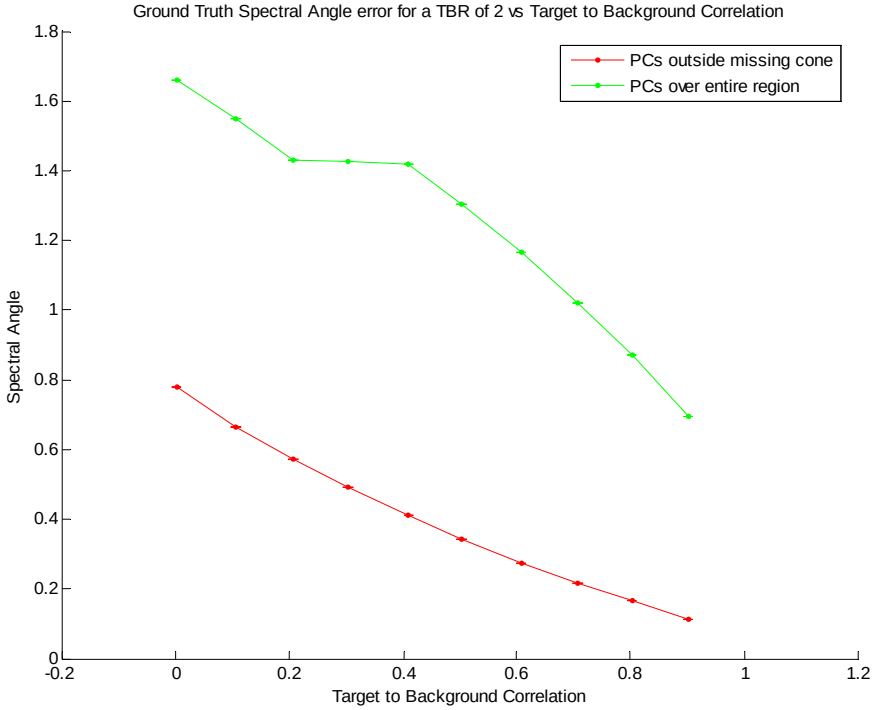

Figure B19.

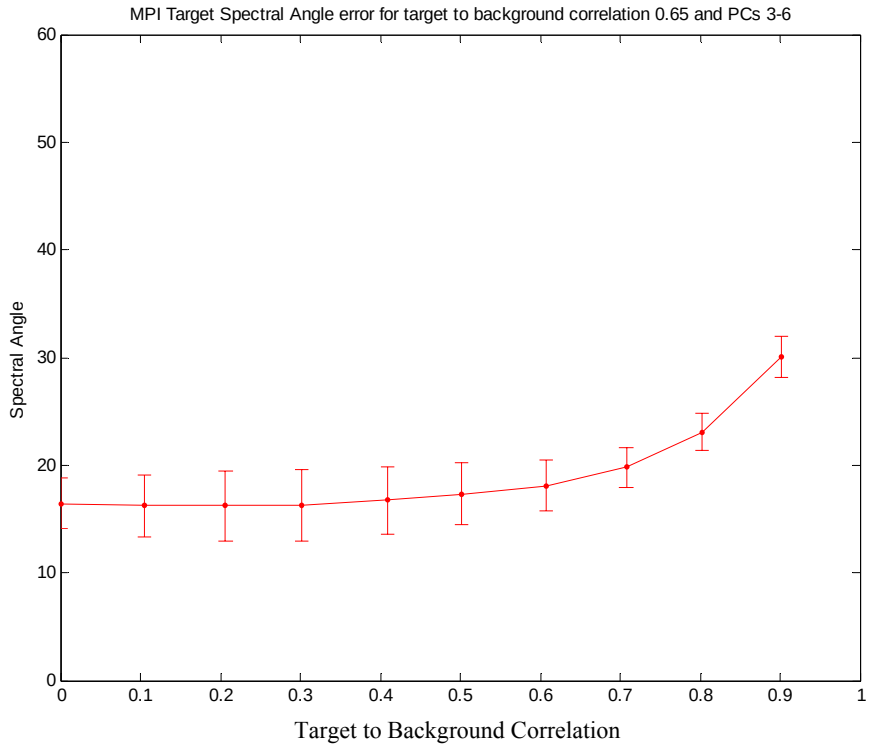

Figure B20.

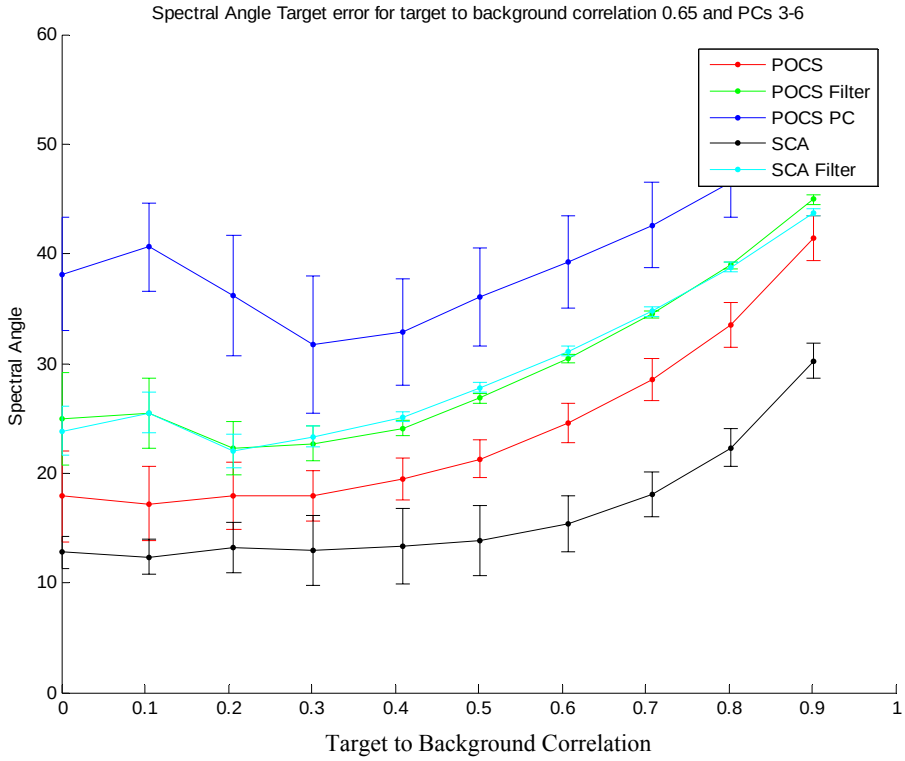

Figure B21.

Background

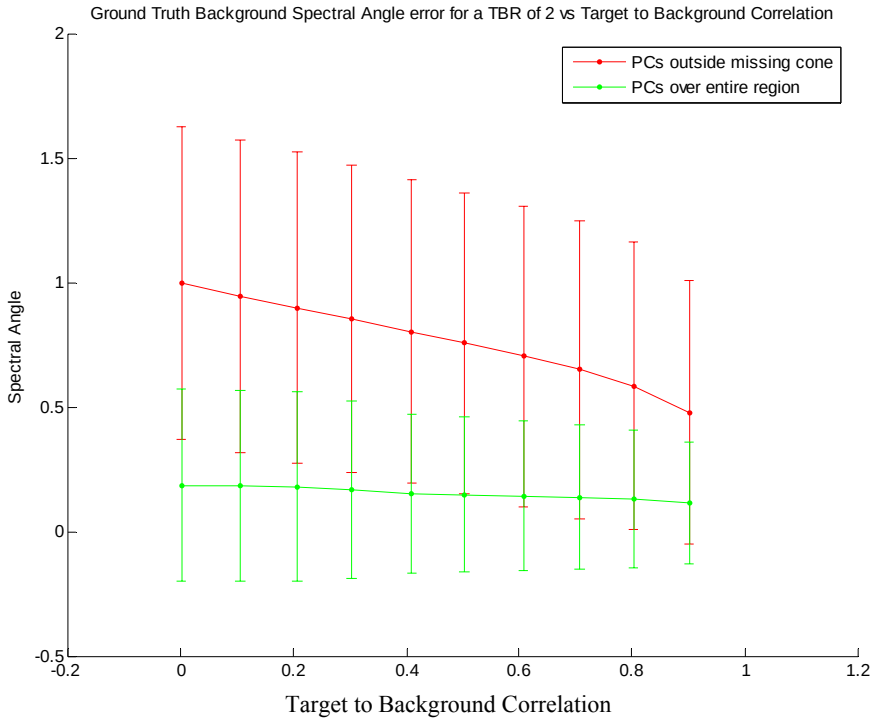

Figure B22.

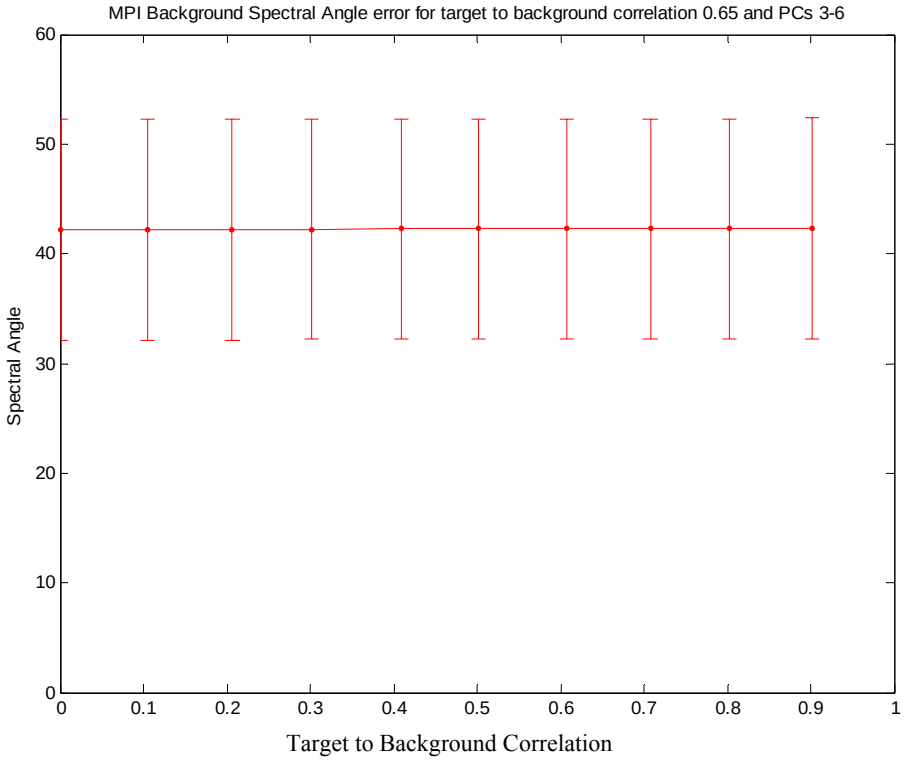

Figure B23.

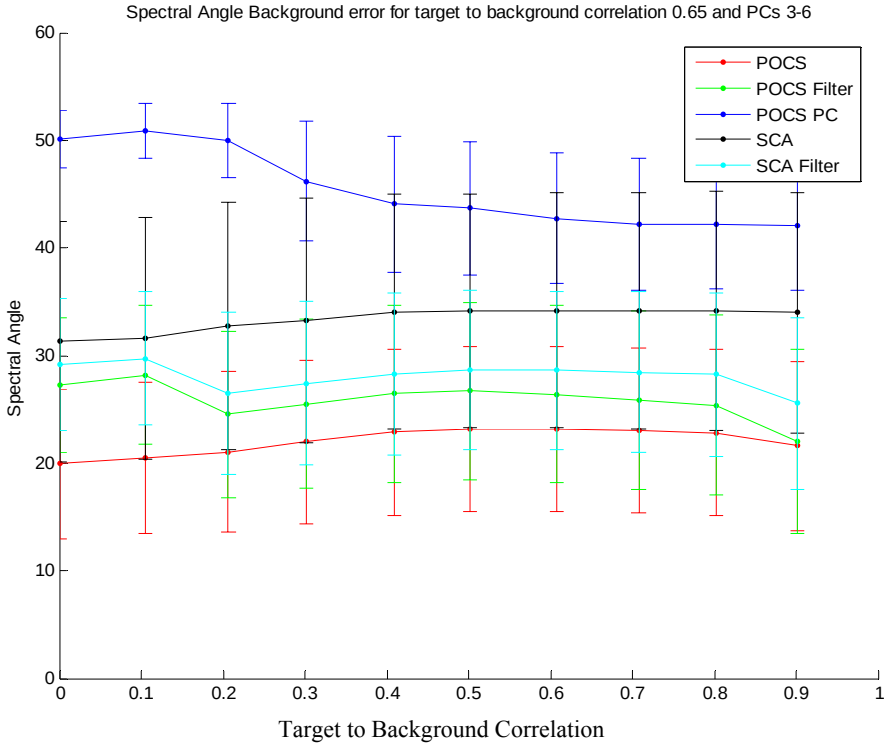

Figure B24.

10 Targets

Targets

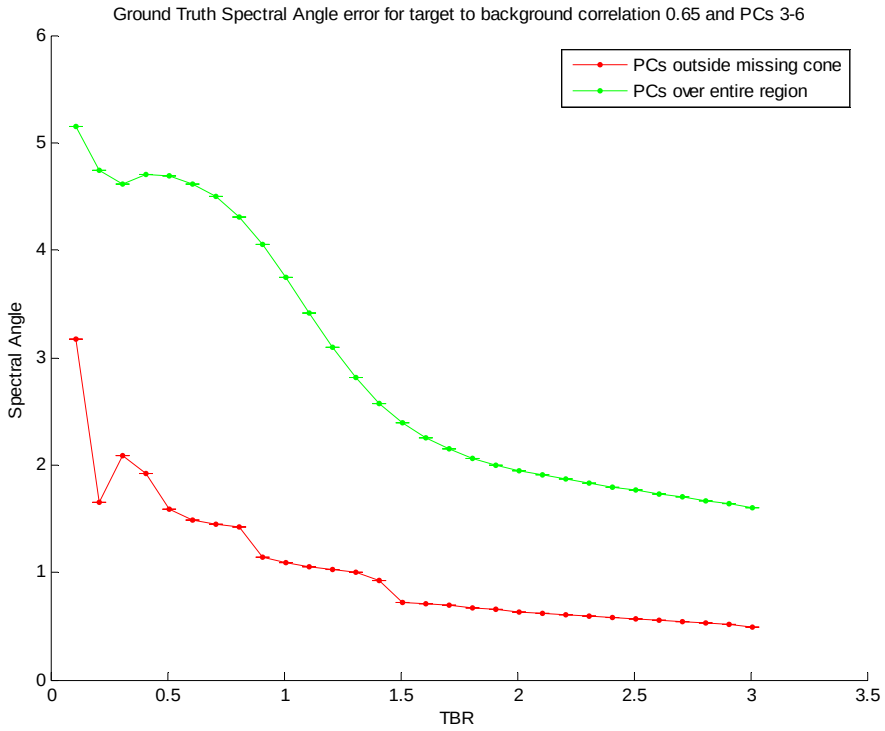

Figure B25.

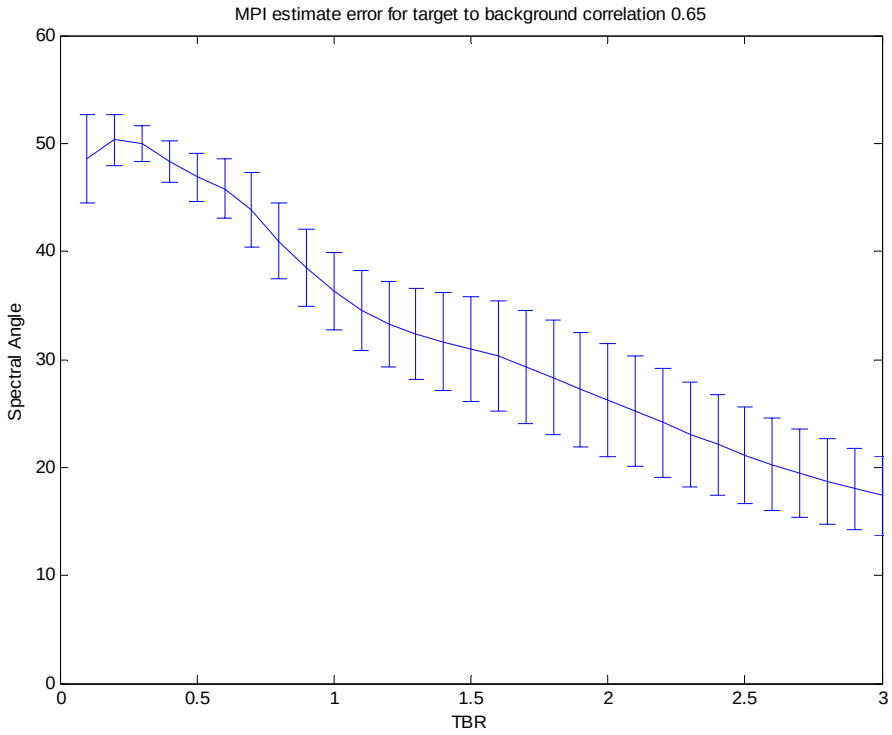

Figure B26.

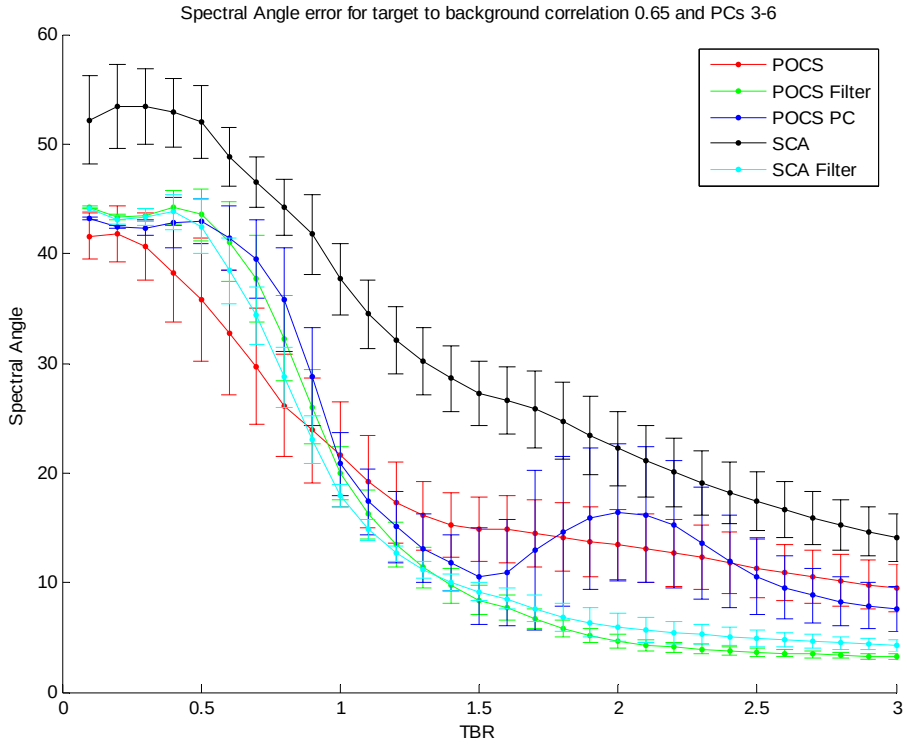

Figure B27.

Background

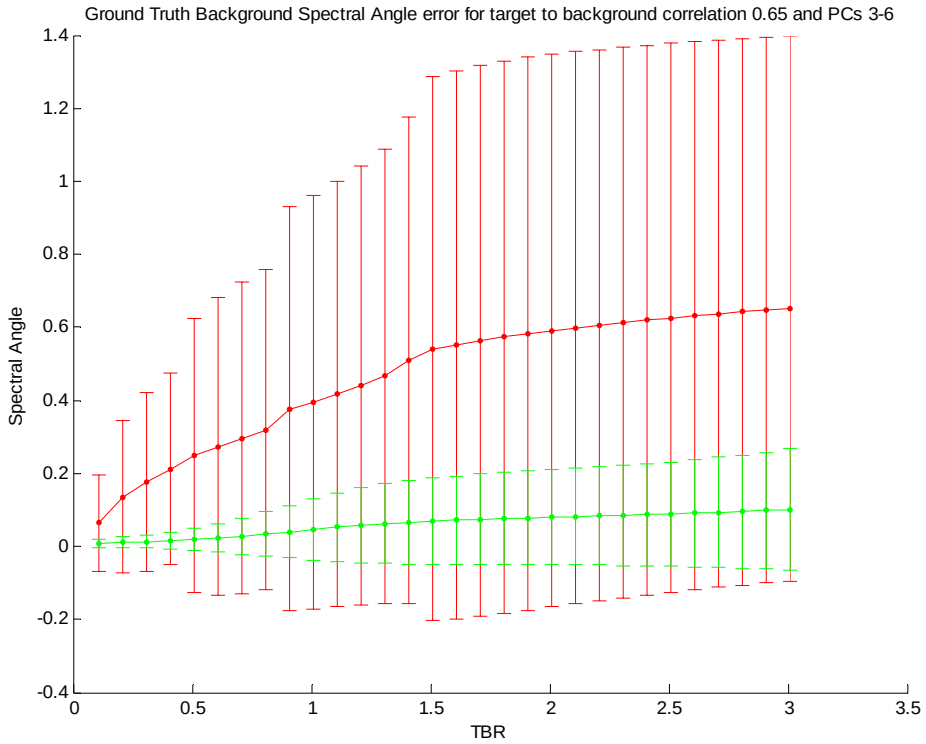

Figure B28.

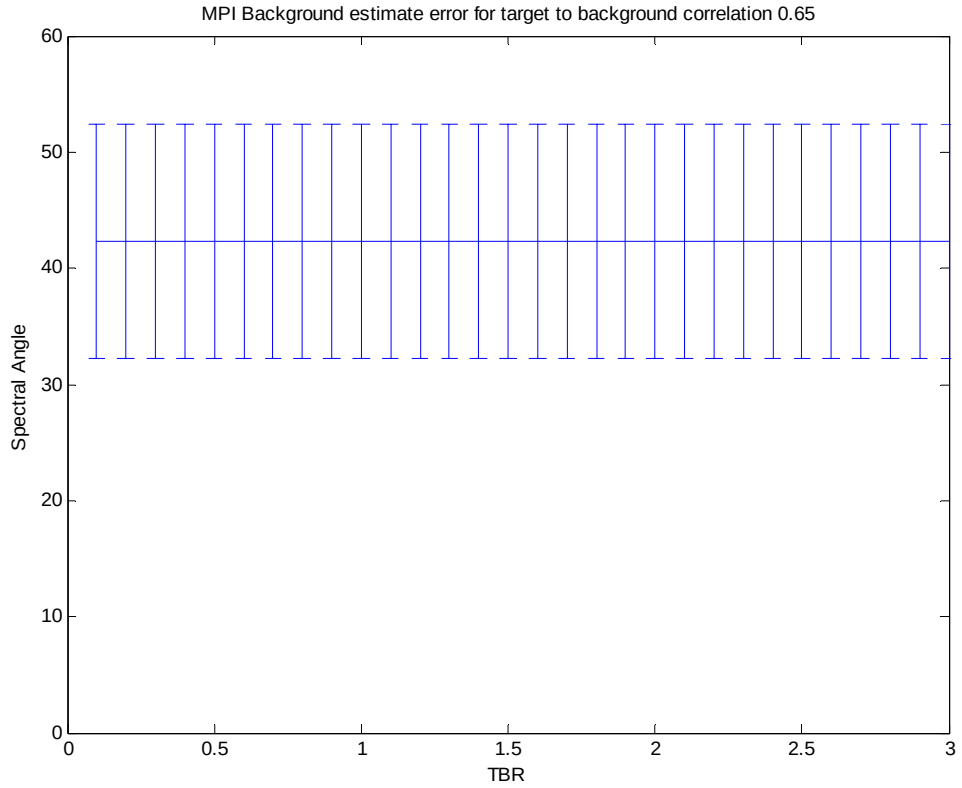

Figure B29.

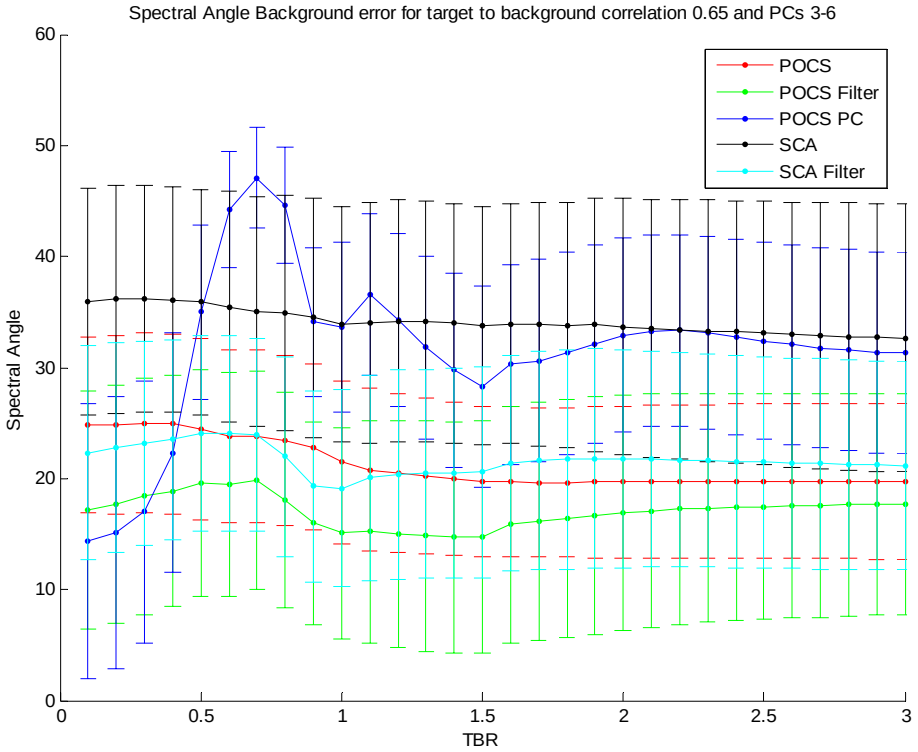

Figure B30.

Correlation Results

Targets

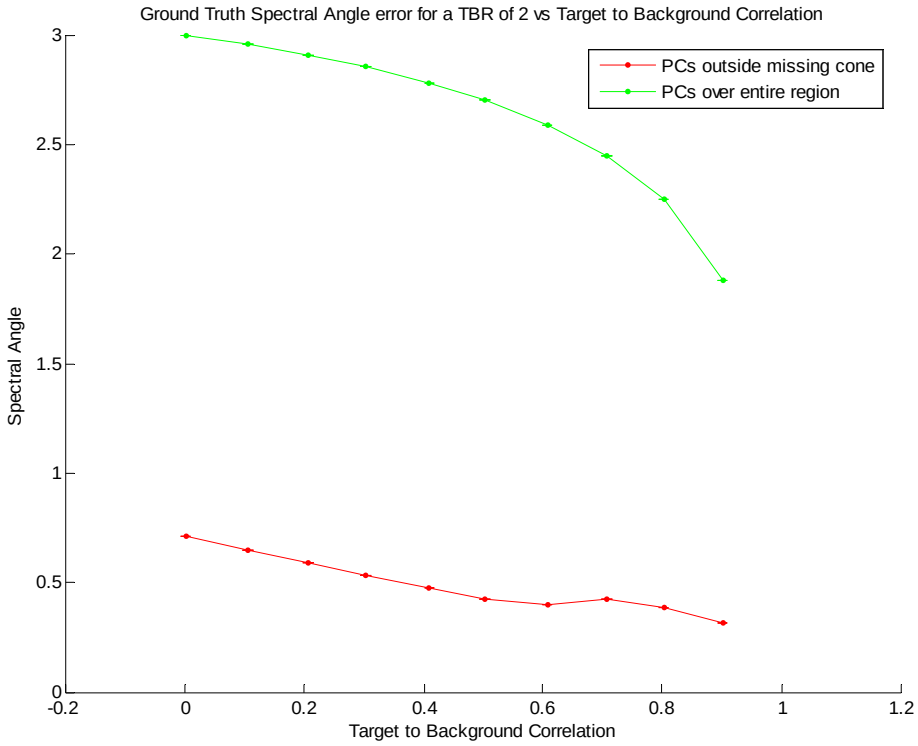

Figure B31.

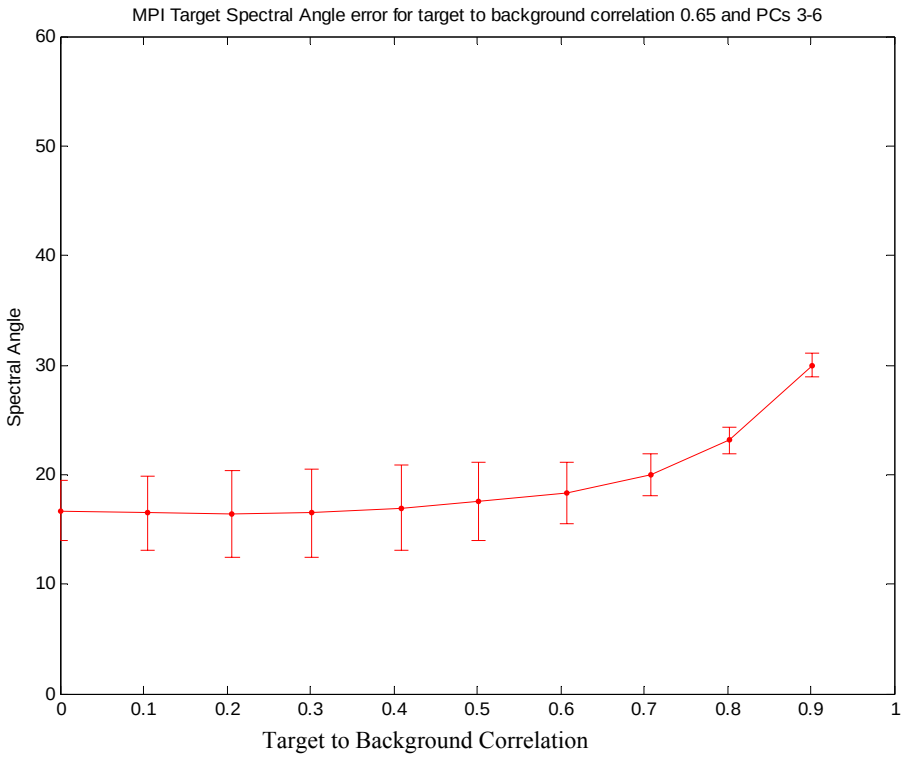

Figure B32.

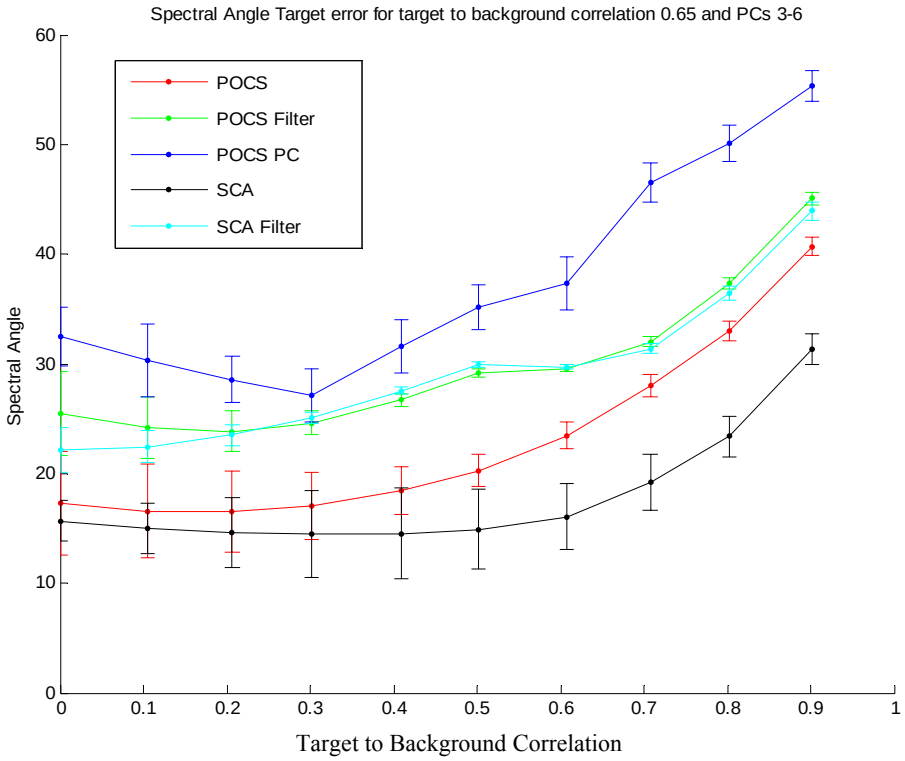

Figure B33.

Background

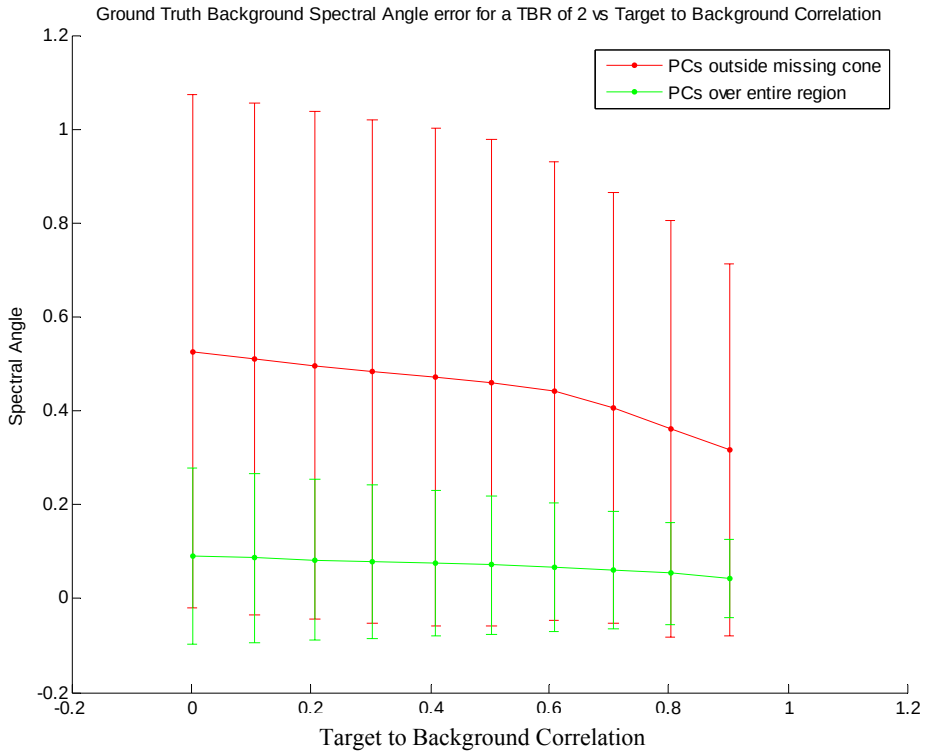

Figure B34.

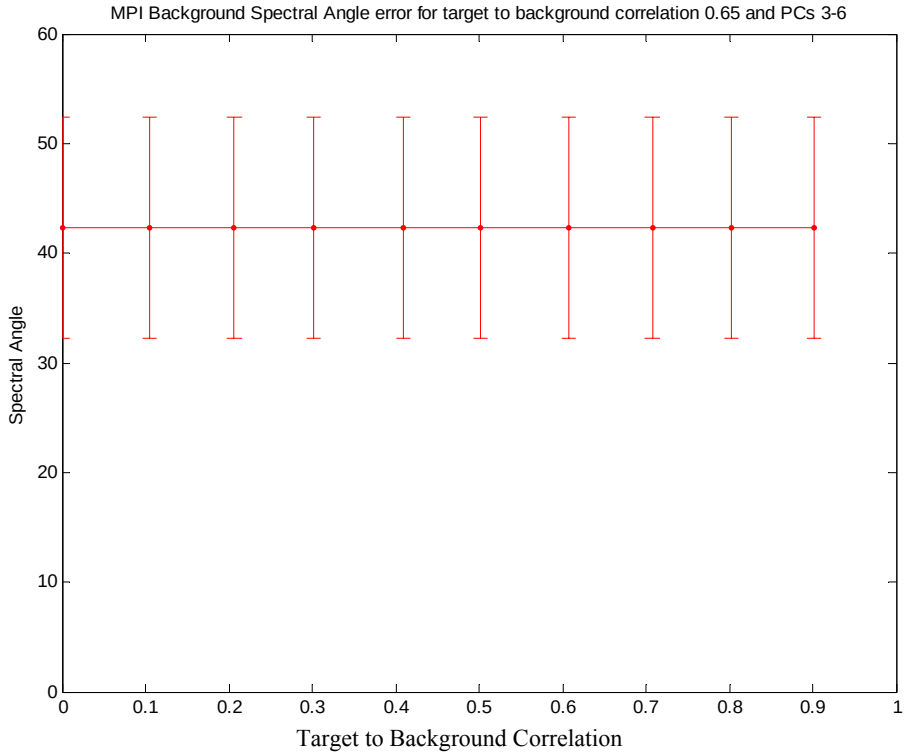

Figure B35.

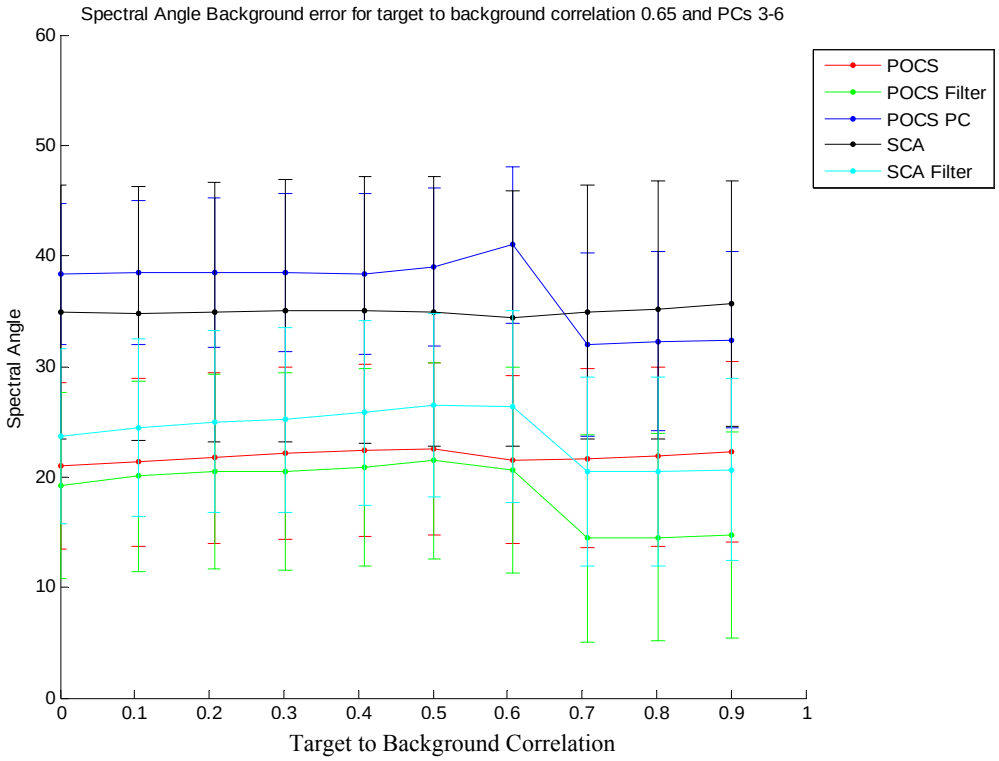

Figure B36.

1 Target

Targets

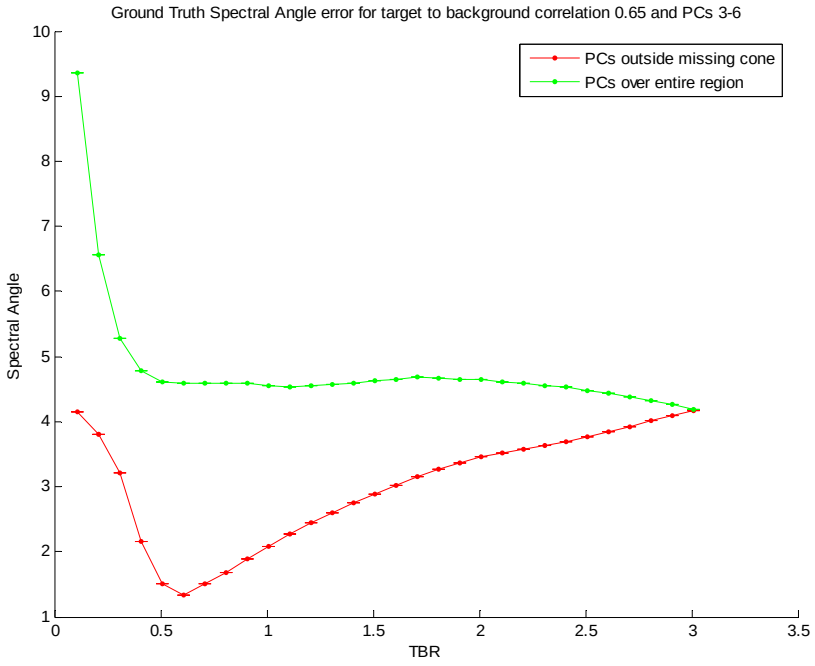

Figure B37.

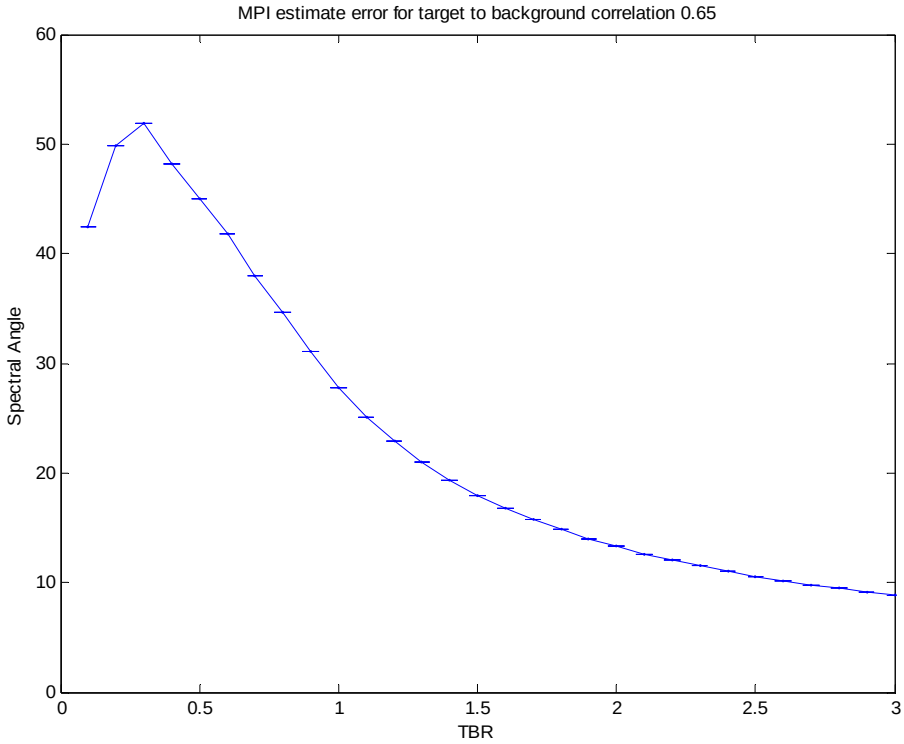

Figure B38.

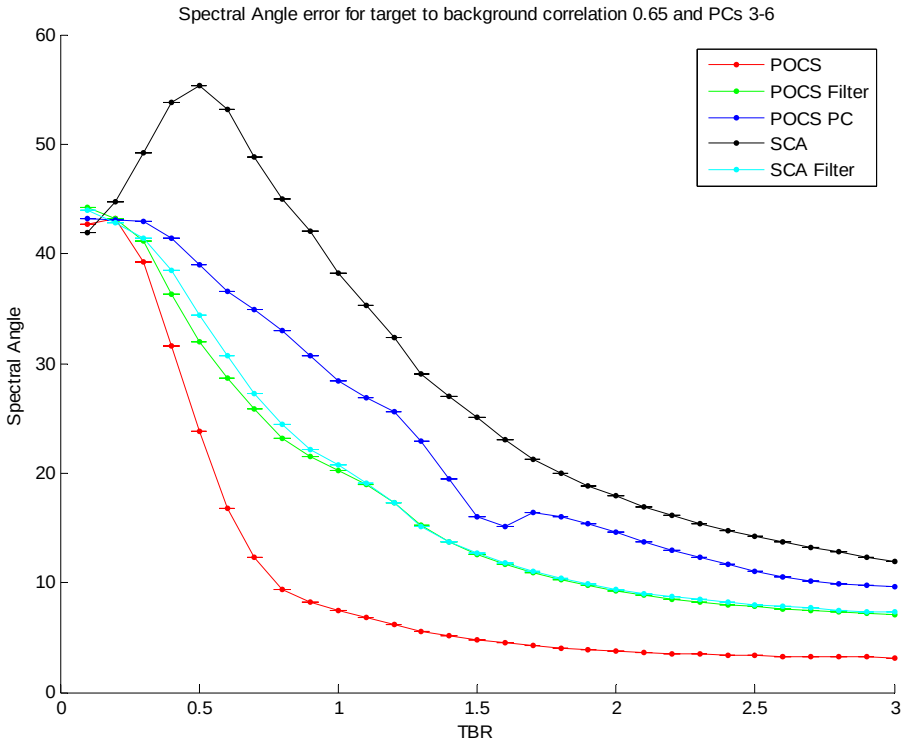

Figure B39.

Background

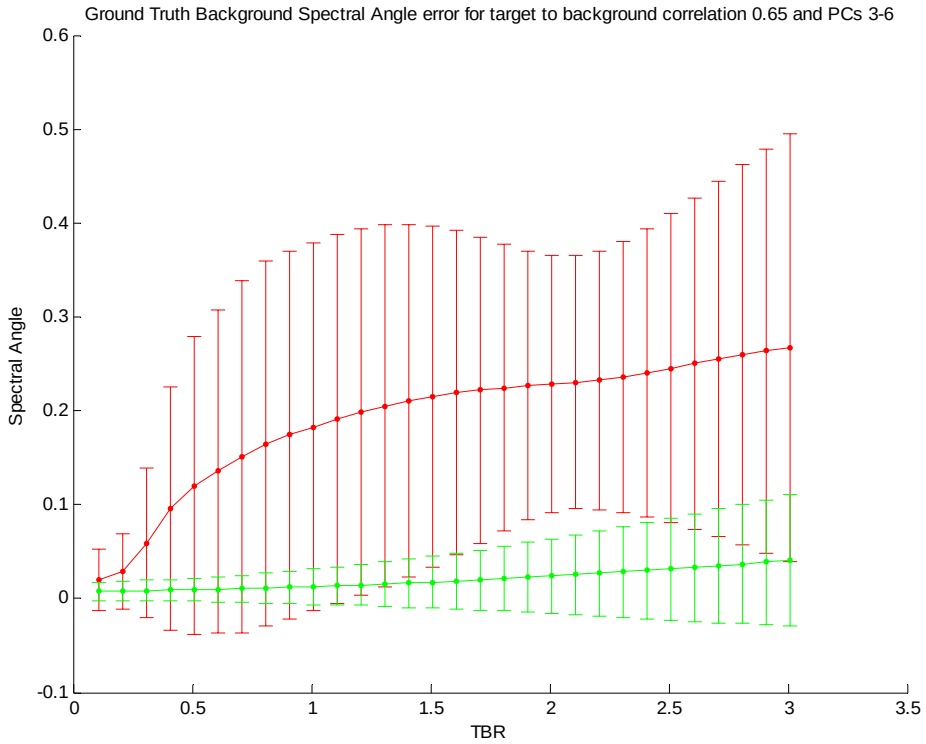

Figure B40.

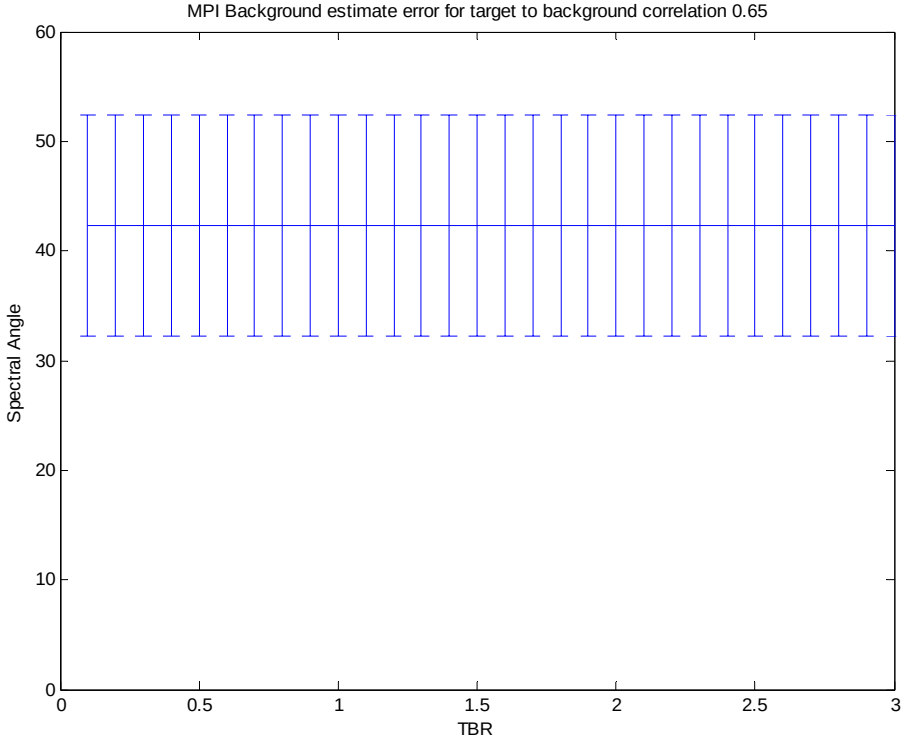

Figure B41.

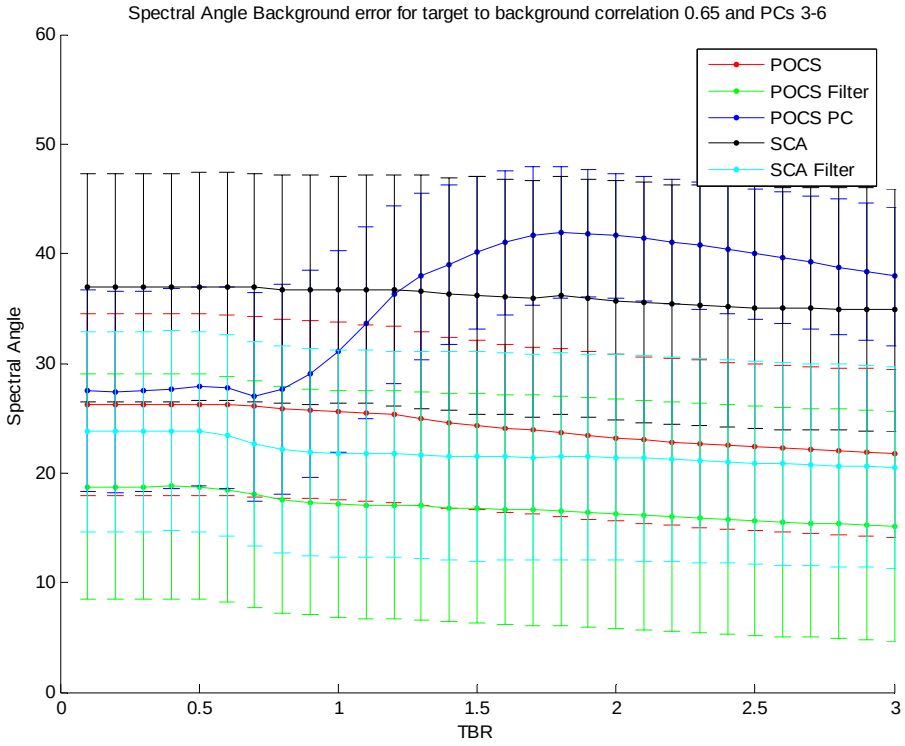
Spectral Angle Background error for target to background correlation 0.65 and PCs 3-6
POCS
POCS Filter
POCS PC
SCA
SCA Filter
Spectral Angle
TBR
0
10
20
30
40
50
60
0
0.5
1
1.5
2
2.5
3
Figure B42.

Correlation Results

Target

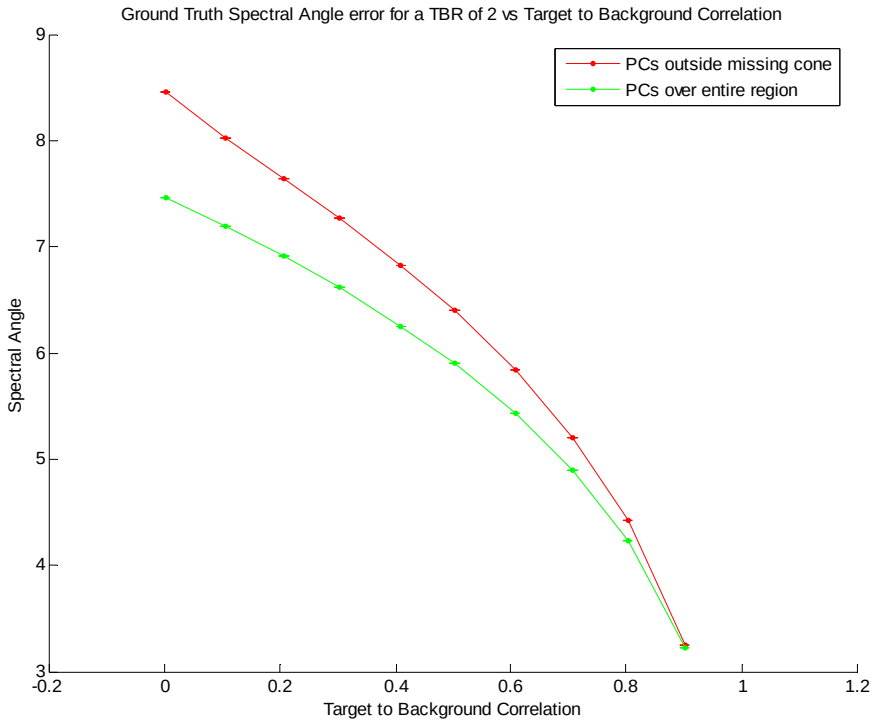

Figure B43.

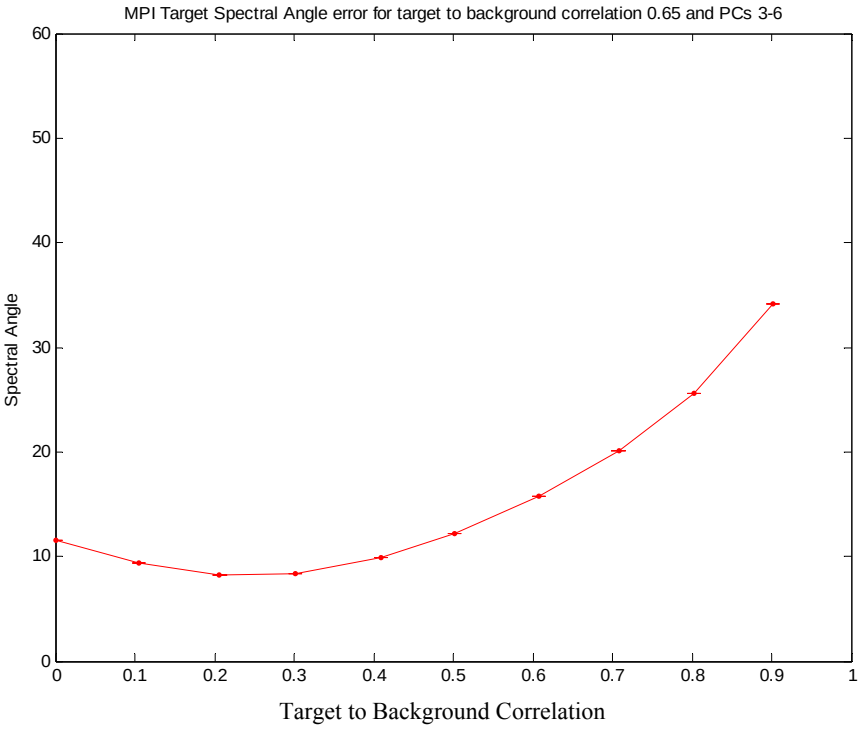

Figure B44.

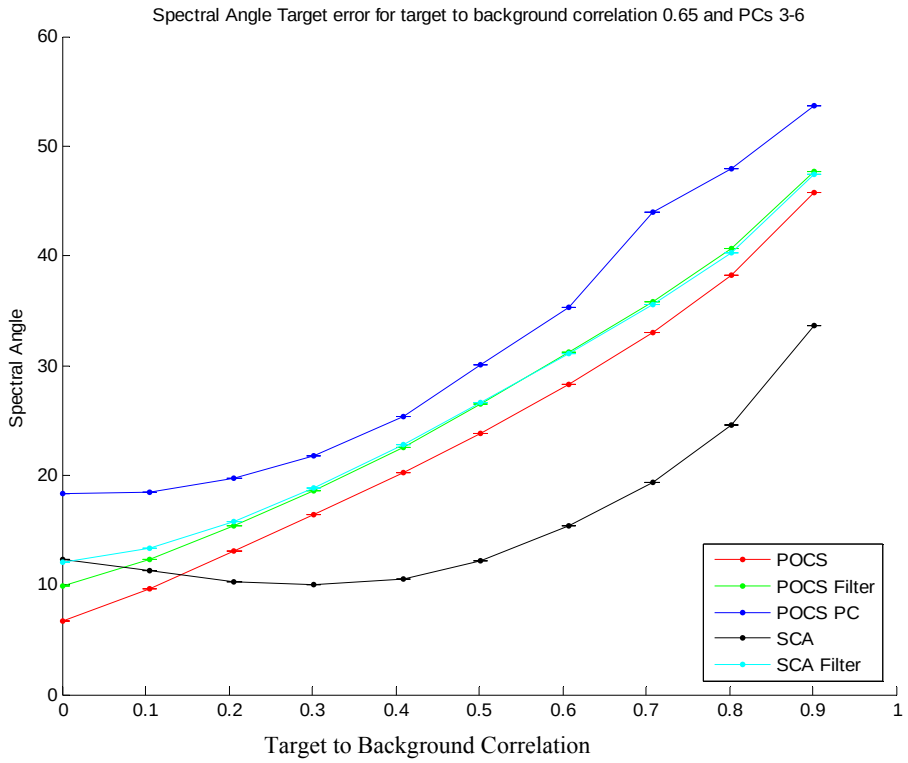

Figure B45.

Background

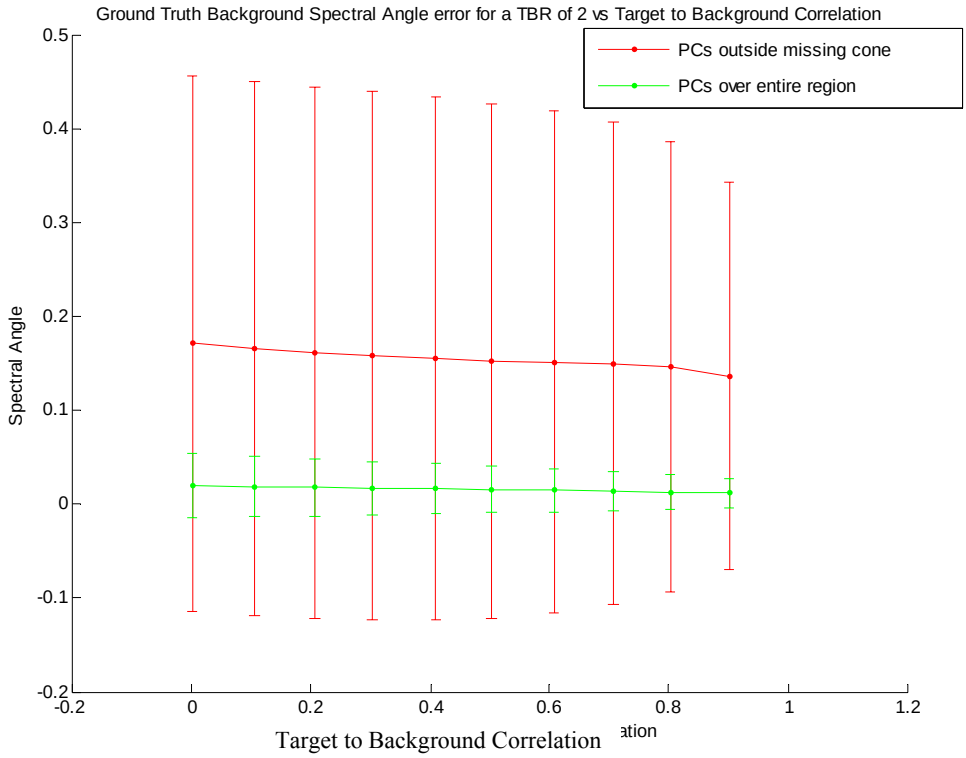

Figure B46.

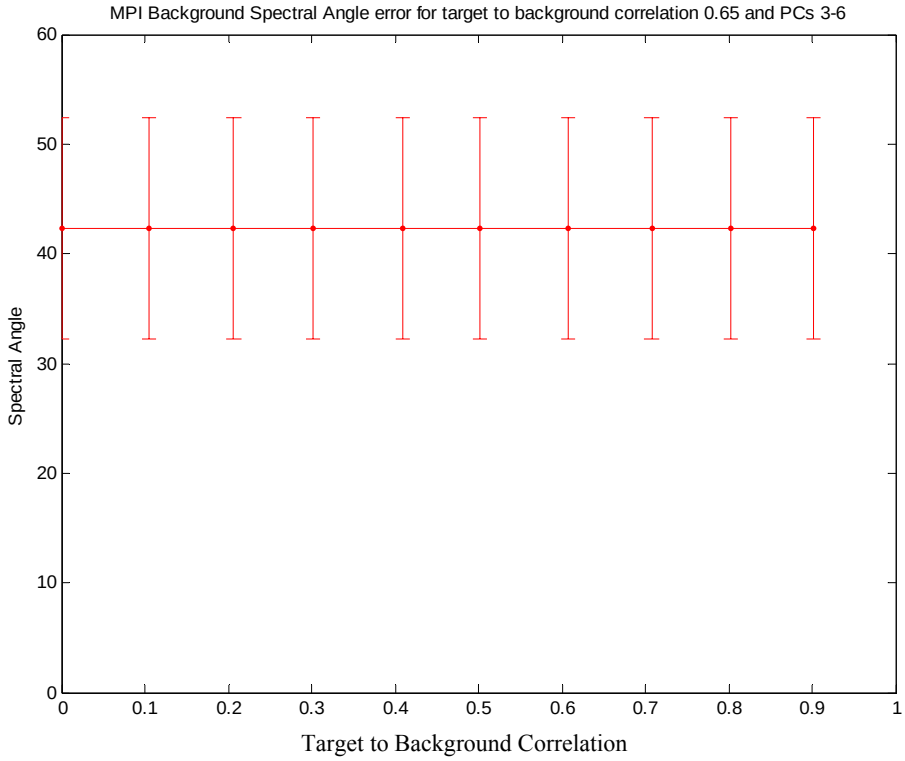

Figure B47.

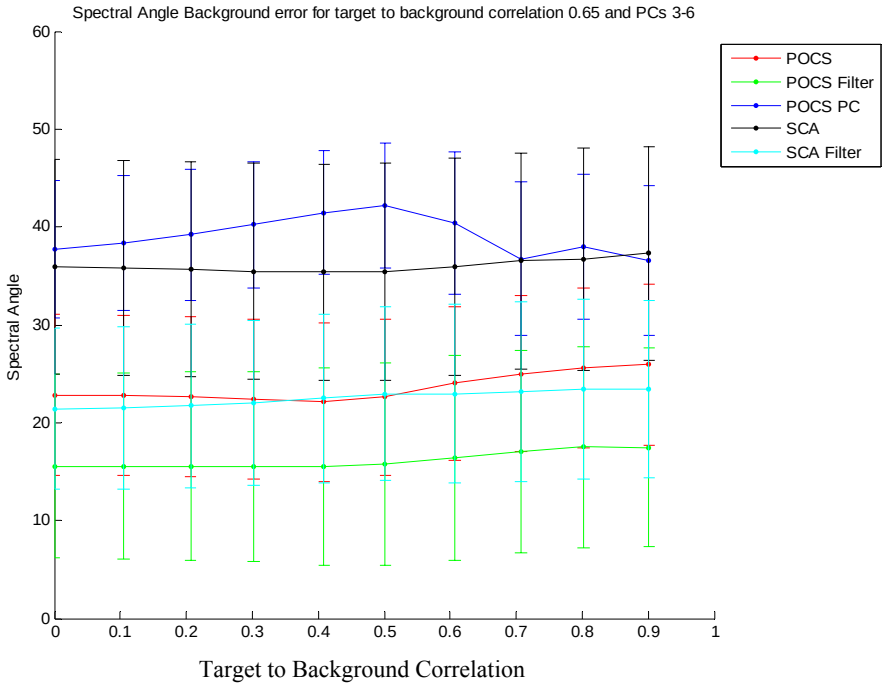

Figure B48.

Appendix C

Iran 256 x 256

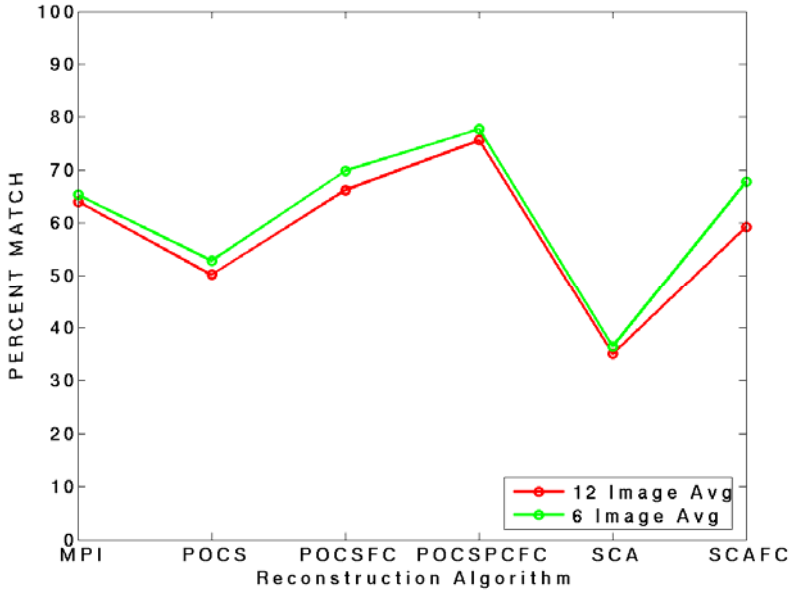

C- 1 Iran 256x256 Images, Bands 1-16, DFC Classification Algorithm, Performance Change by Average Number of Images

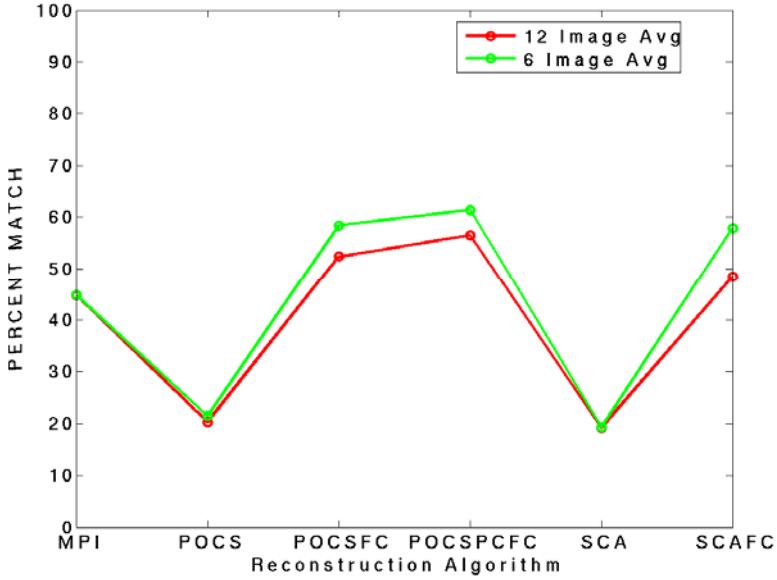

C- 2. Iran 256x256 Images, Bands 1-13 and 24-32, DFC Classification Algorithm, Performance Change by Average Number of Images

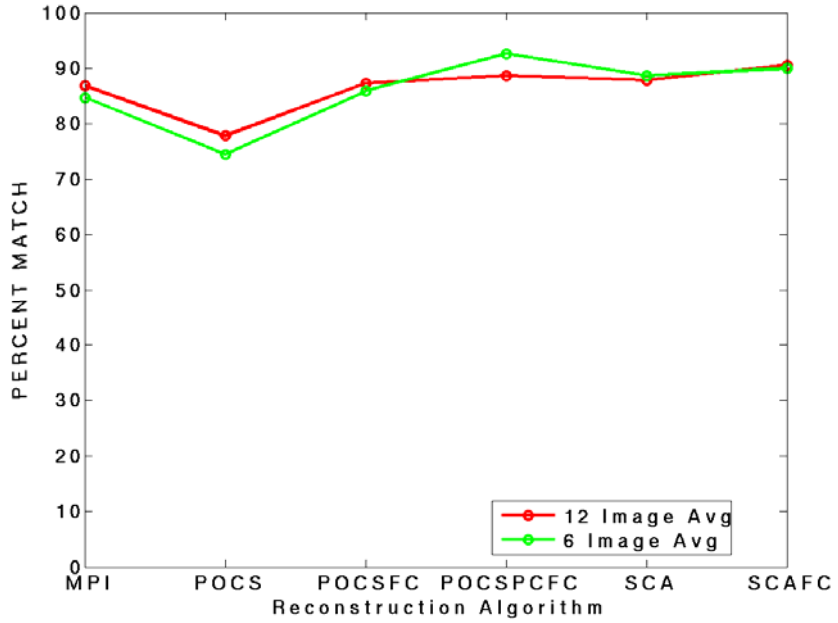

C- 3 Iran 256x256 Images, Bands 1-16, *k*-means Classification Algorithm, 3-Classes, Performance Change by Average Number of Images

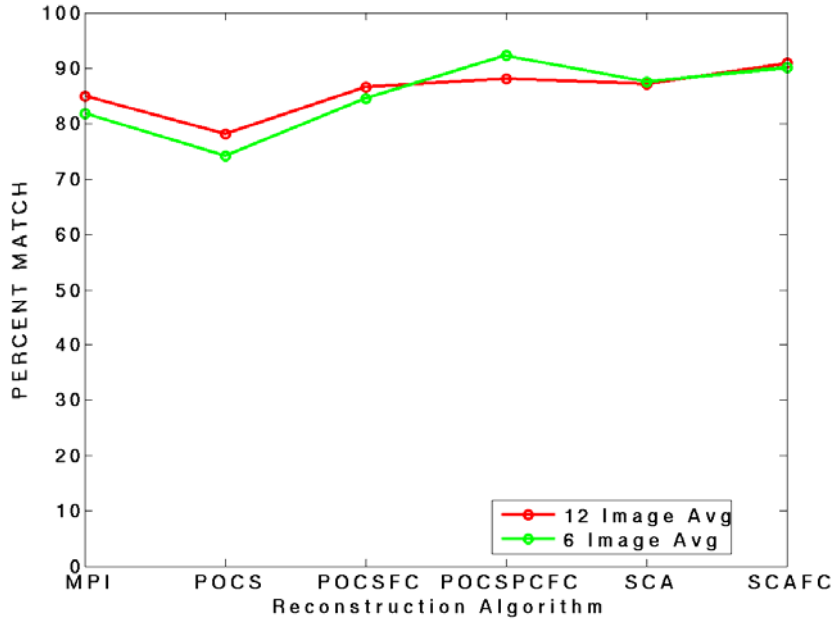

C- 4 Iran 256x256 Images, Bands 1-13 and 24-32, *k*-means Classification Algorithm, 3-Classes, Performance Change by Average Number of Images

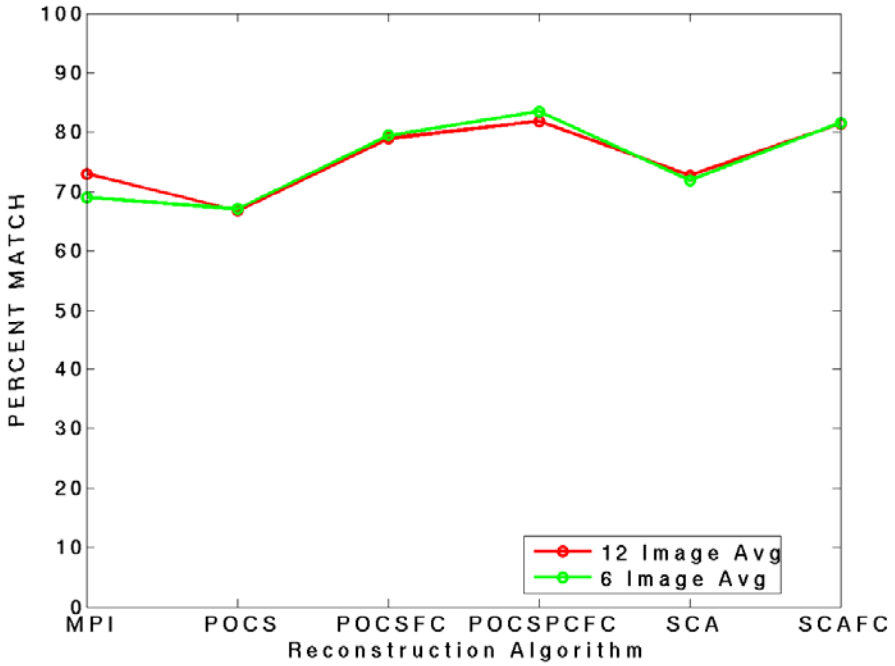

C- 5 Iran 256x256 Images, Bands 1-16, *k*-means Classification Algorithm, 6-Classes, Performance Change by Average Number of Images

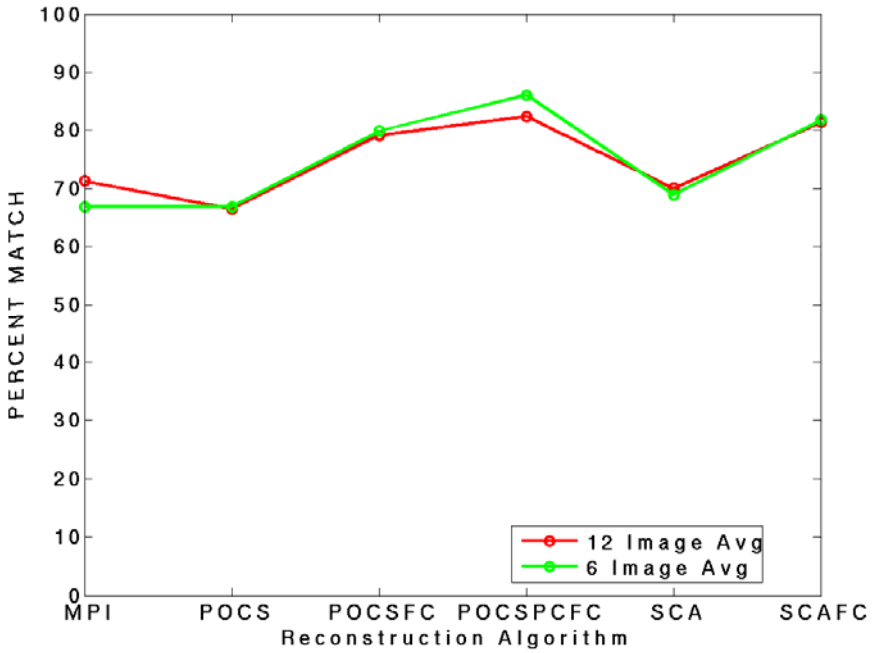

C- 6 Iran 256x256 Images, Bands: 1-13 and 24-32, *k*-means Classification Algorithm, 6-Classes, Performance Change by Average Number of Images

Iran 512x512

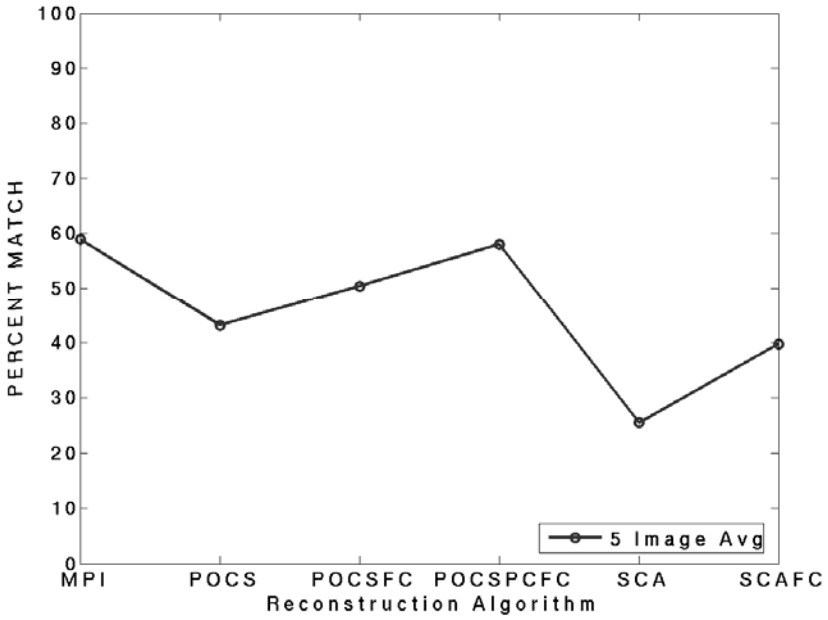

C- 7 Iran 512x512 Images, Bands 1-16, DFC Classification Algorithm, Performance Change Over Average of All Images

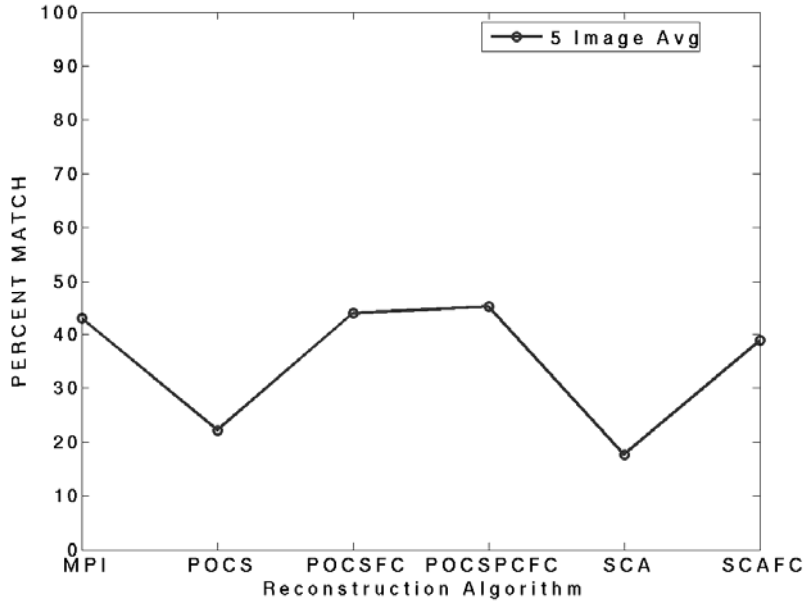

C- 8 Iran 512x512 Images, Bands 1-13 and 24-32, DFC Classification Algorithm, Performance Change Over Average of All Images

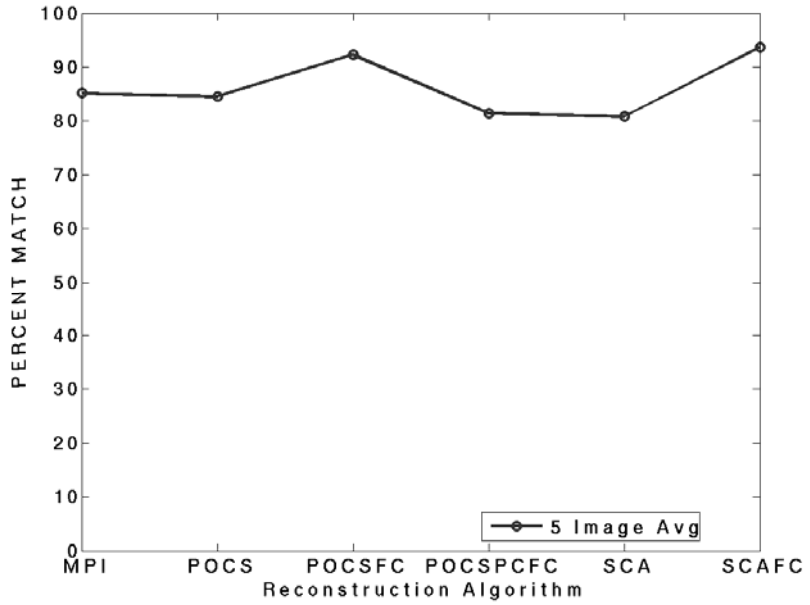

C- 9 Iran 512x512 Images, Bands 1-16, *k*-means Classification Algorithm, 3-Classes, Performance Change Over Average of All Images

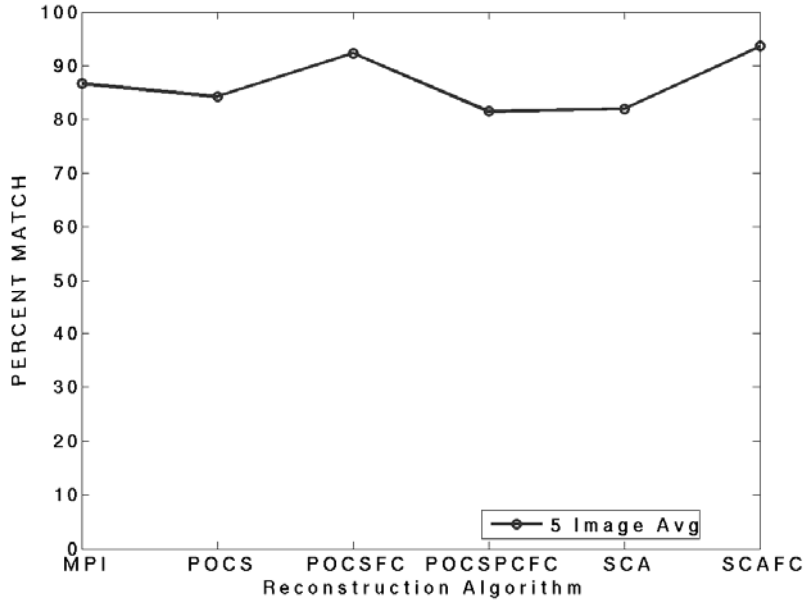

C- 10 Iran 512x512 Images, Bands 1-13 and 24-32, *k*-means Classification Algorithm, 3-Classes, Performance Change Over Average of All Images

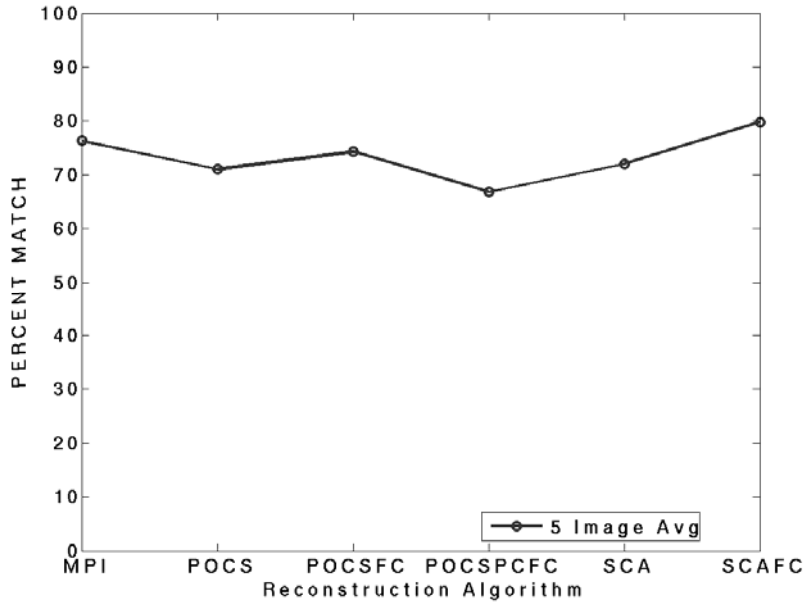

C- 11 Iran 512x512 Images, Bands 1-16, *k*-means Classification Algorithm, 6-Classes, Performance Change Over Average of All Images

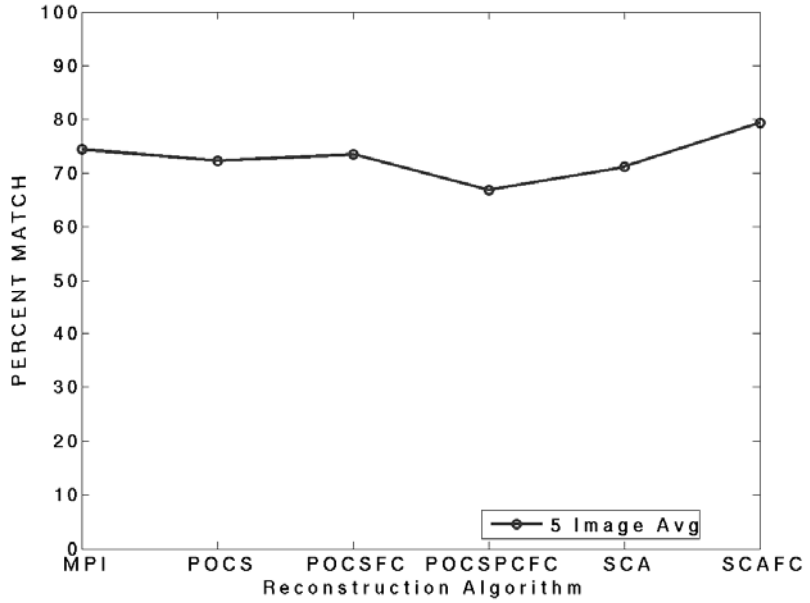

C- 12 Iran 512x512 Images, Bands: 1-13 and 24-32, *k*-means Classification Algorithm, 6-Classes, Performance Change Over Average of All Images

Israel 256x256

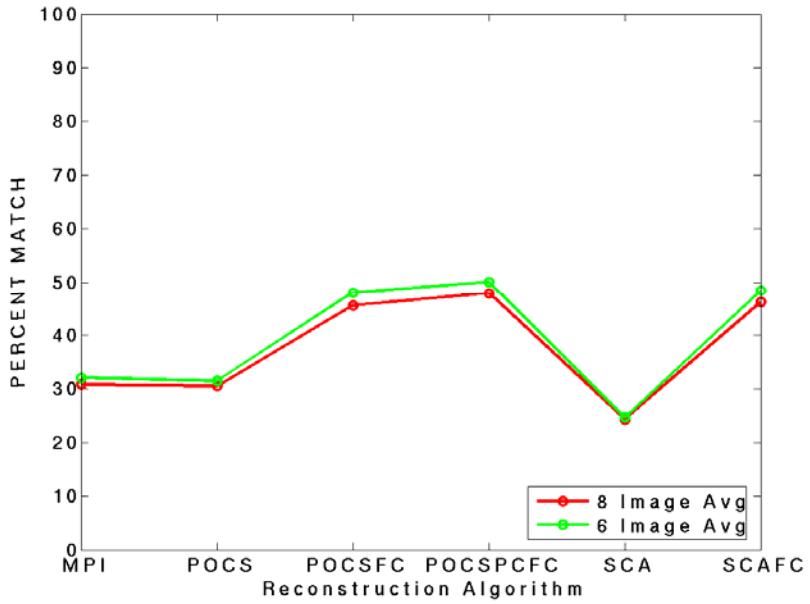

C- 13 Israel 256x256 Images, Bands 1-16, DFC Classification Algorithm, Performance Change by Average Number of Images

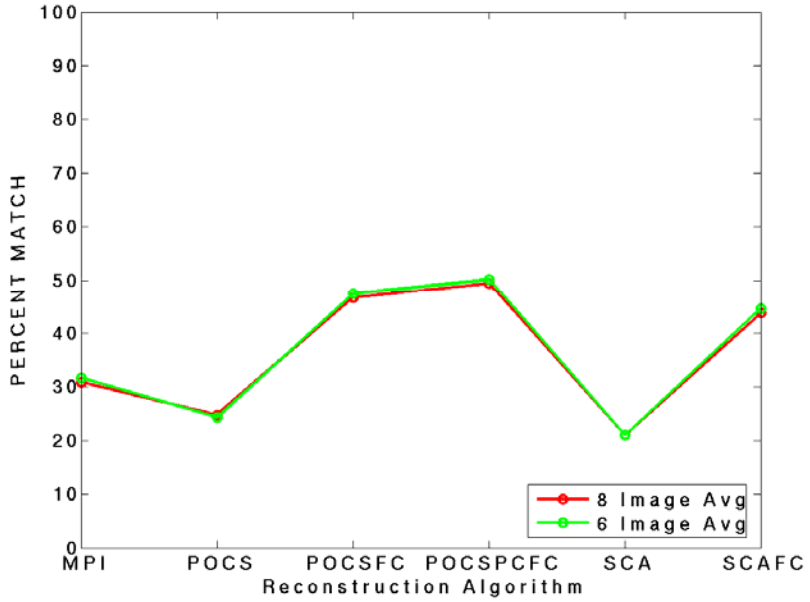

C- 14 Israel 256x256 Images, Bands 1-13 and 24-32, DFC Classification Algorithm, Performance Change by Average Number of Images

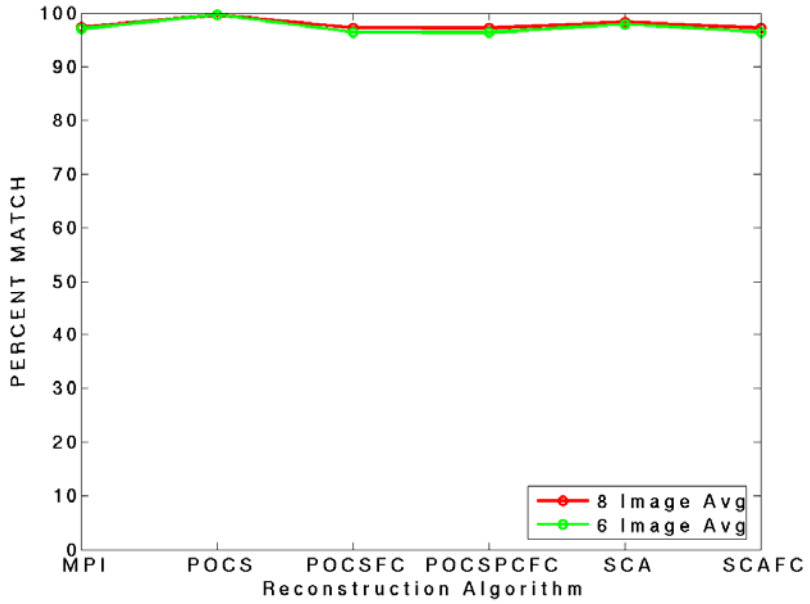

C- 15 Israel 256x256 Images, Bands 1-16, *k*-means Classification Algorithm, 3-Classes, Performance Change by Average Number of Images

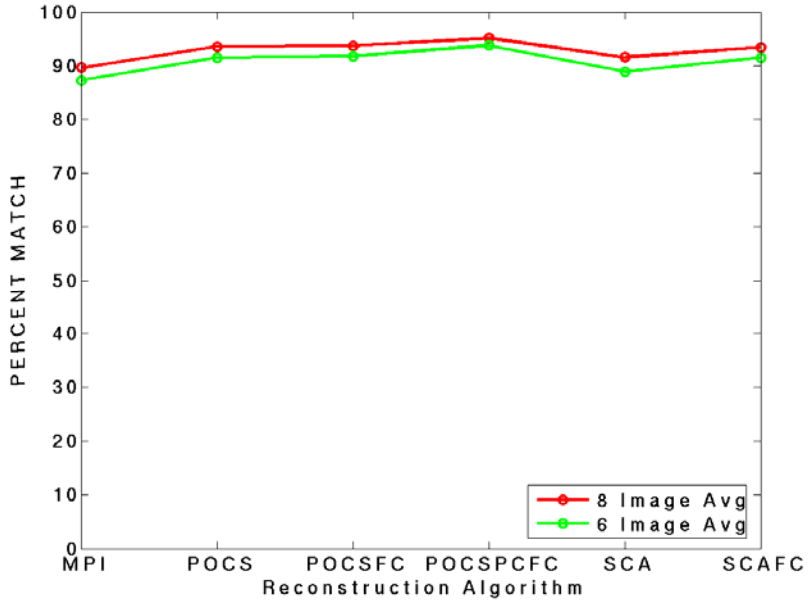

C- 16 Israel 256x256 Images, Bands 1-13 and 24-32, *k*-means Classification Algorithm, 3-Classes, Performance Change by Average Number of Images

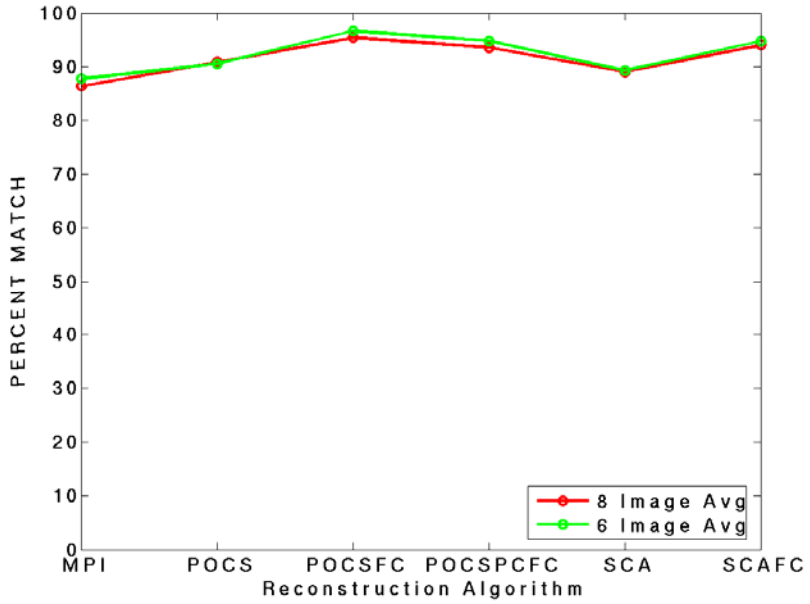

C- 17 Israel 256x256 Images, Bands 1-16, *k*-means Classification Algorithm, 6-Classes, Performance Change by Average Number of Images

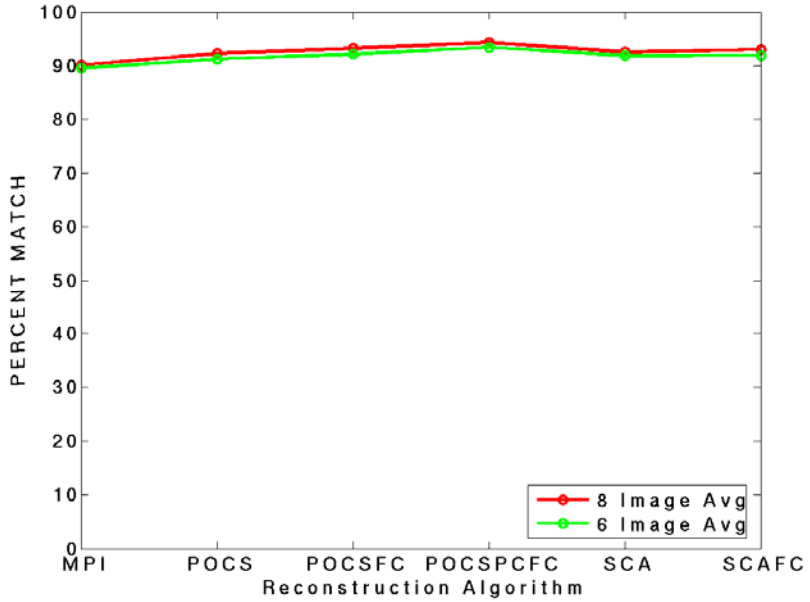

C- 18 Israel 256x256 Images, Bands 1-13 and 24-32, *k*-means Classification Algorithm, 6-Classes, Performance Change by Average Number of Images

Performance Change by Number of Principal Component Constraints

Iran 256x256

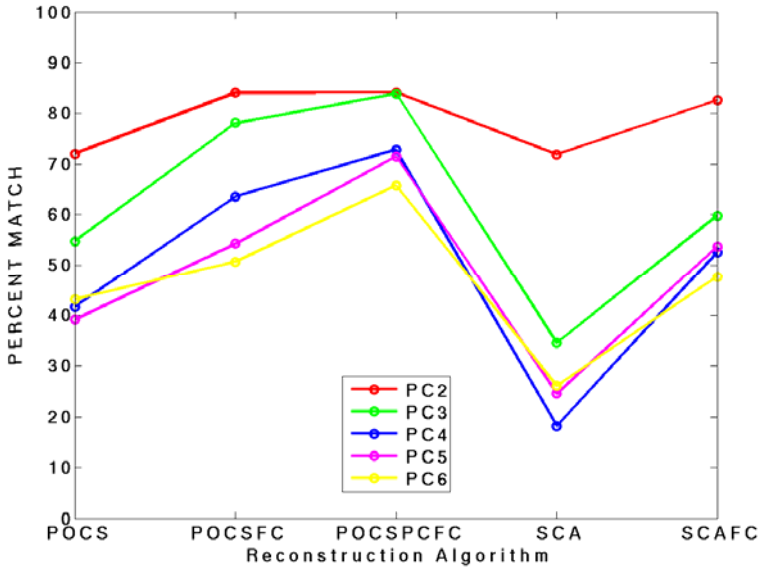

C- 19 Iran 256x256 Images, Bands 1-16, DFC Classification Algorithm, Performance Change by Number of Principal Component Constraints

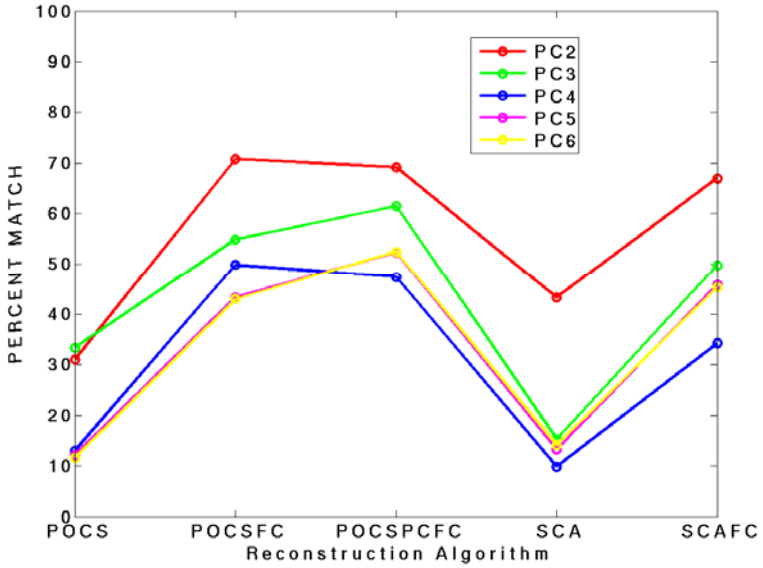

C- 20 Iran 256x256 Images, Bands 1-13 and 24-32, DFC Classification Algorithm, Performance Change by Number of Principal Component Constraints

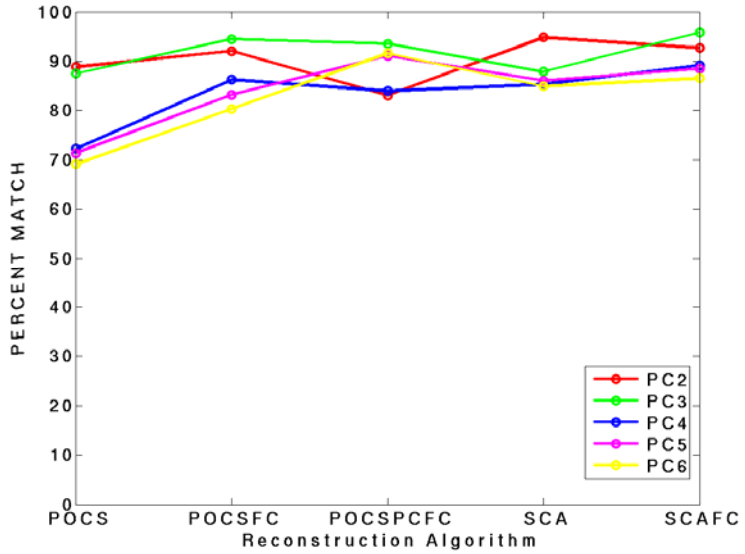

C- 21 Iran 256x256 Images, Bands 1-16, *k*-means Classification Algorithm, 3-Classes, Performance Change by Number of Principal Component Constraints

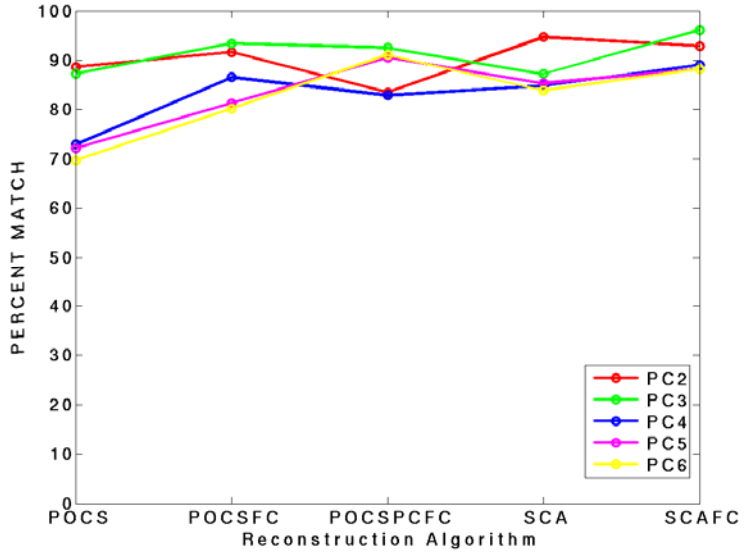

C- 22 Iran 256x256 Images, Bands 1-13 and 24-32, *k*-means Classification Algorithm, 3-Classes, Performance Change by Number of Principal Component Constraints

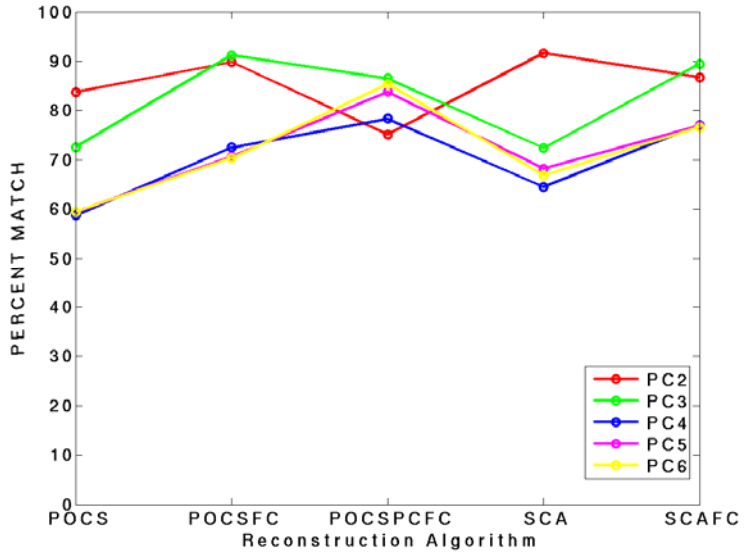

C- 23 Iran 256x256 Images, Bands 1-16, *k*-means Classification Algorithm, 6-Classes, Performance Change by Number of Principal Component Constraints

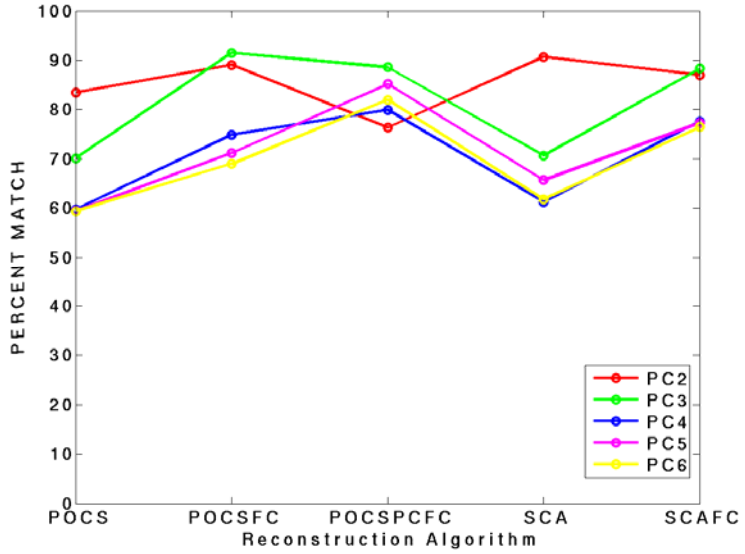

C- 24 Iran 256x256 Images, Bands: 1-13 and 24-32, *k*-means Classification Algorithm, 6-Classes, Performance Change by Number of Principal Component Constraints

Iran 512x512

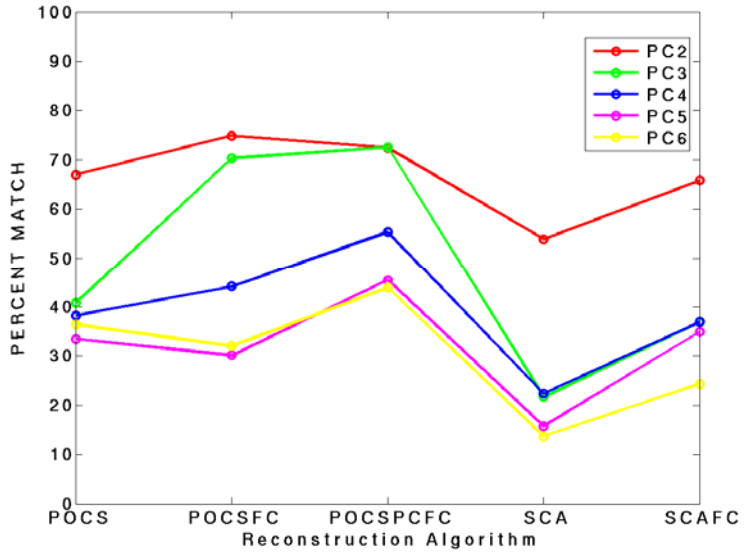

C- 25 Iran 512x512 Images, Bands 1-16, DFC Classification Algorithm, Performance Change by Number of Principal Component Constraints

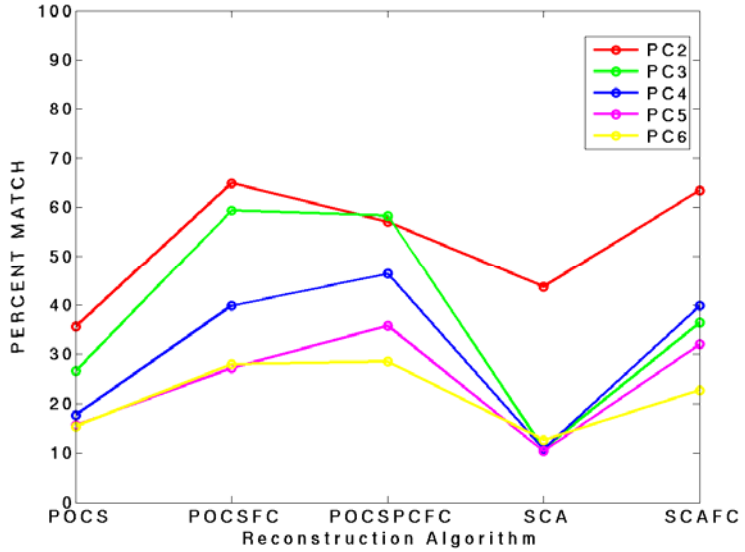

C- 26 Iran 512x512 Images, Bands 1-13 and 24-32, DFC Classification Algorithm, Performance Change by Number of Principal Component Constraints

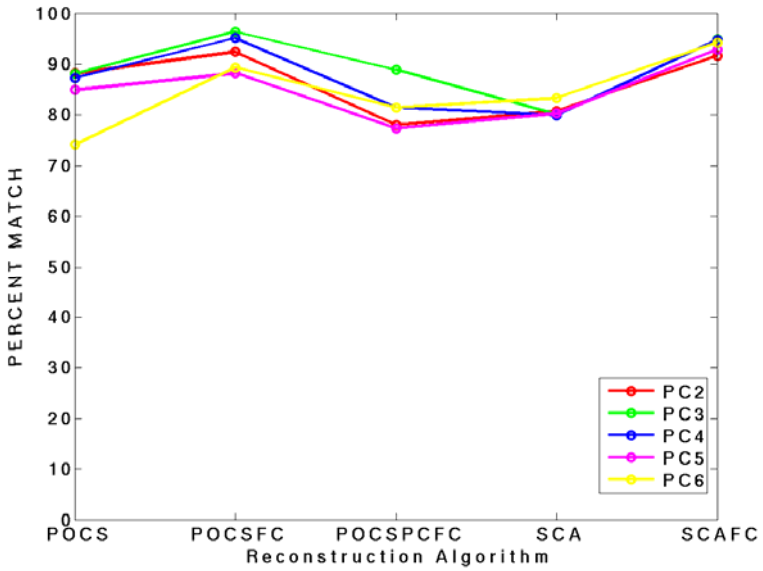

C- 27 Iran 512x512 Images, Bands 1-16, *k*-means Classification Algorithm, 3-Classes, Performance Change by Number of Principal Component Constraints

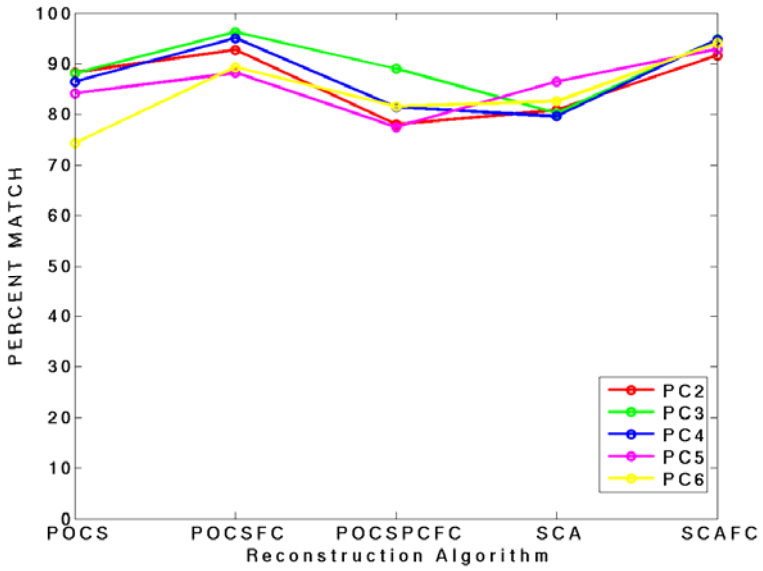

C- 28 Iran 512x512 Images, Bands 1-13 and 24-32, *k*-means Classification Algorithm, 3-Classes, Performance Change by Number of Principal Component Constraints

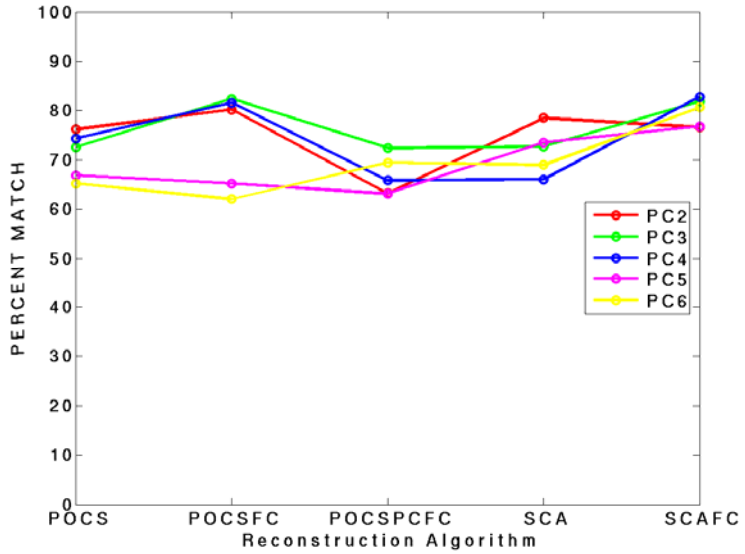

C- 29 Iran 512x512 Images, Bands 1-16, *k*-means Classification Algorithm, 6-Classes, Performance Change by Number of Principal Component Constraints

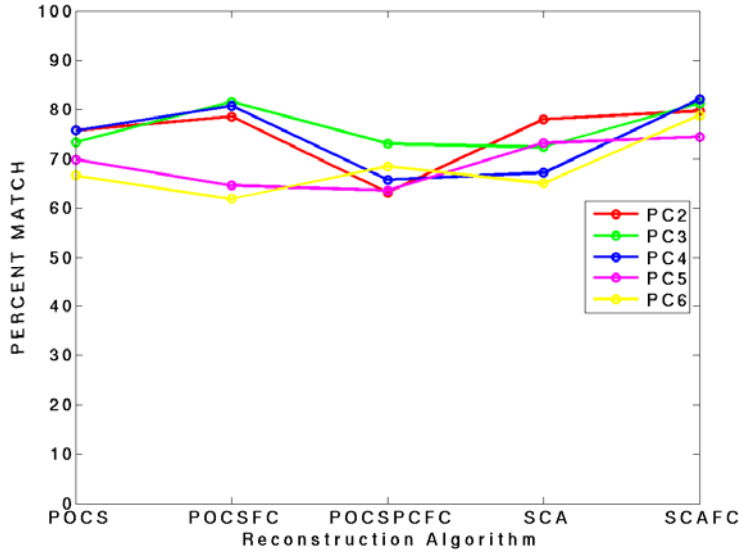

C- 30 Iran 512x512 Images, Bands: 1-13 and 24-32, *k*-means Classification Algorithm, 6-Classes, Performance Change by Number of Principal Component Constraints

Israel 256x256

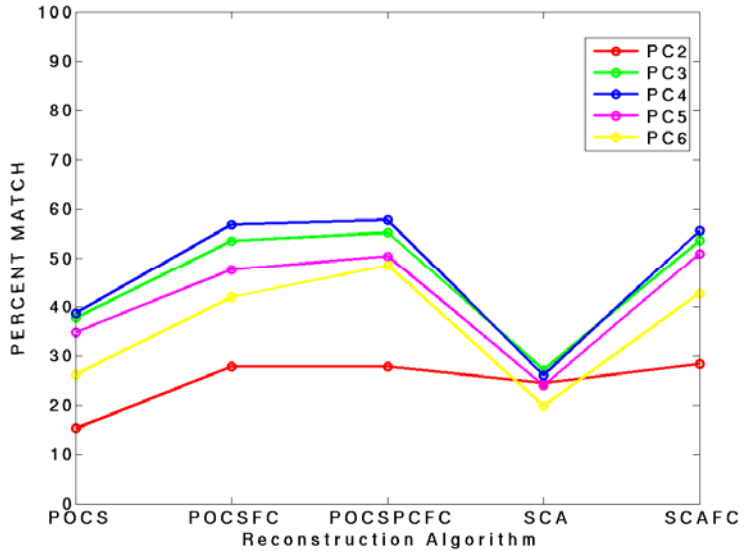

C- 31 Israel 256x256 Images, Bands 1-16, DFC Classification Algorithm, Performance Change by Number of Principal Component Constraints

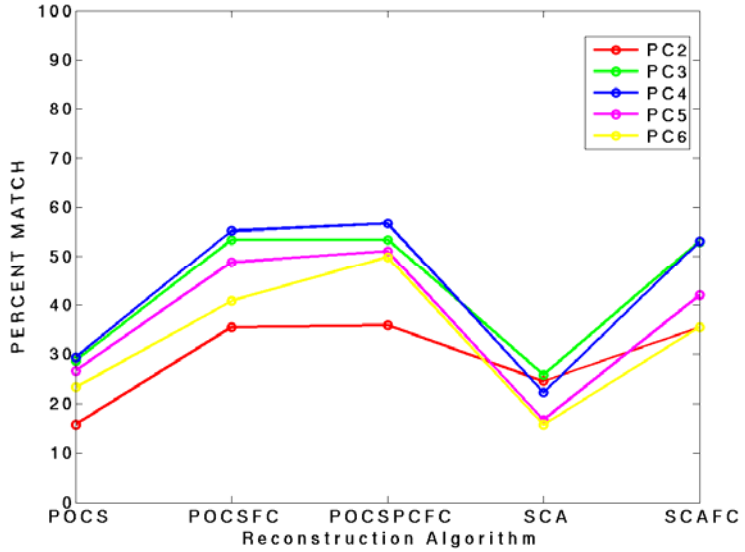

C- 32 Israel 256x256 Images, Bands 1-13 and 24-32, DFC Classification Algorithm, Performance Change by Number of Principal Component Constraints

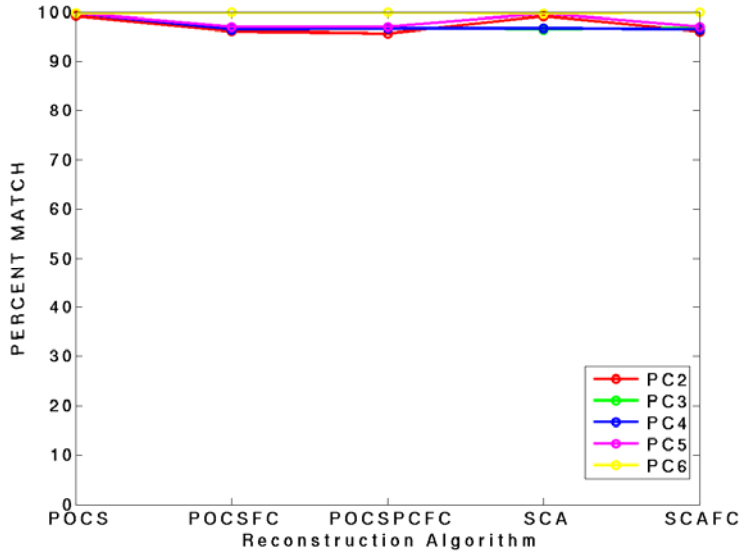

C- 33 Israel 256x256 Images, Bands 1-16, *k*-means Classification Algorithm, 3-Classes, Performance Change by Number of Principal Component Constraints

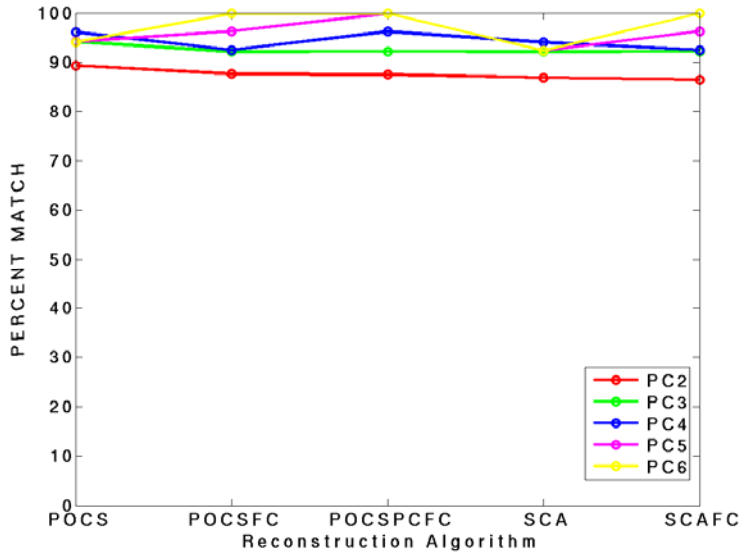

C- 34 Israel 256x256 Images, Bands 1-13 and 24-32, *k*-means Classification Algorithm, 3-Classes, Performance Change by Number of Principal Component Constraints

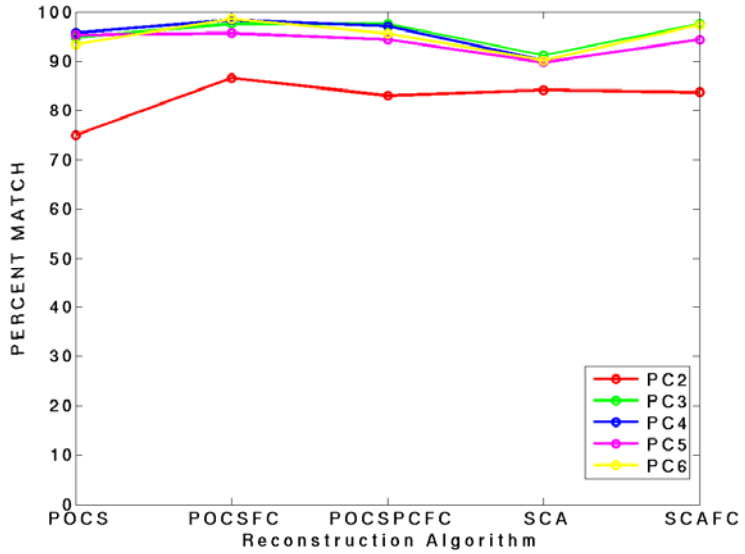

C- 35 Israel 256x256 Images, Bands 1-16, *k*-means Classification Algorithm, 6-Classes, Performance Change by Number of Principal Component Constraints

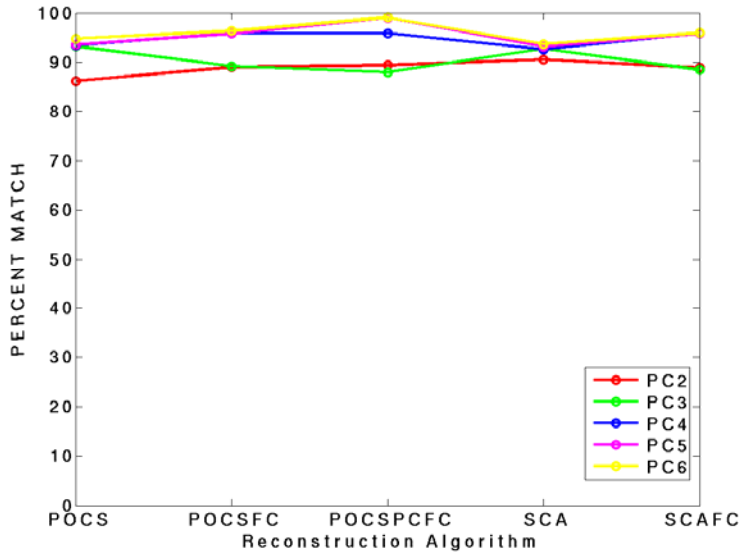

C- 36 Israel 256x256 Images, Bands 1-13 and 24-32, *k*-means Classification Algorithm, 6-Classes, Performance Change by Number of Principal Component Constraints

SNR Sensitivity Analysis

Iran 256x256

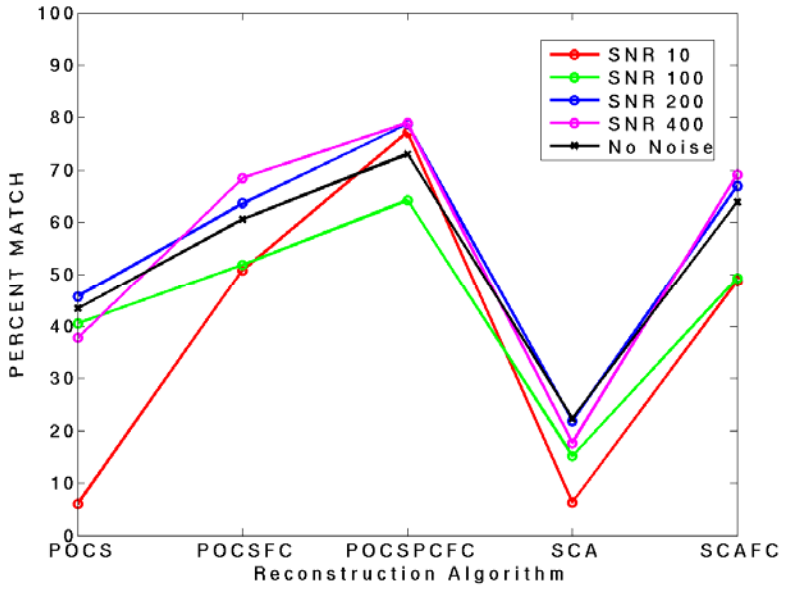

C- 37 Iran 256x256 Images, Bands 1-16, DFC Classification Algorithm, Signal to Noise Ratio (SNR) Analysis

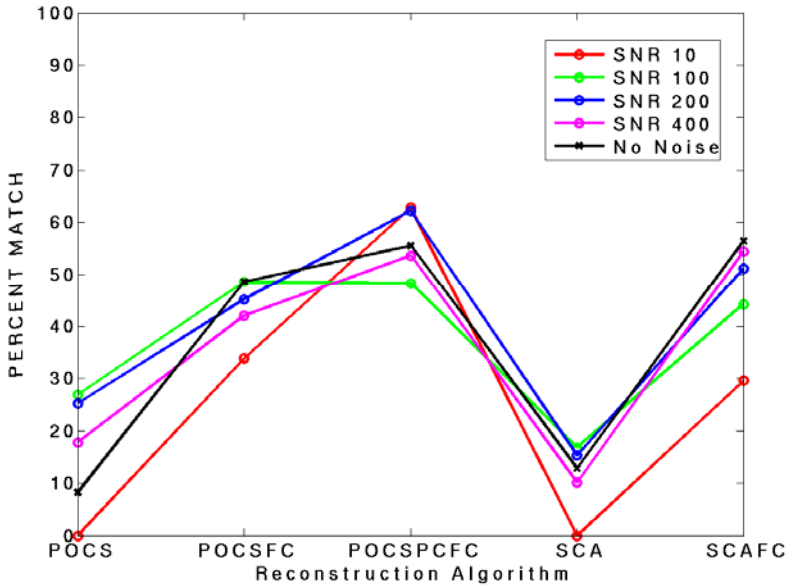

C- 38 Iran 256x256 Images, Bands 1-13 and 24-32, DFC Classification Algorithm, Signal to Noise Ratio (SNR) Analysis

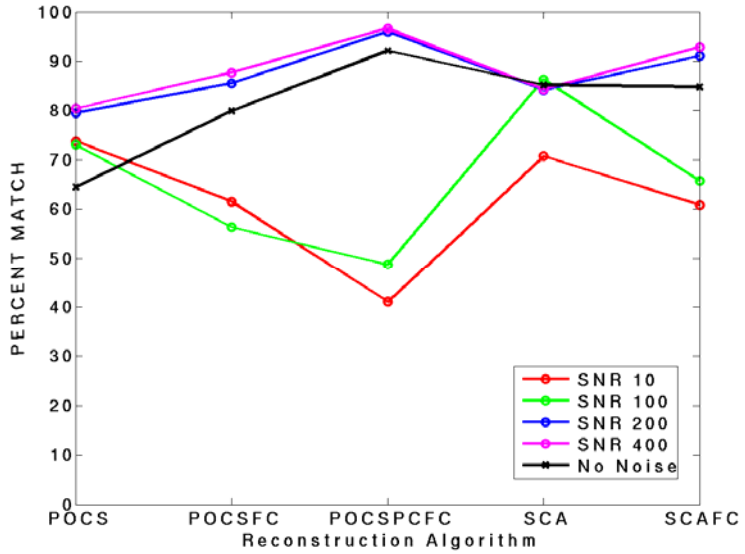

C- 39 Iran 256x256 Images, Bands 1-16, *k*-means Classification Algorithm, 3-Classes, Signal to Noise Ratio (SNR) Analysis

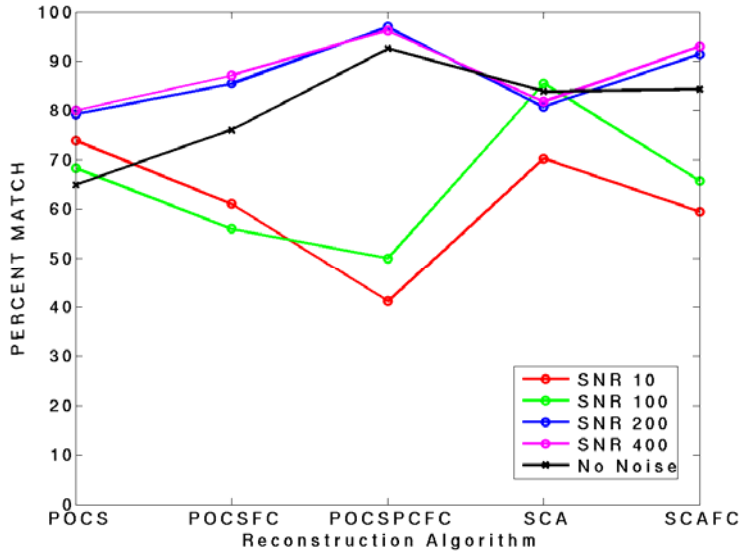

C- 40 Iran 256x256 Images, Bands 1-13 and 24-32, *k*-means Classification Algorithm, 3-Classes, Signal to Noise Ratio (SNR) Analysis

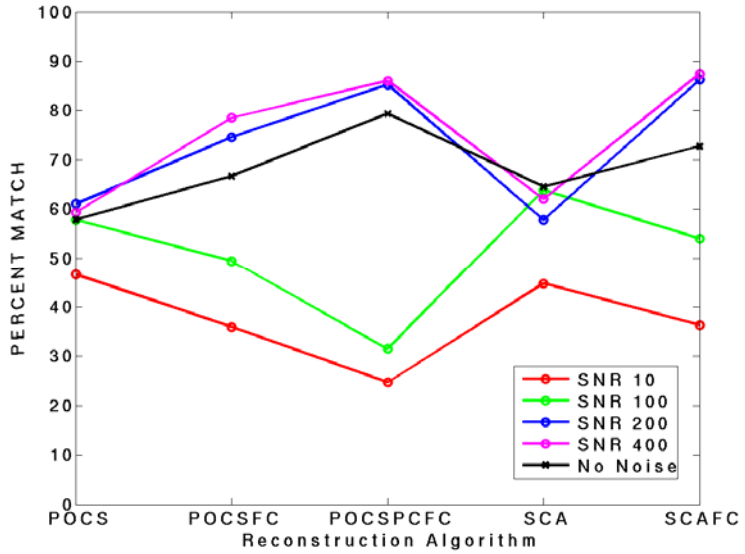

C- 41 Iran 256x256 Images, Bands 1-16, *k*-means Classification Algorithm, 6-Classes, Signal to Noise Ratio (SNR) Analysis

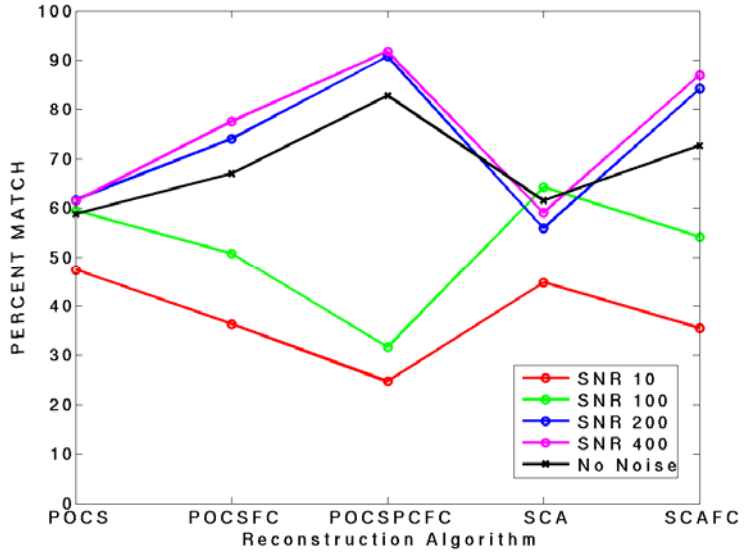

C- 42 Iran 256x256 Images, Bands: 1-13 and 24-32, *k*-means Classification Algorithm, 6-Classes, Signal to Noise Ratio (SNR) Analysis

Israel 256x256

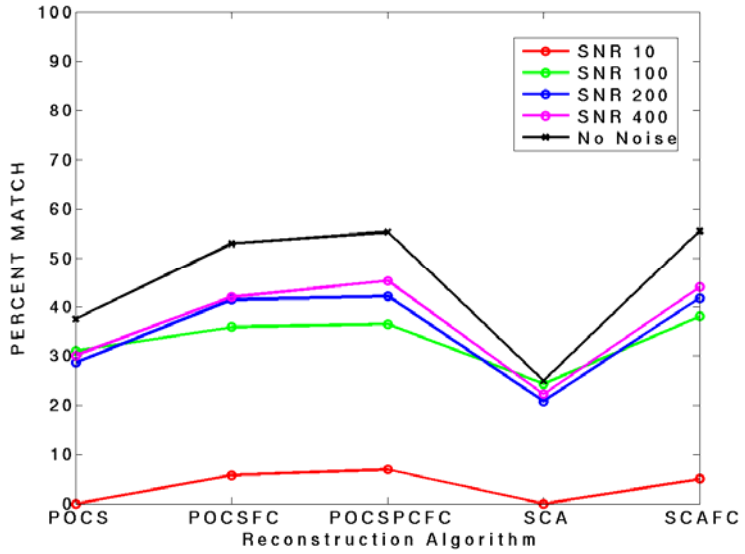

C- 43 Israel 256x256 Images, Bands 1-16, DFC Classification Algorithm, Signal to Noise Ratio (SNR) Analysis

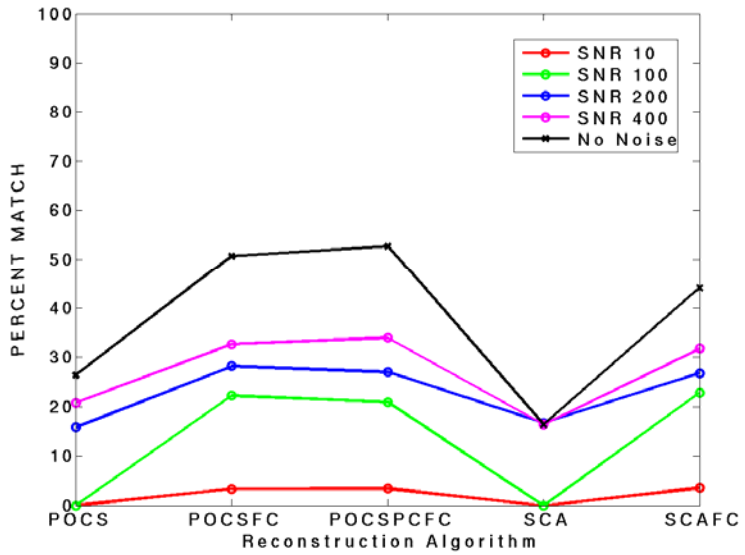

C- 44 Israel 256x256 Images, Bands 1-13 and 24-32, DFC Classification Algorithm, Signal to Noise Ratio (SNR) Analysis

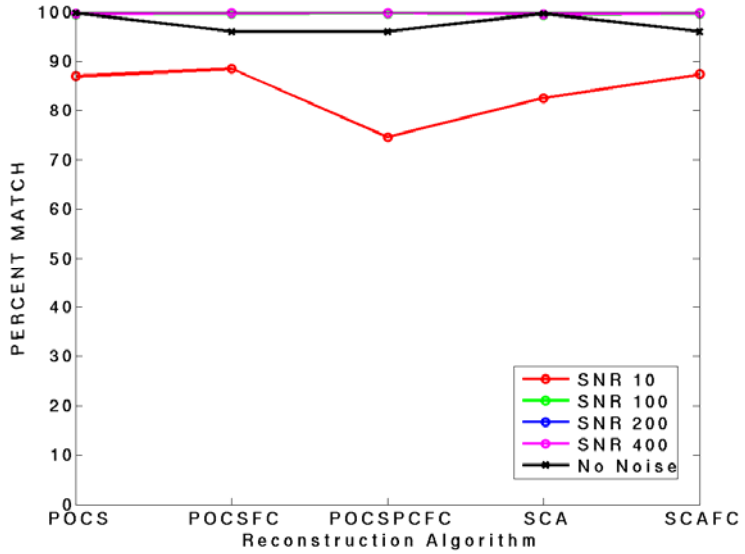

C- 45 Israel 256x256 Images, Bands 1-16, *k*-means Classification Algorithm, 3-Classes, Signal to Noise Ratio (SNR) Analysis

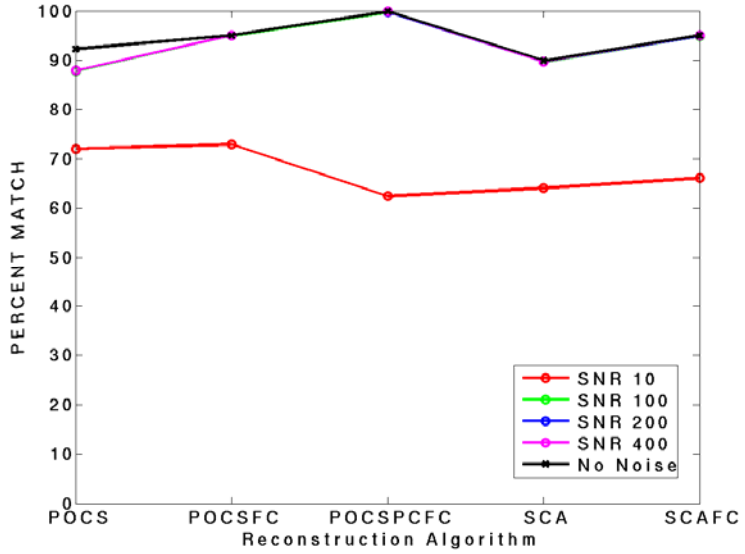

C- 46 Israel 256x256 Images, Bands 1-13 and 24-32, *k*-means Classification Algorithm, 3-Classes, Signal to Noise Ratio (SNR) Analysis

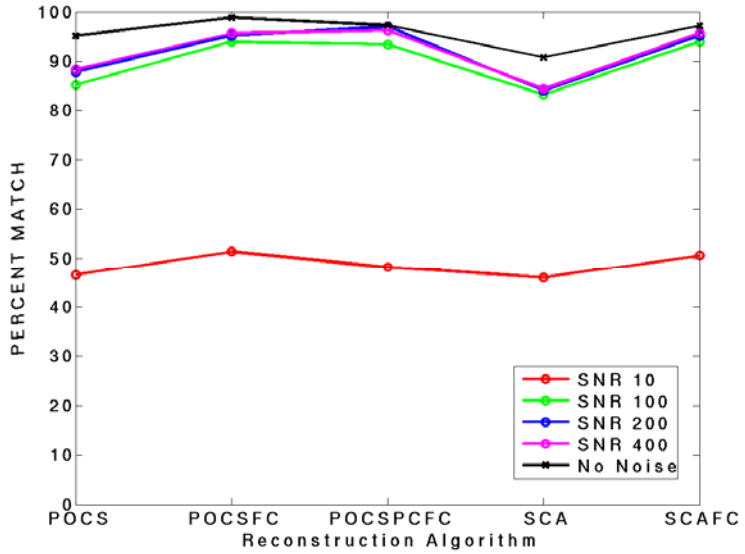

C- 47 Israel 256x256 Images, Bands 1-16, *k*-means Classification Algorithm, 6-Classes, Signal to Noise Ratio (SNR) Analysis

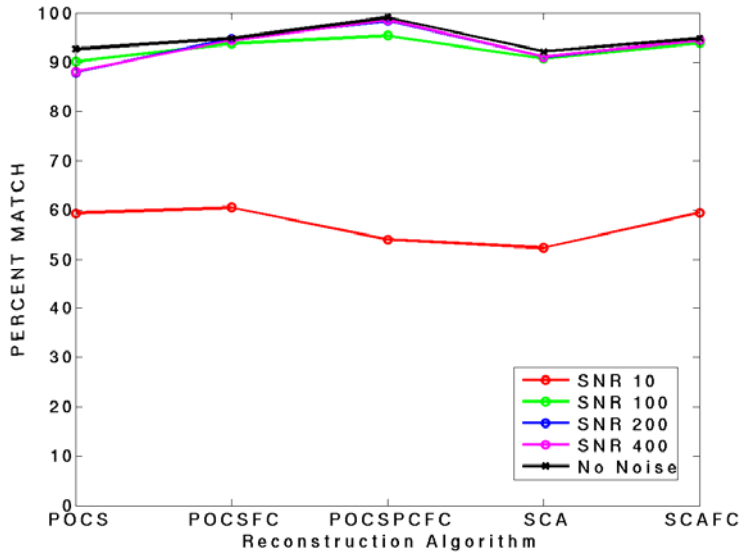

C- 48 Israel 256x256 Images, Bands 1-13 and 24-32, *k*-means Classification Algorithm, 6-Classes, Signal to Noise Ratio (SNR) Analysis

Jitter Sensitivity Analysis

Iran 256x256

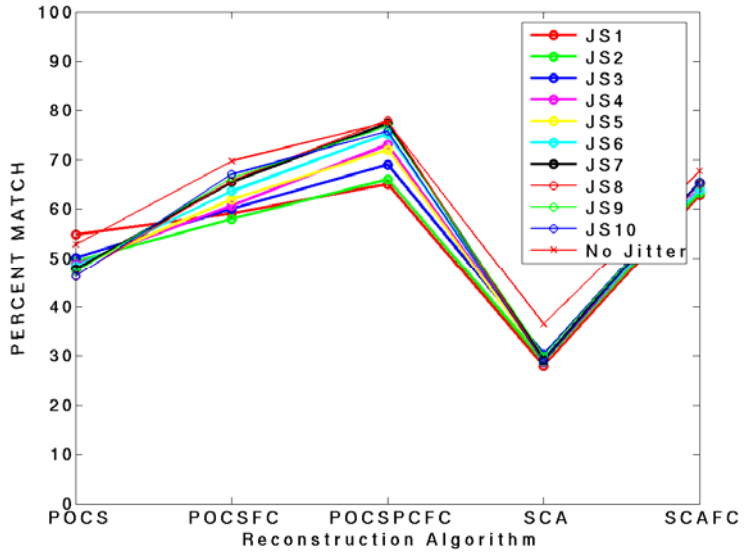

C- 49 Iran 256x256 Images, Bands 1-16, DFC Classification Algorithm, Jitter Analysis

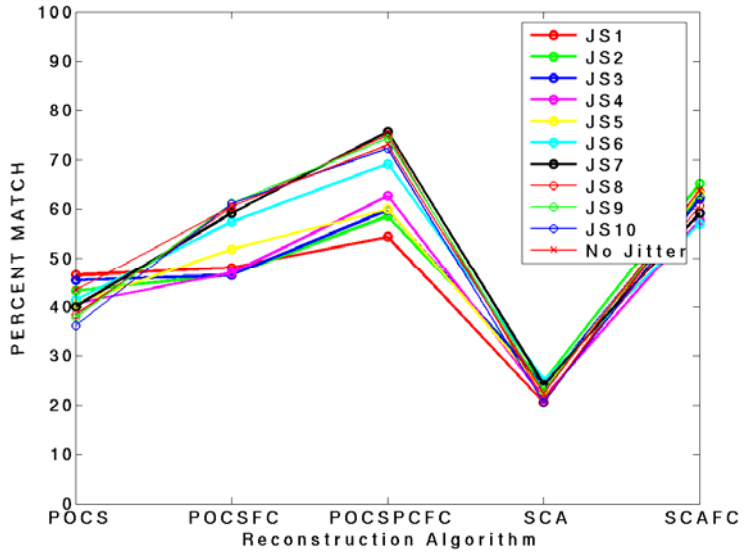

C- 50 Iran 256x256 Images, Bands 1-16, DFC Classification Algorithm, 5 Principal Component Constraint, Jitter Analysis

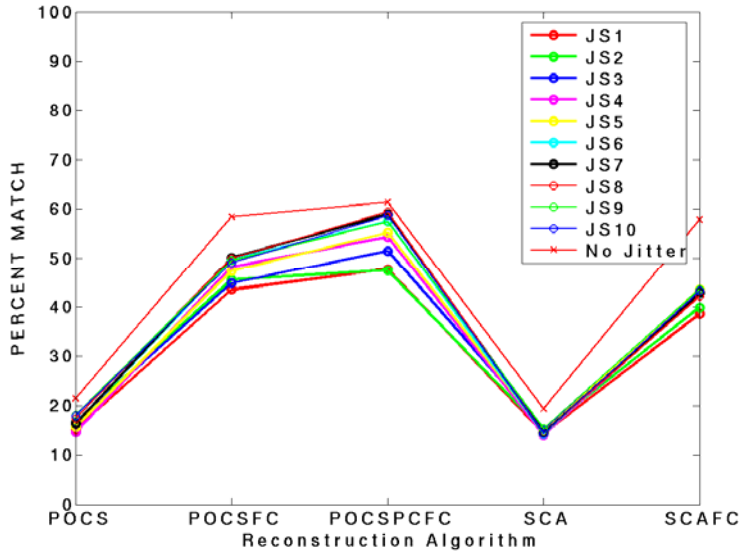

C- 51 Iran 256x256 Images, Bands 1-13 and 24-32, DFC Classification Algorithm, Jitter Analysis

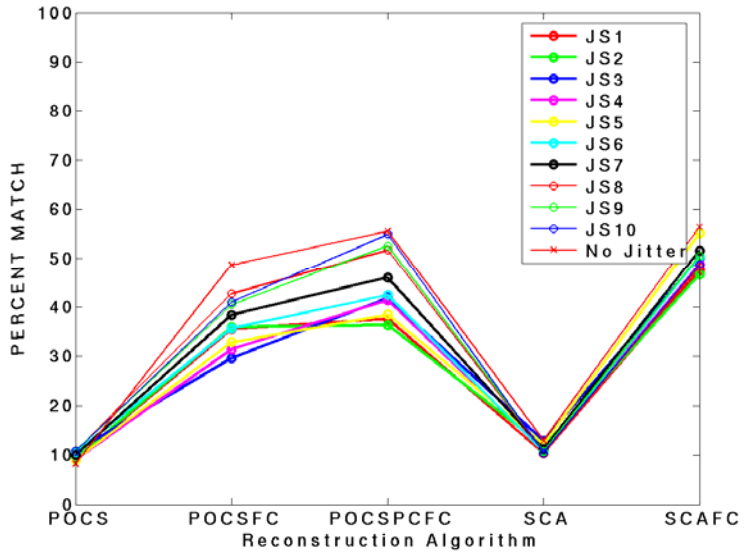

C- 52 Iran 256x256 Images, Bands 1-13 and 24-32, DFC Classification Algorithm, 5 Principal Component Constraint, Jitter Analysis

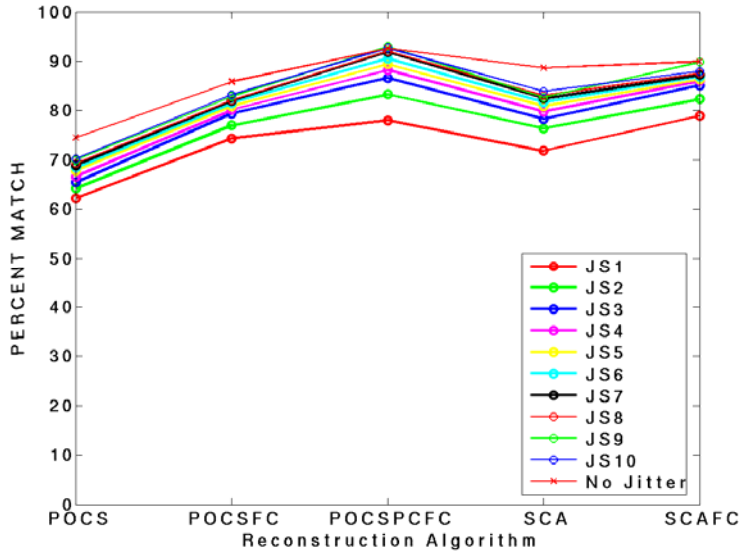

C- 53 Iran 256x256 Images, Bands 1-16, *k*-means Classification Algorithm, 3-Classes, Jitter Analysis

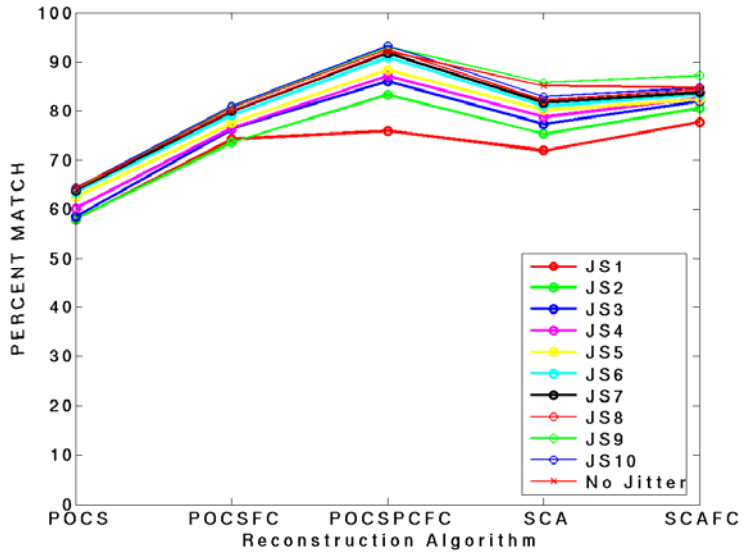

C- 54 Iran 256x256 Images, Bands 1-16, *k*-means Classification Algorithm, 3-Classes, 5 Principal Component Constraint, Jitter Analysis

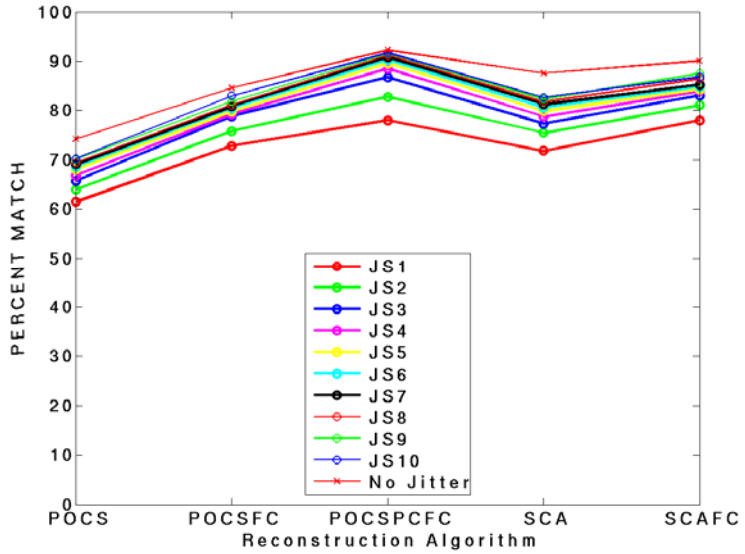

C- 55 Iran 256x256 Images, Bands: 1-13 and 24-32, *k*-means Classification Algorithm, 3-Classes, Jitter Analysis

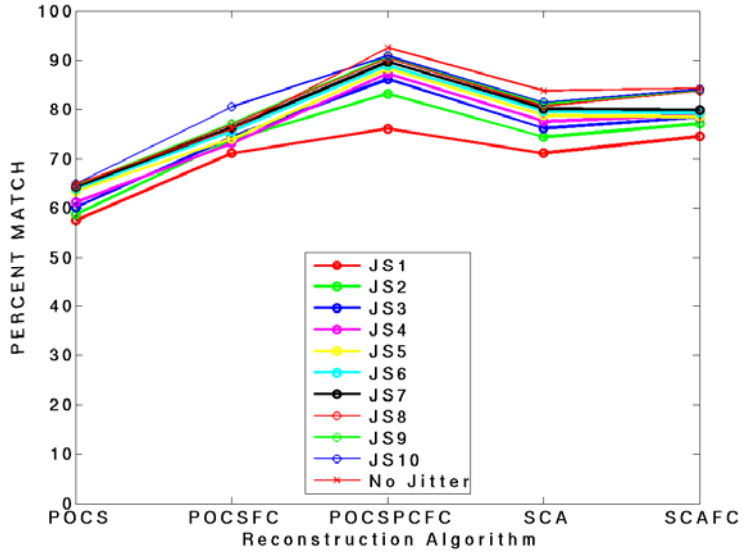

C- 56 Iran 256x256 Images, Bands: 1-13 and 24-32, *k*-means Classification Algorithm, 3-Classes, 5 Principal Component Constraint, Jitter Analysis

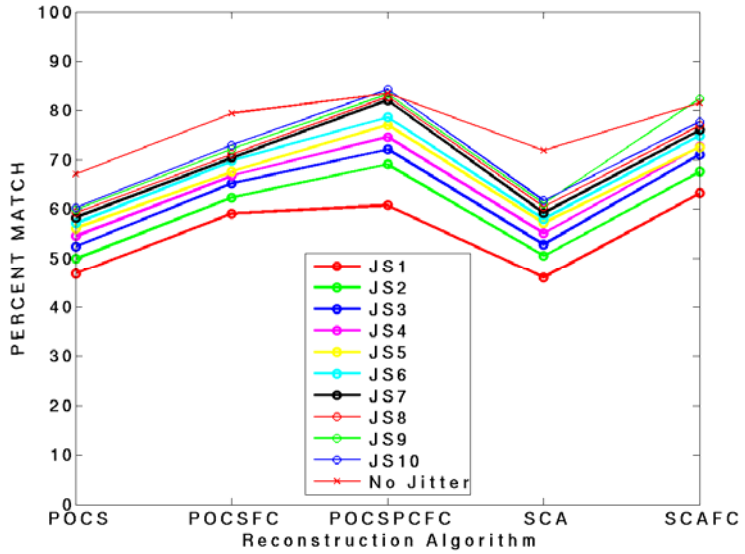

C- 57 Iran 256x256 Images, Bands: 1-16, *k*-means Classification Algorithm, 6-Classes, Jitter Analysis

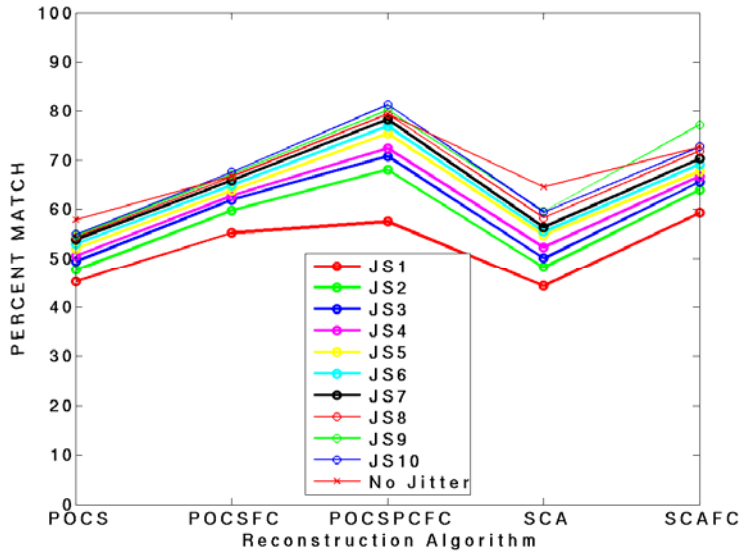

C- 58 Iran 256x256 Images, Bands: 1-16, *k*-means Classification Algorithm, 6-Classes, 5 Principal Component Constraint, Jitter Analysis

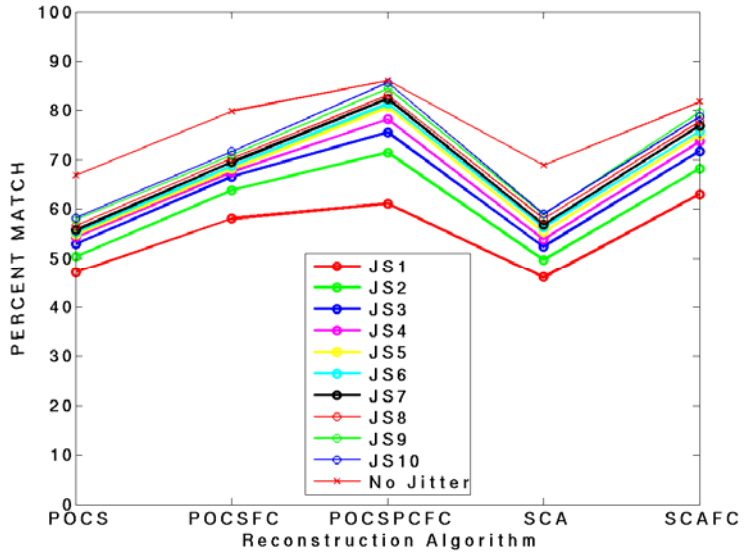

C- 59 Iran 256x256 Images, Bands: 1-13 and 24-32, *k*-means Classification Algorithm, 6-Classes, Jitter Analysis

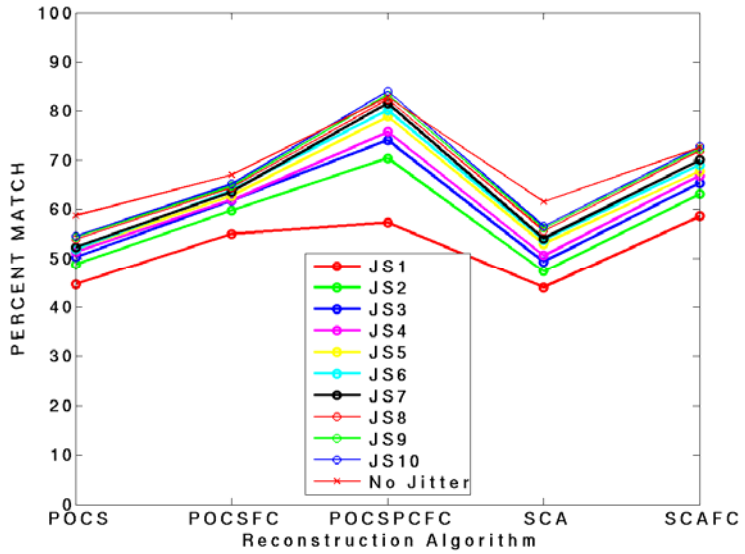

C- 60 Iran 256x256 Images, Bands: 1-13 and 24-32, *k*-means Classification Algorithm, 6-Classes, 5 Principal Component Constraint, Jitter Analysis

Israel 256x256

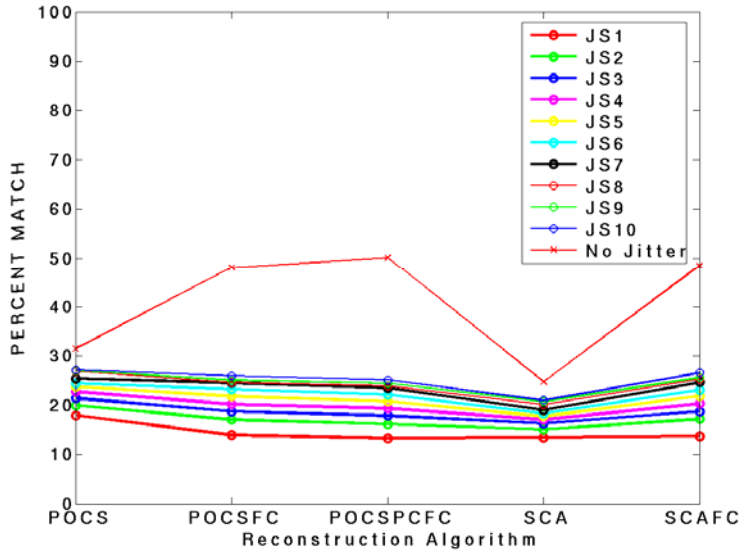

C- 61 Israel 256x256 Images, Bands 1-16, DFC Classification Algorithm, Jitter Analysis

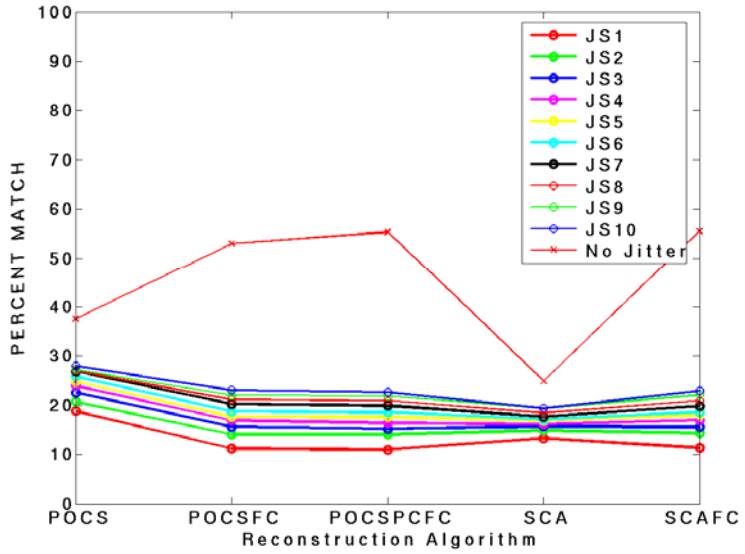

C- 62 Israel 256x256 Images, Bands 1-16, DFC Classification Algorithm, 5 Principal Component Analysis, Jitter Analysis

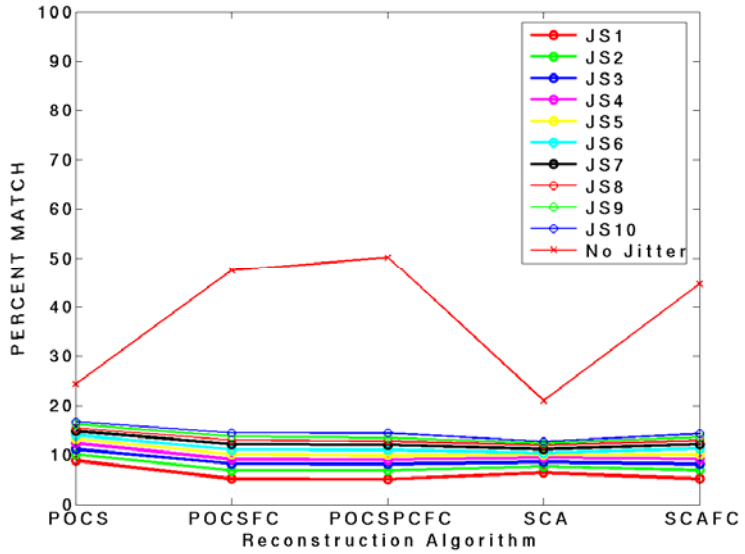

C- 63 Israel 256x256 Images, Bands 1-13 and 24-32, DFC Classification Algorithm, Jitter Analysis

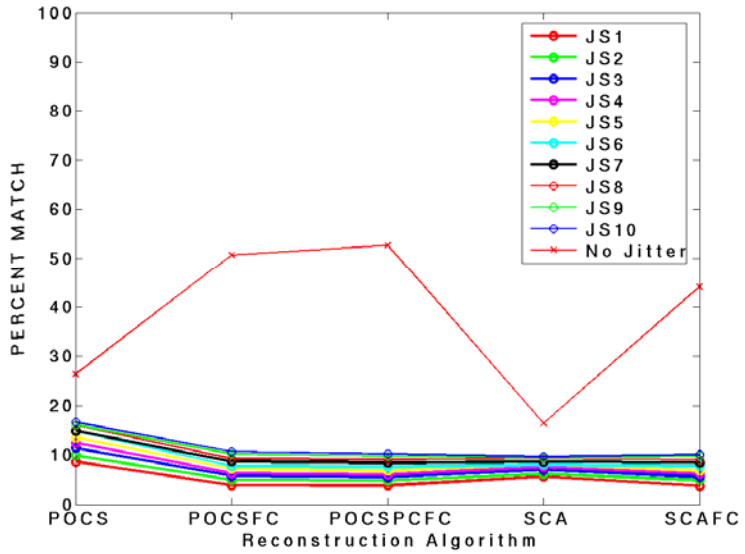

C- 64 Israel 256x256 Images, Bands 1-13 and 24-32, DFC Classification Algorithm, 5 Principal Component Analysis, Jitter Analysis

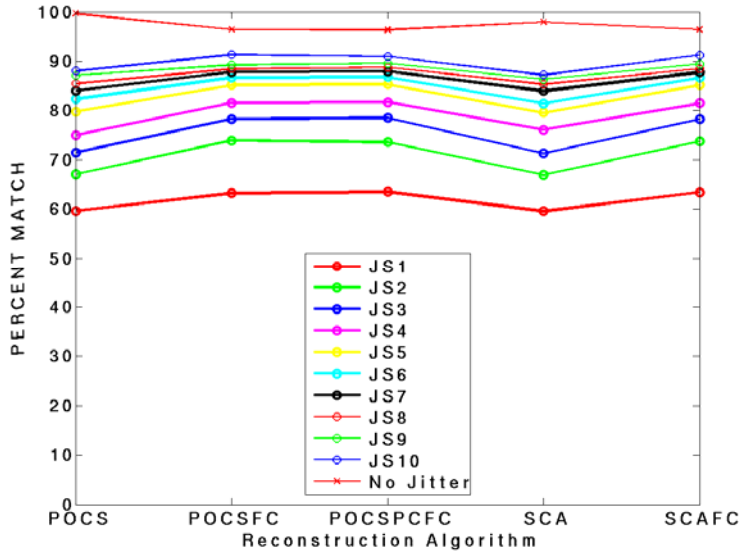

C- 65 Israel 256x256 Images, Bands 1-16, *k*-means Classification Algorithm, 3-Classes, Jitter Analysis

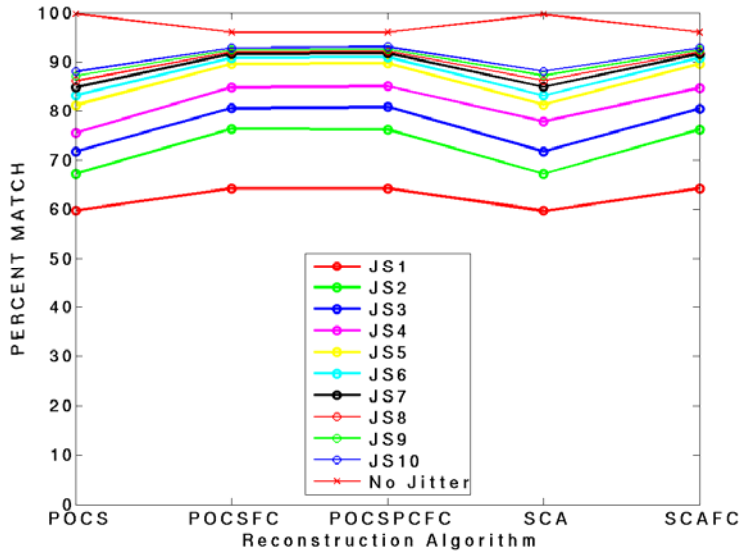

C- 66 Israel 256x256 Images, Bands 1-16, *k*-means Classification Algorithm, 3-Classes, 5 Principal Component Constraint, Jitter Analysis

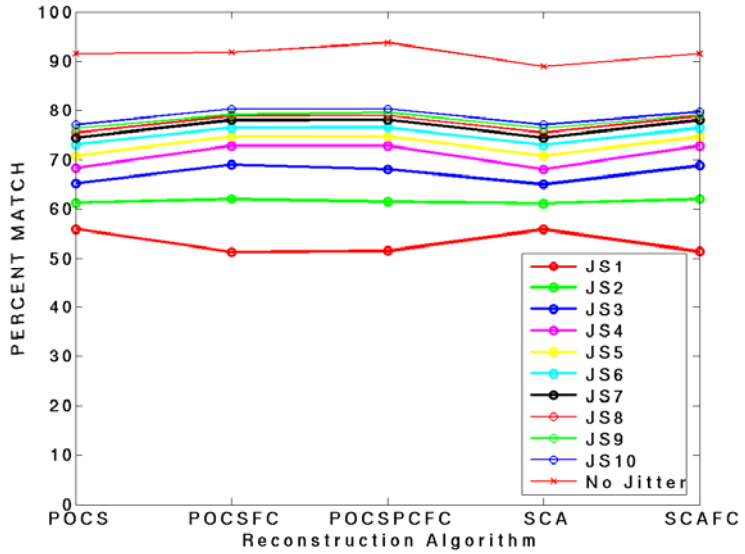

C- 67 Israel 256x256 Images, Bands 1-13 and 24-32, *k*-means Classification Algorithm, 3-Classes, Jitter Analysis

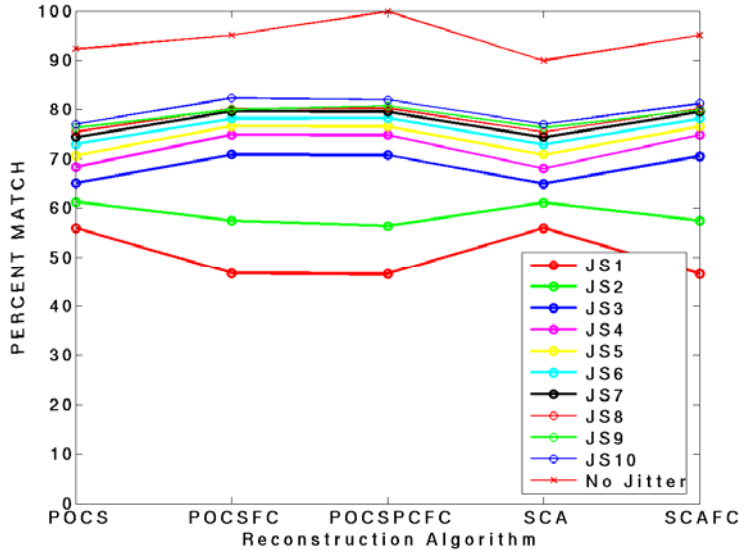

C- 68 Israel 256x256 Images, Bands 1-13 and 24-32, *k*-means Classification Algorithm, 3-Classes, 5 Principal Component Constraint, Jitter Analysis

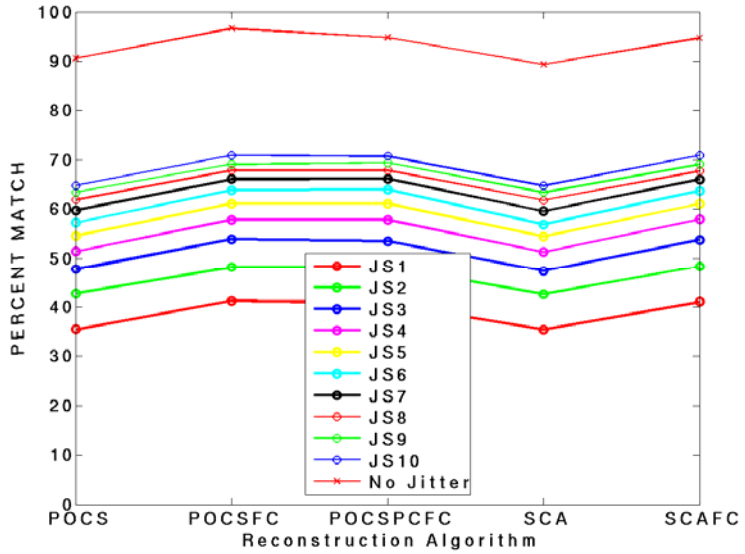

C- 69 Israel 256x256 Images, Bands 1-16, *k*-means Classification Algorithm, 6-Classes, Jitter Analysis

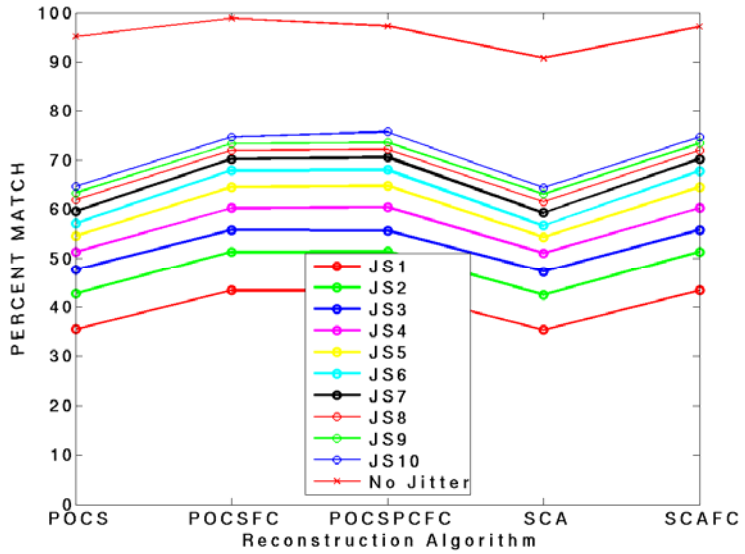

C- 70 Israel 256x256 Images, Bands 1-16, *k*-means Classification Algorithm, 6-Classes, 5 Principal Component Constraint, Jitter Analysis

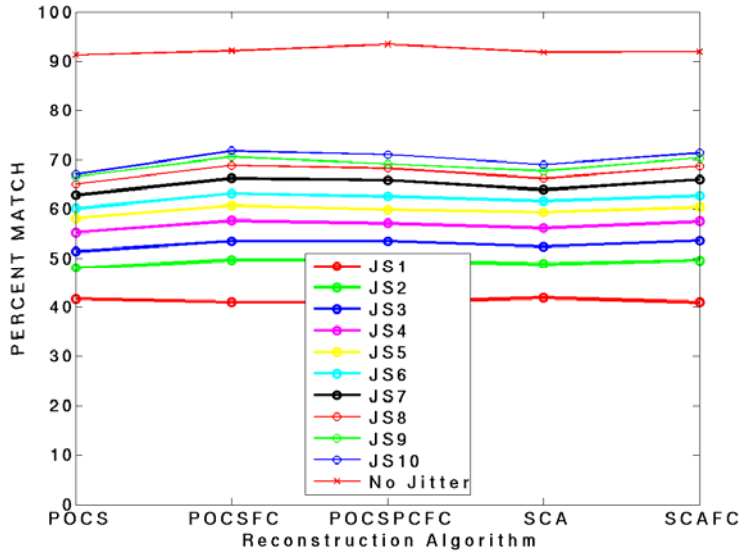

C- 71 Israel 256x256 Images, Bands 1-13 and 24-32, *k*-means Classification Algorithm, 6-Classes, Jitter Analysis

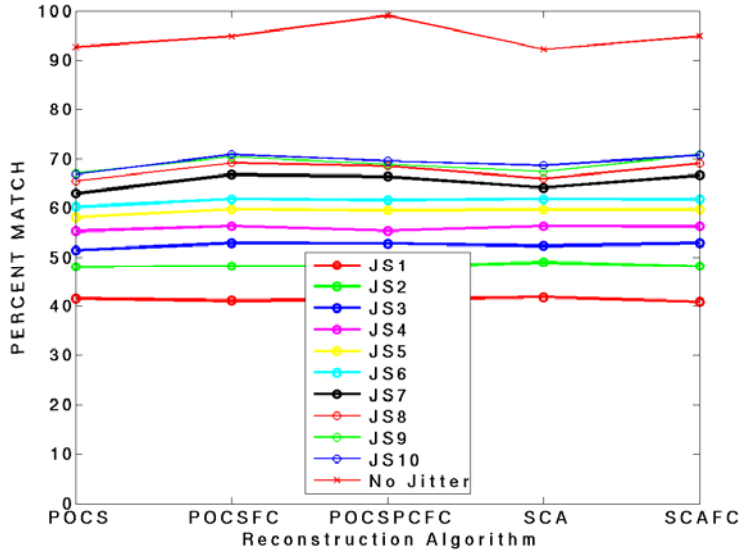

C- 72 Israel 256x256 Images, Bands 1-13 and 24-32, *k*-means Classification Algorithm, 6-Classes, 5 Principal Component Constraint, Jitter Analysis

References

1. J.E. Maurguia, T.D. Reeves, J.M. Mooney, W.S. Ewing, F.D. Shepherd, A. Brodzik. *A Compact Visible/Near Infrared Hyperspectral Imager.* Proceedings of SPIE, Vol. 4028. *In* Infrared Detectors and Focal Plane Arrays VI. Editors: E.L. Dereniak and R.E. Sampson, 2000.

2. M.R. Descour and E.L. Deraniak. *Computed-tomography Imaging Spectrometer: Experimental calibration and Reconstruction Results.* Applied Optics 34(22):4817-26, 1995.

3. H. Barrett and W. Swindell, *Radiological Imaging: The Theory of Image Formation, Detection and Processing,* Academic Press, 1996

4. M. An. *Data Restoration in Chromo-Tomographic hyperspectral imaging*. www.solidstatescientific.com/pdfs/datarestoration.pdf. Date Unknown.

5. A.K. Brodzik and J.M. Mooney, *Convex projections algorithm for restoration of limited-angle chromotomographic images*, JOSA A, 16(2):246-257, 1999

6. SciTec, Inc. Princeton, NJ.

7. PTC, Needham, MA.

8. Photon Research Associates, Inc. San Diego, CA.

9. K. Hartt, M.J Carlotto, and M.W. Brennan. "A Method for Multi-Dimensional Image Classification," Geosicience and Remote Sensing Symposium, IGARSS IEEE International pp. 509-512, 1989

10. S.J Roberts, "Parametric and Non-Parametric Unsupervised Cluster Analysis," Pattern Recognition vol. 30, pp. 327-345, 1989

11. X. Zhuang, Y. Huang, K. Palaniapppan, and Y. Zhao, "Gaussian Mixture Density Modeling Decomposition and Applications," IEEE Transactions on Image Processing, vol. 5, pp. 1293-1302, 1996

12. K. Popat and R.W. Picard. *Cluster-Based Probability Model and Its Application to Image and Texture Processing,* IEEE Transactions on Image Processing, vol. 6, pp. 268-284, 1997

13. A.K. Jain and R.C. Dubes, *Algorithms for Clustering Data*. Prentice Hall, 1988

14. D. Comaniciu, *Nonparametric Robust Methods for Computer Vision*, PhD Thesis, Department of Electrical and Computer Engineering, Rutgers University, 1999

15. J.T. Tou, R.C. Gonzalez. *Pattern Recognition Principles,* Addison Wesley Publishing Company, 1974

16. Salazar, J.S. and Smith, J.L., "Nonparametric Image Classification Applied to Multispectral Thermal Imager Data," Proceedings of SPIE, Algorithms and Technologies for Multispectral, Hyperspectral, and Ultraspectral Imagery IX, pp. 306-319, 2003

17 Cormen, T.H., Leiserson, C.E., Rivest, R.L., and Stein, C., Introduction to Algorithms. MIT Press, Cambridge, Massachusetts, 2002.

Distribution

2	MS 0899	Technical Library, 9616
2	MS 9018	Central Technical Files, 8945-1
1	MS-0123	Donna Chavez
1	MS-0972	C. Andy Boye


Sandia National Laboratories